arXiv:astro-ph/0411631v1 23 Nov 2004

Space telescope Imaging Spectrograph ultraviolet spectra of LMC planetary nebulae. A study of carbon abundances and stellar evolution. [1]

Letizia Stanghellini[2]

National Optical Astronomy Observatory, 950 N. Cherry Av., Tucson, AZ 85719, USA; letizia@noao.edu

Richard A. Shaw

National Optical Astronomy Observatory, 950 N. Cherry Av., Tucson, AZ 85719, USA; shaw@noao.edu

Diane Gilmore

Space Telescope Science Institute, 3700 San Martin Drive, Baltimore, Maryland 21218, USA; dkarakla@stsci.edu

ABSTRACT

We acquired spectra of 24 LMC PNe in the 1150–3000 Å range in order to determine carbon and other ionic abundances. The sample more than doubles the number of LMC PNe with good quality UV spectra in this wavelength range, and whose optical images are available in the HST archive. The Space Telescope Imaging Spectrograph was used with a very large aperture to obtain virtually slit-less spectra, thus the monochromatic images in the major nebulae emission lines are also available. The analysis of the data shows extremely good quality spectra. This paper presents the emission lines identified and measured, and the calculation of the ionic abundances of the emitting carbon and other ions, and total carbon abundance. P-Cygni profiles have been found in a fraction of the nebulae, and the limiting velocities of the stellar winds estimated. The total carbon abundance can be inferred reliably in most nebulae. We found that the average carbon abundance in round and elliptical PNe is one order of magnitude larger than that of the bipolar PNe, while elliptical and round PNe with a bipolar core have a bimodal behavior. This results confirm that bipolarity in LMC PNe is tightly correlated with high mass progenitors. When compared to predicted

[2] On leave from INAF-Bologna Observatory

yields, we found that the observed abundance ratio show a shift toward higher carbon abundances, that may be due to initial conditions assumed in the models not appropriate for LMC PNe.

Subject headings: Planetary nebulae, central stars of planetary nebulae, stellar evolution, nucleosynthesis, ultraviolet spectroscopy, Magellanic Clouds

1. Introduction

Planetary Nebulae (PNe) have been studied for decades, and through those efforts has come an understanding of the final phases of stellar evolution of stars with masses in the 1 – 8 $M_\odot$ range. Since PNe are gas shells ejected by evolved stars, they refuel the ISM with elements processed by stellar evolution. Thus PNe are ideal probes to test the theory of stellar evolution itself, and to study the ISM enrichment from their parent stars in a quantitative way.

The scientific importance of studying Planetary Nebulae in the Large Magellanic Cloud (LMC) can be very simply summarized: LMC PNe are absolute probes of stellar and nebular brightness, luminosity, and size, because their distance is known (unlike the distances to Galactic PNe which are typically uncertain by $\gtrsim$ 50%) and because their interstellar extinction is comparatively low (unlike Galactic PNe, where the disk and bulge PN populations are underrepresented in most samples).

Planetary nebulae are ejected toward the end of the evolution of low- and intermediate-mass stars, after the thermally-pulsing asymptotic giant branch (TP-AGB) phase. The gas ejected at this phase contains elements that have been produced during the previous evolutionary stages, and then carried to the stellar surface by the convective dredge-up processes (Iben & Renzini 1983; van den Hoek & Groenewegen 1997, hereafter HG 97). The single-star evolution models predict a chemical enrichment of the outer region of evolved stars in the 1 – 8 $M_\odot$ range, which can be summarized in the following four points: (a) During the first Red Giant phase, the convective envelope penetrates regions that are partially CNO-processed. This dredge-up results in a ^{13}C and ^{14}N enhancement, and depletion of ^{12}C. Later, He-burning starts in the stellar core, marking the beginning of the Horizontal Branch phase.

---

[1]Based on observations made with the NASA/ESA Hubble Space Telescope, obtained at the Space Telescope Science Institute, which is operated by the Association of universities for research in Astronomy, Inc., under NASA contract NAS 5–26555

Helium burning then continues in the helium shell. Finally, the hydrogen and helium burning occur alternately in two nuclear burning shells surrounding the CO core, and the star ramps up to the TP-AGB; (b) The second convective dredge-up (for stellar masses larger than 3 $M_\odot$) occurs at the onset of the AGB, when the H-burning is quiescent. This process carries ^{4}He, ^{13}C, and ^{14}N-rich material to the stellar surface; (c) During the TP-AGB phase, the envelope is able to dredge-up material after each thermal pulse, carrying ^{4}He, ^{12}C, and the s-process elements to the surface; and (d) For stars with masses larger than 3 $M_\odot$, one final process is thought to occur that alters the chemical composition: the so-called "hot-bottom burning" (HBB) that processes most of the carbon into nitrogen.

Stellar evolution models predict the sequence of processes given above for Galactic and LMC PN progenitors alike (HG97). The key to assessing the above predictions is to measure the abundances of the processed elements, particularly C, N, and O, which is straightforward to do with PNe. Carbon depletion and nitrogen enrichment also depend on the progenitor mass, which forms a direct connection between observed progenitor mass (i.e. Population) and chemical content. Evolutionary models show that carbon depletion and nitrogen enrichment in higher mass progenitors occur in models with a variety of initial chemistry, thus, by measuring the C and N abundances in PNe one can at once validate key elements of stellar evolution theory, and make a more robust measure of the contribution of low- and intermediate-mass stars to the enrichment of the local ISM.

It is important to note that most central stars are found at low luminosity on the HR diagram, where even a very small error in the luminosity translates into a large error in the inferred mass (Stanghellini & Renzini 2000). The great advantage of performing such an abundance study on LMC PNe is that we know their distance, thus a direct comparison of models and data is possible, in principle, by determining the mass of the central stars from their location on the HR diagram and comparing predicted and observed elemental abundances.

Abundance calculations require optical and ultraviolet nebular lines to support a reliable analysis of all the ionized stages of the relevant ions. Optical spectra of both LMC and Galactic PNe can be acquired from the ground. By studying extra-Galactic PNe, we have shown that morphology is a surprisingly useful indicator of the progenitor stellar population (Stanghellini, Shaw, Balick, & Blades 2000, hereafter SSBB). From a combination of morphology (determined from the images) and abundances, SSBB demonstrated that bipolarity in LMC PNe is indicative of a younger stellar progenitor. This was shown by the high abundance of alpha-elements (Ne, S, Ar), and other elements not altered by stellar evolution of these stars. SSBB found that nitrogen enhancement and carbon depletion are also mildly correlated with bipolarity (see Figures 1 and 2 in SSBB). These two main results were

broadly consistent with the predictions of stellar evolution if the progenitors of bipolar PNe have on average larger masses than the progenitors of round and elliptical PNe. The SSBB results are based on a rather small sample of objects: The carbon abundance was known at that time for only 18 LMC PNe with known morphology.

While the UV diagnostics emission lines are available in the IUE archive for several bright LMC PNe, and in the HST archives for a few others acquired with the FOS, most of these LMC PNe do not have spatially-resolved optical counterparts. More importantly, none of their central stars have been observed directly. The first set of central stars of LMC PNe available in the literature has been acquired with HST program 8271 (Shaw et al. 2001; Stanghellini et al. 2002), and the stellar physics has been studied by Villaver, Stanghellini, & Shaw (2003). Ultraviolet spectra of most of these targets are not available in the literature, nor in the HST and IUE Data Archives. To study how the chemical evolution of PNe relates to the evolution of their stars and morphology, we have acquired low dispersion UV STIS spectra of those LMC PNe for which narrow-band images have been acquired with HST, but for which no UV spectroscopy existed. This total of 24 targets greatly improves the statistics of LMC PNe whose carbon abundance has been determined, and it constitutes the first data set ever available to study central stars of PNe and their nucleosynthesis without the distance bias well known in Galactic PNe. This paper deals with the observed nebular properties in the UV, and presents limited comparison of the data to theoretical yields. In x 2 we present the observations and the data analysis of the 24 target PNe. Section 3 includes the study of the emission lines and the calculation the ionic and carbon abundances, including the comparison between the derived abundances and the theoretical yields, and the comparison of our abundances to those of Galactic PNe. In x4 we summarize and discuss the conclusions of our findings. The analysis of the stellar continua, the detailed modeling of the central stars winds, and the detailed modeling for each nebula will be published in future papers.

2. Observations and data analysis

We observed 24 LMC PNe using the STIS MAMA detectors with the first-order G140L and G230L gratings for long-slit spectroscopy, covering the NUV-FUV wavelength range from 1150 to 3100 A. The spatial scale of the spectrograms is 2.44 10^{2} arcsec pix^{1}, an excellent resolution to observe the morphology of the emission lines in LMC PNe that are typically half an acrsec wide. The G140L grating has central wavelength $_{c}$= 1425 A and the spectral range is 590 A, with nominal point source spectral resolution of 1425 at $_{c}$ (Proffitt et al. 2002). The G230L grating has $_{c}$= 2376 A and = 1616 A, with spectral resolution of 740 at $_{c}$. The spectral resolution of our near slit-less spectra depends on the extension

of the feature, and it is typically much lower than the nominal point source resolution. The observing log is presented in Table 1.

We observed the nebulae using a large $6'' \times 6''$ aperture to produce monochromatic images of the nebulae in each emission line. In these images, spatial information is convoluted with spectral information in the dispersion direction, practically as in a slit-less spectrum. However, most spectral emission lines are well-separated, providing a clear picture of the spatial morphology in the UV emission lines. Also, because most LMC PNe are angularly small, total uncontaminated fluxes are easily determined. While no comparison arcs were acquired related to these spectra, their pattern of separations, together with the known wavelength limits of the gratings, provide for unique identification of the lines in all but a few cases. For the rest, identification was based on the most probable features expected.

To measure the fluxes of emission features, images were collapsed in the spatial direction by extracting a spectrum using the x1d task in the IRAF[2] stis package (McGrath et al. 1999; Hulbert et al. 1997). The flux-calibration of extracted spectra relies, in part, on the quality of the spectral wavelength calibration. For each observation the position of the source in the dispersion direction is unknown.

Since the reference wavelengths are suitable only for a source centered in the aperture and with velocity, it was necessary to determine the offset between the reference wavelength positions and the source wavelengths prior to flux calibration. The process we used is outlined below in section 2.2.

2.1. Data Reduction

We obtained the bias-subtracted and dark-corrected spectral images, as processed with calstis (McGrath et al. 1999; Hulbert et al. 1997) from the HST archive. Spectra obtained with large apertures were not automatically flat-corrected during OTFR since it was believed at one time that the flat-field might be wavelength-dependent. The flat-field correction was applied separately to the data using the most appropriate reference files available (those generated from slit data). This is a two-step process. This correction is small for typical PN fluxes. High-resolution PFLATS, or pixel-to-pixel flats, have 5–6% peak-to-peak variations in alternating columns, but these are rebinned by a factor of two in each dimension when

[2] IRAF is the Image Reduction and Analysis Facility, a general-purpose software system for the reduction and analysis of astronomical data. It is distributed by the National Optical Astronomy Observatories, which are operated by the Association of Universities for Research in Astronomy, Inc., under cooperative agreement with the National Science Foundation.

applied to the science data. Rebinning to a lower resolution smoothes out the effect, so that only the smallest, brightest emission line fluxes are affected at the 1-2% level. This is comparable to the flux errors of only the highest S/N PN spectra. Typical PN emission features are more extended and less bright, and flat-field correction has a much smaller effect.

In addition to the PFLATS, LFLATS, which contain the large-scale flat-field variations were also applied to the science data during flat-field correction. These remove the spatially-dependent sensitivity variations, and are normalized to a value of one in the standard extraction region. The spatial dependance is negligible in the G230L data, and LFLAT calibration for these is routinely not performed, and was not for our G230L PN data. The flat-field effects are more pronounced in the FUV (the G140L data). All our spectra are extracted from a region where there are at most a few percent variations in the LFLAT. The LFLATs contain variations on scales larger than about 60 pixels, and are by definition 1.0 in the standard extraction region. They contain only the spatial-dependance of the flat-field correction. The task x1d removes the spectral-dependance.

Furthermore, x1d corrects for sensitivity variations across the field (interpolated between certain values of A2CENTER in the SPTRCTAB), but it assumes the spectrum is at the aperture center in the dispersion direction. We used an iterative procedure to correct for the wavelength offset. If the source is not centered well, the effects on the flux calibration are worse at the edges of the spectrum. Applying the wavelength offset correction to SHIFTA1 to rest wavelength as we do when we extract the spectrum with x1d should remove most of the effect. The other potential effect on fluxes is due to the wavelength offset caused by the radial velocity of the source, which was not accounted for. That could potentially affect the goodness of the sensitivity correction that is applied with x1d. However, we calculated a difference of only a few pixels for the radial velocity offset, so we believe that it will not affect the fluxes at a significant level.

2.2. Spectral extraction

The height and width of the extraction region were determined at the image center in the dispersion direction. The y-height was taken as the visual centroid of continuum emission, where present. Continuum emission from either the central star, or in some cases, the nebula itself, were used. In some cases it was possible to further refine the spatial center during the extraction by cross-correlation with the appropriate line profile.

The extraction width was determined by visual examination of the brightest nebular emission line feature, and was later enlarged if it was found to be smaller than 1.5 times

the FWHM of the measured feature in the extracted spectrum. For a gaussian intensity distribution, about 96% of the light falls within this limit. For flatter distributions, more of the light falls outside the limit, and the measured flux represents a conservative estimate of the total flux in the line. For those sources with flatter wings, we used a Voigt function to more accurately measure the flux.

Since the two-dimensional spectra are not perfectly aligned with the image rows, spectra extracted from different y-heights of the two-dimensional image have non-parallel spectral traces along the dispersion direction. The traces for a sampling of heights are provided in the reference file SPTRCTAB found in the image header and are used by the extraction routine, x1d, to appropriately extract spectra. The traces are interpolated for heights between listed table values.

Background-subtraction was performed during spectral extraction. The background contribution was measured in large areas away from the nebular spectrum and any continuum spectral sources in the field. This process helped remove the geo-coronal lines that are prominent in the G140L data.

For some PNe, like SMP 19 and SMP 71, different emission lines of the same nebula have different spatial extensions. In most cases where this is true, the centroid of the intensity distribution is the same, but the gradient is different. For a few of the nebulae we chose to extract spectra using two different widths in order to more appropriately measure the fluxes in the various features. Where larger extraction regions are used, the measured flux is subject to larger noise errors.

In several cases the stellar continuum is clearly distinguished in the 2D spectra.

2.3. Aperture correction

The aperture correction is appropriate for point sources, since by extracting 1D spectra with very narrow widths one may undercount the total flux by not including the flux scattered outside the aperture itself. The correction is applied in x1d for specific extraction widths. The task x1d selects the most closely-matching extraction width and applies the corresponding aperture correction found in PCTAB. However, since the nebulae are all of different spatial extent (few of which are point-sources) and all have been measured with various aperture sizes, it was decided to measure the fluxes without aperture corrections. We instead try to estimate the size of the aperture correction for a few different nebulae, and incorporate it into a flux error.

2.4. Feature identification and flux measurement

The extracted spectra were plotted and the locations of the gaussian centers of detectable features were measured with the IRAF task splot. Wavelength offsets were determined by comparing feature centers measured with splot to the wavelengths of lines identified with our own IDL routine. The IDL routine plots an array of marks representing the locations of possible emission features onto the two-dimensional spectral image. The array is shifted until the best visual alignment is achieved. More weight is given to matching prominent UV lines predicted by current theory of PN evolution (Cox 2000; Feibelman, Oliversen, Nicholsbohlin, & Garhart 1988). Once the line identifications are established, comparison of the feature centers measured with splot and the rest wavelengths of the identified lines yields the wavelength shift of the extracted spectrum. Conversion to pixel offsets was done using the average dispersion of the spectrum for the given grating, and the image header keyword SHIFTA1 was updated with the computed offset. For PNe with few emission lines, stellar emission or absorption features were used to help wavelength-calibrate the spectra whenever possible. Additionally, the sky emission at L and O i 1304 aided wavelength calibration of the G140L spectra. Sky emission from these lines fills the aperture and creates large boxes of emission superimposed on the nebular spectrum. These geocoronal lines were used primarily as a guide to exclude alternate wavelength solutions when the solution was otherwise uncertain.

Spectra were then re-extracted with x1d which used the header SHIFTA1 values to more accurately flux-calibrate the extracted spectrum. This method allows for a first-order correction of the wavelengths. Two other factors add to the wavelength-solution uncertainty: the spatial extent of the source in the dispersion direction (especially diffuse or complex sources like SMP 30 and SMP 93), and the source's radial velocity. The line-of-sight heliocentric velocity to the LMC is about 270 km sec ^{1}. For the gratings used, this velocity amounts to no more than a few pixels offset in the dispersion direction. Sources with emission features having a non-symmetric spatial distribution will further complicate the determination of unique wavelengths across the spectrum. The resultant wavelength correction then will depend on several factors: the number of features present, their spatial extent, intensity, and symmetry. For some nebulae, we used the interstellar absorption lines in the spectra of nearby stars to help determine the wavelength solution whenever possible.

To measure the flux in the line, Gaussian fits were performed. During measurement, the cursor is placed at the level of the continuum on either side of the feature before the feature is fit with a Gaussian. This procedure removes the contribution of the underlying stellar continuum, if present, from the flux measurements. When close-lying spectral features appeared in the extracted spectra, de-blending was done using the d feature in splot, which

solves for several superimposed spectral features with the same baseline.

We have identified several nebular emission lines and a few stellar P-Cygni features in our sample of PNe. We observed the helium recombination lines at 1640, 2511, and 2733 Å, corresponding respectively to the He II Balmer-, Paschen-, and Paschen- lines. We saw, as expected, many of the carbon features that were the essential motivation for this science program, namely C II 1335/36 and 2837/38 (both in emission and as a P-Cygni profile); C II] 2325–29; C III 1175/76 (possibly collisionally populated), a feature at 1247, possibly a C III emission line; C III] 1907/09; and C IV 1548/50. We observed the following emission lines from the oxygen ions: [O II] 2470; O III] 1658–1666; [O III] 2321/31; the Bowen fluorescence emission of O III 3043/47 and 3133; the possible O IV 1342 in SMP 102 only; O IV] 1407; and O V 1371, with a P-Cygni profile in SMP 79. We have also identified the following features: N III] 1747–1754; N IV] 1483/87; N V 1239/43 (with P-Cygni profile, typical of O stars); [Ne IV] 1602 and 2423/25; [Ne V] 1575; [Si III] 2334–50 (in SMP 28); Si III] 1883 and 1892; O IV] 1397/1407. Finally, some lines whose identification remains uncertain are S II 1915 (in SMP 28); a possible Fe II feature at 2629 Å (in SMP 28); Mg II 2796/2803, and Mg V 2784/2929.

In Table 2 we give the complete set of observed emission lines. Column (1) gives the PN name, column (2) and (3) the laboratory wavelength and identification of the emission line(s) respectively, column (4) gives the flux ratio of the emission line relative to H , columns (5) and (6) the extinction correction of the targets for the Galactic and LMC contributions, and column (7) gives the corrected line ratio (see §2.5). Finally, column (8) gives comments on the measured fluxes. The H fluxes in these ratios are from the STIS/HST data from Stanghellini et al. (2002). These H fluxes were measured by extracting 1D spectra from the 2D (slitless) optical spectral images with the same apertures for given PNe than used in the 1D extraction of the UV spectra.

The P-Cygni profile analysis is given in Table 3. The terminal velocities were measured at the violet edge of the P-Cygni absorption feature. This gives a good indication of the terminal velocity for well-saturated lines. In the cases that we present here, most of the P-Cygni lines are not totally saturated, but they are very strong, and their measurement gives a good estimate of the velocity (Lamers, Snow, & Lindholm 1995). In most cases we have two measurements of the terminal velocity for each of the nebulae in this Table. A good estimate of the terminal velocity could then be the average of these two measurements. In some cases, one of the features had very low S/N, as noted in the table notes, and the other velocity measurement should be taken for further use.

The 1D spectra of all targets are plotted in Figures 1 through 24. In order to make the plots more legible, we have smoothed the spectra with a 10 pixel box-car (naturally all

measurements were obtained from the original data). We use the excitation constant (EC) from Morgan (1984), when available (see §3.2 and Table 4). Information on the central star temperature is taken from the Zanstra analysis by Villaver, Stanghellini, & Shaw (2003).

While stellar and detailed nebular models are not the intent of this paper, we could get an estimate of the effective temperature of the central stars in the cases where the stellar continua were clearly present in the 2D spectra and, shortward of 2200 Å, could be fitted with a simple black body function. We use these estimates only to double check the consistency between Zanstra temperatures and emission spectra. Detailed nebular and stellar models, including the UV and optical data, will be presented in a future paper.

In the following text we describe in some detail the spectra of our targets.

J 41: This is an intermediate excitation nebula with central star temperature $T_{Z(HeII)}$ = 60,000 K. The G140L spectrum is very noisy and does not show other features than a possible trace of the C IV 1548/50 line. Black-body fitting of the continuum confirms the Zanstra temperature. There is a trace of emission at 1220 Å. The G230L spectrum clearly shows the C III] 1907/09 feature, but no other obvious emission lines (see Fig. 1). Absorption lines are identified with 2380 He II and 2799 Mg II.

SMP 4: A moderately high excitation nebula, whose Zanstra temperature, $T_{Z(HeII)}$ = 90,000 K. the stellar continuum is prominent in the 2D image, and the Zanstra temperature agrees with the black-body fitting of the stellar continuum. The nebular morphology of the 2D line images is similar to that of the optical images (Shaw et al. 2001). We detected and measured the C II 1335/36 resonance line, with superimposed interstellar absorption. Possible absorption features are detected at Lγ, Si II 1309 Å, C II 1335/36 Å, and S II 1253 Å. Evidence of dust absorption is evident at about 2200 Å. The flux in the [Ne V] emission at 1575 Å is marginal, while its presence agrees with the nebular high excitation (see fig. 2).

SMP 9: This is a moderately high excitation PN, with EC = 6–7. (Fig. 3). The 2D image shows nebular continuum and almost no stellar continuum. The major UV lines are all as spatially extended as the optical emission lines. We marginally detect a feature around 1400 Å, probably Si IV, or O IV], or a blend of the two components. We also marginally detect the Mg II emission around 2800 Å, corresponding to the blend of the 2796/2803, 2800 features.

SMP 10: An intermediate excitation nebula (Fig. 4), with EC = 6–7 and Zanstra temperature $T_{Z(HeII)}$ = 75,000 K. The marginal detection of the [Ne V] 1575 line agrees with the relatively high stellar temperature. The 2D G140L spectrum clearly shows the continuum of the central star. We detect several emission features. The N V 1239 emission line is measured, while an additional component of the N V doublet is barely detected at 1243 Å.

Absorption features are evident at λ 1334 (possibly C II), and others. The signal-to-noise ratio (S/N) is low for this extended, point-symmetric PN.

SMP 16: This is a high excitation nebula ($T_{Z(HeII)}$ = 142,000 K, EC = 8) with plenty of emission lines in its spectra (see Fig. 5). The stellar continuum is almost completely absorbed in the G140L spectrum, while there is evident nebular continuum. The O III 1658–1666 line is measured above the wings of the He II 1640 feature. A feature around 2150 Å is unidentified. We marginally detected a group of emission lines around 2740Å, possibly O II.

SMP 18: The G140L spectrum of this nebula is dominated by the absorption lines (Fig. 6). The spectra are characteristic of a low-excitation nebula (EC = 2–6), where the He II lines are barely seen below the 5 percent level. The black-body temperature, measured by UV continuum fitting, is around 40,000 K. We detect two P-Cygni features, corresponding to N V 1239/43 and C IV 1548/50. We also detect sky absorption lines at λ 1304 O I, 1335/36 C II, and 1371 O V, and possibly others. A possible emission at 1600 Å may correspond to the Ne IV line. The prominent C III] 1907/09 line is the only extended emission in this PN. Other absorption lines, notably Mg II at 2799, and some Fe features, are present in the G230L spectrum. A possible emission feature blended with C III] is detected at 1993 Å.

SMP 19: A high excitation nebula ($T_{Z(HeII)}$ = 144,000 K, EC = 7), it shows faint nebular continuum (Fig. 7). The marginal presence of [Ne V] 1575 confirms the high-excitation temperature. Both spectrograms show several emission lines, including the O III lines. Most of the nebular lines are extended in the 2D spectra, similarly to the optical emission lines. As in SMP 4, there is evidence of dust absorption around 2200 Å.

SMP 25: Similarly to SMP 18, the G140L spectrum (Fig. 8) presents P-Cygni profiles corresponding to the photospheric N V 1239/43 and C IV 1548/50 winds. In the G230L spectrum, the nebular emission features corresponding to C III] 1908 and C II] 2325–29 are as spatially extended as the optical emission lines. The stellar continuum is visible in the 2D spectra.

SMP 27: Another photosphere-dominated G140L spectrum for this low excitation (EC = 3–6) quadrupolar PN (Fig. 9). The continuum fitting gives a stellar temperature around 30,000 K. the G140L spectrum presents P-Cygni profiles corresponding to the photospheric N V 1239/43 and C IV 1550 winds. Several absorption lines are observed in the G140L spectrum, including λ. Very interesting is the G230L spectrum, where we can see the nebular C III] emission at 1908, and several absorption features including an absorption feature around 2598, that could be identified as Fe II.

SMP 28: Very rich spectra (Fig. 10) of a moderately high excitation PN (EC = 6–7).

The group of features around 1400 Å are hard to identify unambiguously. It could be the Si IV plus two or more of the O IV emission lines around 1400 Å. The blend around 1900 Å is probably a combination of the Si III lines (1883, 1892), C III] 1907/09, and Si I 1915. The G230L spectrum presents an unidentified two-component feature at 2145 Å, possibly Fe II 2630, and O III 3133. It looks like there are two components to most emission lines. The optical slit-less images also look double, thus both the optical and UV emission originates from two nebular blobs.

SMP 30: The spectra of this very extended PN have low S/N (Fig. 11). This is a high excitation PN, with EC = 8. The [Ne V] feature at 1575 that would confirm the high excitation status could not be correctly measured, but its presence can't be excluded given the low signal to noise ratio. The continuum is typically nebular, thus no black body temperature could be estimated. The feature at 1403 Å could be interpreted either as a blend of the O IV multiplet, or as Si IV. The G230L spectrum is characterized by nebular continuum, and by the C III] 1909 line. The wavelength calibration of the G230L spectrum is somewhat uncertain, since the only three features available are very broad and have low S/N. An unidentified features has been observed at 2135 Å.

SMP 34: A low excitation nebula (Fig. 12), with EC = 2. While Zanstra analysis gives $T_{Z(HeII)}$ = 68,000, the UV continuum fitting suggests a somewhat lower temperature (40,000 K). As with SMP 18, SMP 25, and SMP 27, the G140L spectrum shows P-Cygni profiles corresponding to the photospheric 1239/43 N V and 1548/50 C IV wind features. Several sky lines are seen in absorption, overlying a strong stellar continuum.

SMP 45: Very large nebula, and low S/N spectra with few clear emission features (Fig. 13). The excitation is moderately high (EC = 6). The wavelength calibration of the G230L spectrum is uncertain, thus the features listed in Table 2 could be misidentified. As in SMP 30, a diffuse nebular continuum is present in both spectrograms.

SMP 46: A high excitation nebula (Fig. 14) with $T_{Z(HeII)}$ = 119,000 K and EC = 6, its high S/N spectra shows all the major carbon emission lines. The spectrogram also shows a diffuse nebular continuum like SMP 45 (Fig. 14).

SMP 48: Absorption is present at L. The P-Cygni profiles correspond to N V 1239/43 and C IV 1548/50 (Fig. 15). The G230L spectrum shows the C III] and C II] lines, an absorption feature at 2381 Å (possibly He II), a possible absorption feature around 2596 Å (Fe II), and Mg II at 2800. This is a low excitation nebula (EC = 3-4) with central star temperature T = 30,000 K inferred from the continuum fitting. The continuum shows a dominant stellar component.

SMP 59: Extended quadrupolar PN with high central star temperature ($T_{Z(HeII)}$ = 98,000

K) and high excitation (EC = 7–9) (Fig. 16). There is marginal detections of [Ne v] at 1575. The 2D spectra are adjacent to the edge of the aperture. The extracted 1D spectrum may not include the whole nebular flux in the emission lines. We estimate, from the 2D image, that less or about 20 % of the flux may be not accounted for in the 1D extracted spectra.

SMP 71: Moderately high excitation PN ($T_{Z(HeII)}$ = 83,400 K and EC = 6–7), with a very rich spectrum (Fig. 17). Like SMP 45 and SMP 46, the G140L spectrum shows a diffuse nebular continuum, and the stellar continuum. An unidentified emission feature is evident at 1520 A, in the wing of the C iv feature.

SMP 72: An extended PN whose optical image was taken with the early PC1 (Dopita et al. 1996), and whose UV spectra show very low S/N (Fig. 18). The 2D spectra indicate the presence of stellar continuum. Both the C iv 1550 and the He ii 1640 emission lines are broad, due to the large spatial extent of the nebula, and marginal splitting. This is a relatively high excitation nebula (EC = 7), though [Ne v] 1575 is not detected.

SMP 79: A moderate excitation PN (EC = 5, Fig. 19), with a rich emission spectrum. The P-Cygni feature at 1371 A is associated with stellar O v. We do not know the Zanstra temperature of the central star, but the presence of O v indicates it to be an early O star, and the presence of [Ne v] in the spectra indicates high excitation. A fit to the prominent stellar continuum gives T 60,000 K. Another possible P-Cygni feature is shown in the G230L spectrum, corresponding to the C ii 2837/38 emission. Like SMP 71, and possibly SMP 19, the spectrum shows emission at 2783 A (Mg v or [Ar V]?)

SMP 80: The G140L spectrum shows hydrogen in absorption, and possible P-Cygni lines corresponding to N v 1240, and C iv 1550. The almost featureless G230L spectrum shows only a possible low intensity C iii] 1909 A feature. The G230L spectrum has sloping continuum. The excitation is low in this PN (EC = 2–4, T = 30,000 K from continuum fitting, spectra in Fig. 20).

SMP 81: A very compact PN, showing L absorption. The wing of this absorption line merges with the P-Cygni profile corresponding to photospheric N v 1239/43 emission (Fig. 21). The determination of the strength of these lines is thus uncertain, given the particular configuration. All the major nebular emission lines are present. Absorption features are detected at 1304, 1335/36, 2380, 2591, and 2799, A, possibly corresponding to Si iii, C ii, He ii, Fe ii, and Mg ii. The nebula has intermediate optical excitation (EC = 5) and T = 45,000 K from the stellar continuum fitting.

SMP 93: An unusually extended PN, its Zanstra temperature, $T_{Z(HeII)}$ = 372,000 K, is likely to be an overestimate (Villaver, Stanghellini, & Shaw 2003). The nebular excitation from the optical lines is deemed to be high (EC = 8). The spectra have very low S/N so that

the extracted uxes and wavelengths are uncertain (Fig. 22). The line pro les are similar to those of SM P 72. Like SM P 45 and others, the spectrum shows di use nebular continuum. As for SM P 59, the nebula is at the edge of the aperture, and its line intensities may be underestimated.

SM P 95: A moderately high excitation elliptical nebula (EC = 5–7, $T_{Z(HeII)}$ = 146,000 K), where the major UV lines have the same two-dimensional morphology as the optical lines. Many nebular emission lines appear in the spectra (Fig. 23). The continuum is weak and appears to be of nebular origin from the 2D spectra analysis.

SM P 102: A high excitation nebula ($T_{Z(HeII)}$ = 132,000 K, EC = 7), shows a host of emission lines (Fig. 24). Absorption features are evident at L , O i or S ii at 1301, and elsewhere. SM P 102 shows a di use ellipsoidal light distribution in most lines with a small circular enhancement on the redward side of a few emission features. This enhanced region is more prominent in the C iii] 1908 and C ii 2325–29 lines than in any other feature seen. Neutral helium is seen in emission at 2734. The stellar continuum is prominent in both its spectra.

2.5. Extinction correction

The ux measurements have been corrected both for Galactic foreground and for the LMC extinction. It was assumed that the internal extinction within the nebulae is negligible. Since the extinction curves for the LMC and the Galaxy are di erent in the UV, we have proceeded as follows. The relation between observed and de-reddened uxes, scaled to H , can be written as:

$$I/I = (F/F)10^{(cf)} \quad (1)$$

where c is the target-dependent logarithmic extinction at H and f is the reddening function at wavelength . The reddening term includes a foreground Galactic and a LMC component. We can express the double origin of extinction as:

$$cf = c_G f_{,G} + c_{LMC} f_{,LMC} \quad (2)$$

where c_G is the reddening constant for the Galactic foreground in the direction of the LMC, $f_{,G}$ is the Galactic extinction law, c_{LMC} is the reddening constant for the LMC, and $f_{,LMC}$ is the LMC extinction law. Since the Galactic and LMC extinction laws are di erent in the UV, we need to correct for the two terms independently.

We use the values of the Galactic color excess, E_{B-V}, for the line-of-sight to each of our targets from Gochermann (private communication), and we calculate $c_G = 1.47\,E_{B-V}$ for each target, as listed in Table 2, column (5). In a couple of cases the foreground reddening was not available from Gochermann and we have estimated E_{B-V} by eye, from the LMC foreground reddening map of Schwering & Israel (1991).

By using $f_{\lambda,G}$ from Cardelli, Clayton, & Mathis (1989), we correct the UV fluxes by foreground extinction, and obtain:

$$(I_\lambda/I_\beta)_0 = F_\lambda/F_\beta\ 10^{(c_G f_{\lambda,G})}. \qquad (3)$$

If we apply Equation (3) to the $(H\alpha/H\beta)$ ratio, we obtain $(H\alpha/H\beta)_0$, an essential ingredient for evaluating the LMC reddening:

$$c_{LMC} = 2.875 \quad \log[(H\alpha/H\beta)_0/2.85] \qquad (4)$$

where 2.875 is the inverse of the f value at $H\beta$, and 2.85 is the assumed intrinsic ratio of $H\alpha/H\beta$ in the case of T_e= 10,000 and N_e= 10,000 K (Osterbrock 1989).

Values of c_{LMC} are listed in Table 2, Column 6. If the computed foreground optical extinction constant is larger than the total optical extinction constant from Stanghellini et al. (2002), implying that the foreground correction overshoots the actual reddening, we set c_{LMC} = 0 instead of using Eq. (4).

The final step of the de-reddening is the correction for the LMC extinction, by using:

$$I_\lambda/I_\beta = (I_\lambda/I_\beta)_0 10^{(c_{LMC} f_{\lambda,LMC})}; \qquad (5)$$

where $f_{\lambda,LMC}$ is parametrized by Howarth (1983). The line intensity ratios in Table 2 have been corrected with the above procedure.

In Figure 25 we show the histograms of the foreground and LMC extinction constant, c_G and c_{LMC}. We omitted one datum from the LMC plot, corresponding to c_{LMC} = 0.96 of SMP 45, for compactness of the Figure. The averages of the extinction constants are respectively $< c_G > = 0.11 \pm 0.06$, and $< c_{LMC} > = 0.09 \pm 0.20$. While the foreground correction tends to be more evenly distributed than the LMC factor, it is clear that adopting the same foreground constant for all PNe in our target list would be inappropriate. In studies of LMC PNe, a common c_G for the foreground correction is usually assumed. For example, Vassiliadis et al. (1998) use c_G = 0.074 for the Galactic foreground to the LMC PNe, which

is a moderately appropriate median value, but not at all representative of extreme PNe. We estimate that by using the point-by-point foreground extinction we have lowered errors in the measured de-reddened intensities as much as 50% in cases where the LMC reddening is very low. For example, in the case of SMP 79, using the foreground correction of $c_G = 0.074$ would underestimate the C IV flux by 52%.

A sanity check for the extinction correction is the comparison between the He II 1640 and the optical 4686 lines. We will not be able to derive an extinction constant from this comparison, given the two-step procedure that we use to correct our fluxes, but we can compare the two de-reddened intensities for each nebula where these are available. We correlate the UV and optical He II line intensities. The UV and optical line intensities correlate tightly ($R_{xy} = 0.97$), and their least square fit gives $I_{1640} = 5.011 \; I_{4686}$, in broad agreement with the theoretical predictions (Osterbrock 1989). This result demonstrates that the UV extinction corrections we have applied are appropriate. There are two straggler points in this relation corresponding to SMP 59 and SMP 93, the two very extended PNe whose intensities are uncertain due to their positions within the aperture.

3. Results

3.1. Flux ranges, errors, and comparisons

In Figure 26 we plot the cumulative distributions of the line intensities (relative to Hβ) of the four most commonly observed emission lines in our spectra: C IV 1540/50, He II 1640, C III] 1907/09, and C II] 2325–29. These plots show the normal distribution of the line ratios in our PN sample. The plots also show the the median intensity ratios in the prominent lines. The carbon lines are very prominent in LMC PNe, and they are typically several times the intensity of Hβ. In Galactic PNe, the C IV line is typically half of the Hβ flux, while the C III] line is only slightly higher than Hβ (Henry, Kwitter, & Bates 2000). The carbon emission can be an important coolant in LMC PNe, as shown by Stanghellini et al. (2003).

In order to determine the errors associated with the line intensities, we should consider the many sources of possible errors in the data analysis, namely, (1) the sky subtraction, (2) the spectral extraction, (3) the measure of the actual spectral line by line fit, (4) the extinction correction, and (5) the uncertainty due to the S/N within the nebular spectra. We are less concerned about the errors due to the line identification. Typically, the emission lines observed in the spectra are well-recognized, with the possible exceptions of SMP 45 and SMP 30.

One of the tools that we can use to grossly constrain the error sources is the direct comparison of the emission line He II 1640 Å, which is often detectable both in the G140L and the G230L spectra. Since this line appears at the blue edge of the G230L spectra, its measure is uncertain, thus our comparison gives a super-conservative upper limit to the flux errors. We find that the He II fluxes from the two grisms are correlated with $R_{xy} > 0.96$, and that the average difference between the He II flux measured on the G140L and the G230L grisms is 28 ± 0.09%. We also find a mild relation between the photometric radii of the PNe (from optical data) and the G140L to G230L He II flux difference, with correlation coefficient $R_{xy} = 0.73$; PNe with radii smaller than about 0.4″ have He II flux errors smaller than about 25%. In general, for the central parts of the grisms, we expect that the flux errors are much smaller than this.

We should expect a marginal source of error in the flux determination in the cases in which the spectral lines did not have gaussian profile. This source of errors, though, is marginal with respect to other sources such as (1), (2) and (5) above. As an upper limit, we have the case of SMP 28 where the Balmer-α line was measured with a gaussian in the G230L spectrum and with a Voigt function in the G140L spectrum. The relative error between the two measurement is around 35%, which is on the upper end of the errors mentioned above.

We assume that the typical flux error from fitting a gaussian profile via the IRAF routines is < 5% (Stanghellini et al. 2002). This is the major error source for the UV fluxes of compact nebulae, with high S/N spectra, and for emission lines near the center of the grisms. Another check on the reliability of our calibrations is by comparing the UV and optical He II line emission, when the latter are available from the optical measurements in the literature. For this comparison we used the G140L fluxes in this paper (He II 1640) and the He II 4686 optical data either from Leisy (private communication) or from our own optical observations with the ESO telescopes (Shaw et al., in preparation). The intensities of the UV and optical He II fluxes for the 15 PNe used in the comparison correlate to better than 95%. If we exclude the large bipolar PNe (SMP 93 and SMP 59), whose fluxes carry larger errors due to the fact that the aperture of extraction do not include 100 % of their fluxes, the correlation coefficient goes up to 98%. This result indicates that the calibration is sound for what the emission lines are concerned.

The continuum level of the G140L and G230L spectra are the same in the common part of the spectra if the extraction box used is the same. In general, the extraction boxes are optimized for the emission lines, and this may affect the continuum level (but not the reliability of the line intensities). We take into account the different continuum level when we fit the UV continua with a Plankian function to obtain the (color) temperature of the central star.

3.2. Abundances

The main goal of these HST observations was that of deriving the carbon abundance for the target nebulae. All of the major emission lines that are commonly used to determine the C abundance in PNe fall in the satellite UV range between 1200 and 2000 Å. In this paper we calculate the abundances of the observable ions of C, N, O, and Ne, and from the C ions we derive approximate total C abundance for our targets.

Two fairly common approaches to computing chemical abundances in ionized nebulae are the "ICF" method and photo-ionization modeling (see, e.g., Aller 1984). In the ICF approach it is necessary to compute the electron temperature (T_e) and density (N_e) for the ionized gas from standard diagnostics, determine the abundances of the observed ions based upon the inferred T_e and N_e, and then use empirical relations to correct for the unseen ionization stages in order to derive total elemental abundances. The other common approach is to build a photo-ionization model of the nebula by iteratively positing physical characteristics (T_e, N_e, chemical abundance, physical size of the nebula, the spectral energy distribution of the ionizing source, etc.) and refining those assumptions in order to match the computed spectrum with that observed. Often these approaches can be combined to good effect (see, e.g., Hyung, Aller, & Feibelman 1994). In this paper we focus on the carbon abundance in these planetary nebulae, where the relevant ionization stages can generally be observed and where the temperature and density information is taken from other sources. For the modest accuracy required for the present purpose, the ICF method will suffice; more detailed nebular modeling will be addressed in a future paper.

The bulk of the ionic abundances for this study were computed using the nebular package in STSDAS, developed by Shaw & Dufour (1995), as updated by Shaw et al. (1998). We used as input the relative intensities from collisionally excited emission lines presented in Table 2, corrected for extinction. We adopted the simple model used in the nebular package for the variation of T_e and N_e within the nebula, namely, that the various plasma diagnostics are most applicable within one of three zones of ionization potential. For example, the densities and temperatures derived from [S II] and [O II] apply to a zone of low ionization, whereas the temperature derived from [O III] and the density derived from [Ar IV] apply to a zone of moderate ionization. The T_e and N_e applied within each target nebula is given in Table 4. These diagnostics were derived using nebular from standard T_e and N_e diagnostics and based upon fluxes from our own ground-based optical observations at ESO and MSSSO (Shaw et al. in preparation), and from the observations by Leisy (private communication). For a few nebulae where these diagnostic line fluxes were not available we have assumed typical values of electron temperature and density (also given in the table).

The ionic abundances presented in Table 6 were derived from the fluxes in the emission

lines given in Table 5. The abundance of some ions must be derived from recombination lines, which were estimated based on approximate relations from Aller (1984, and Table 5-3 therein), as they are not computed within the nebular package. In columns (2) through (4) of Table 6 we list the carbon ionic abundances C^{+}, C^{2+}, and C^{3+}, and in column (5) we give the sum of the carbon ionic abundances. Columns (6) through (10) give the abundances of the nitrogen ions, of O^{3+}, and of Ne^{3+} (though they are not used further in this paper).

We labeled the sum of the observed carbon ions in column (5) of Table 6 as the total C/H abundance, though in principle this sum must be corrected for the presence of C^{4+}, which is not observed. The magnitude of this correction can be estimated using the prescriptions given by Kingsburgh & Barlow (1994). In the case of the very high excitation nebulae, C V emission should be accompanied by N V 1240 emission since this latter ion has a much lower ionization potential. (Note that, normally, the presence of a N V 1240 feature with a P-Cygni profile is not an indication of a high excitation PN, since the origin of this feature is a stellar wind.) The absence of this nebular feature in many of our target nebulae is a strong indication that the C^{4+} abundance is very low or absent. In addition, the absence of He II 1640 strengthens the low-excitation classification for most PNe in our sample that do not show N V emission.

In our PN sample, SMP 4, SMP 10, SMP 16, SMP 28, and SMP 79 may be of high enough excitation to require a finite correction for C^{4+}. Here we examine the carbon content of these PNe in more detail. If we assume that C^{2+}/O^{2+} C/O (Leisy & Dennefeld 1996), and multiply that ratio by oxygen abundances obtained from the literature (Stasinska, Richer, & McCall 1998), we obtain C/H values that are comparable to the C/H ratios in Table 6. With this further assurance, and the extremely high potential of ionization of C V, we conclude that the carbon abundances in column (5) of Table 6 are good approximations for all of the high excitation PNe in this sample. In the low and intermediate excitation PNe, sometimes it happens that the C^{+} 2326 emission line intensity is weak and below the noise limit of the spectrum (SMP 30, SMP 45, SMP 72, and SMP 102). In these cases, the total carbon abundances in Table 6 may be underestimated by 10%. We have also checked whether there are correlations between the derived abundances and the excitation constant, EC, and found none. This is a good sign that the abundance analysis is sound and the results do not depend on the excitation level of the PN.

In Figures 27 and 28 we used our C/H abundances from Table 6 and the O/H, N/H, and He/H abundances from Stasinska, Richer, & McCall (1998). In addition, we also plot all data that were available a few years ago, and that have been presented in SSBB. In all we have a sizable sample of LMC PNe whose morphology are known from direct HST observations and whose carbon abundances have been derived by means of either HST or

IUE spectroscopy. Prior to this paper, there were 16 PNe in the LMC whose morphology and carbon abundances were known, though the morphologies only approximate since the HST images were from the pre-COSTAR era. The sample of 24 PNe presented in this paper more than doubles the original sample and improves enormously the reliability of the analysis.

In Figure 27 we show the C/H versus N/H relation in a plot where data points are coded by morphological type (open circles: round, asterisks: elliptical, filled triangles: round or elliptical with bipolar core, squares: bipolar, and filled circles: point-symmetric PNe). This is a quantitative improvement to the plot in Fig. 4 by SSBB. The additional nebulae shown here are the 11 nebulae studied in this paper whose nitrogen abundances are available in the literature (Stasinska, Richer, & McCall 1998). This plot largely confirms what was anticipated in SSBB: Bipolar and Point-symmetric PNe show low carbon and high nitrogen abundances with respect to hydrogen, while round and elliptical PNe show the opposite behavior. Interestingly, we also find that round and elliptical PNe with a bipolar core are split into two separate groups, one that is chemically more like bipolar, the other closer to the domain of elliptical PNe. From this plot, it looks like all bipolar (and point-symmetric) PNe of this sample have gone through the process of carbon depletion during the HBB, which also partially enriches nitrogen; round and elliptical PNe have not gone through that process, while the bipolar core PNe are a mixed group.

In Figure 27 the morphology of the bipolar PN with lowest nitrogen abundance (SMP 45), and the bipolar core PN with second to lowest nitrogen abundance (SMP 100), are ambiguous; erasing these two targets from the plot does not change any of the above results. A similar situation is shown when the C/O and N/O ratios are plotted (Fig. 28). Note that the arrow indicates the range of C/O that defines the domain of carbon stars, from which it is clear that bipolar PNe are not the progeny of carbon stars in the LMC (HG 97).

In Table 7 we give the average carbon abundances for each morphological type for the whole sample of PNe whose carbon abundance is known. The sample consists now of 40 LMC PNe, enough to populate each morphological class, except the point-symmetric, reliably. From the table we infer that the median carbon abundance of bipolar PNe is about one order of magnitude lower than those of round and elliptical PNe, while the content of carbon in bipolar core PNe is about half than that of round and elliptical PNe. We will explore the nature of BC PNe with detailed individual photo-ionization models in a future paper.

3.3. Comparison to theoretical yields

The carbon abundances that we derived can be used successfully to constrain the stellar evolution models for stars that undergo the AGB phase. Only with the comparison between the observed abundances and the theoretical yields one can improve the current knowledge of stellar evolution and its variation with initial metallicity.

Several authors have modeled the evolution of stars that go through the AGB phase, and then calculated the yields of the principal elements such as H, He, C, N, and O (Renzini & Voli 1981; van den Hoek & Groenewegen 1997; Forestini & Charbonnel 1997; Marigo 2001; Karakas 2003). For the comparison with LMC PN data we look for models that have initial LMC composition. Furthermore, we looked for authors that evaluated the mass return into the ISM both from the total evolution, and in the final thermal pulses, the latter mass return being directly comparable to the PN ejecta. The synthetic AGB models by Marigo (2001) (hereafter M01) cover a wide initial mass range, and initial Galactic, LMC, and SMC composition. Marigo (2001) also evaluated the expected PN composition by averaging the abundances in the mass ejected during the final 30,000 yr of the AGB. Such yields can be compared to our data directly. Van den Hoek & Groenewegen (1997) also produced yields for Magellanic and Galactic initial composition for a wide initial mass range of AGB evolutionary models, giving the total and final (25,000 yr) yields. By knowing the initial composition we can derive the expected PN composition to compare with our data, following their formulation.

It is worth noting that the models by M01 and HG97 are not directly comparable. Van den Hoek & Groenewegen (1997) uses the empirical mass loss prescription by Vassiliadis & Wood (1994), different mixing-length parameters for different initial mass, and $Y = 0.25$ for the initial set of LMC models. Van den Hoek & Groenewegen (1997) use Reimers (1975)'s mass loss rate with efficiency $= 4$ for the LMC models, independent of initial mass, $Y = 0.264$ for the initial LMC model. Finally, M01's use of extra-dredge up makes the carbon yields higher that those of HG97.

There are other evolutionary models in the literature that estimate atomic yields from AGB stars. Renzini & Voli (1981) gave surface and PN abundances derived from evolutionary models, but they did not perform their analysis for an LMC composition. Karakas (2003) calculated complete AGB models for stars in the appropriate mass range, and with adequate initial composition, but did not evaluate the mass fraction of the major atoms ejected in the final thermal pulses. Finally, Forestini & Charbonnel (1997) provided the yields in the final 4 thermal pulses, thus comparable with PN abundances, with extrapolated nucleosynthesis. The initial composition of their models is limited to $Z = 0.02$ and $Z = 0.005$, thus we will make only marginal use of these models in this paper.

In Figure 29 we show the log C/O vs. log N/O trends similarly to those of Fig. 28, including also those PNe whose morphology is uncertain or not known (small open circles). In this Figure we show the loci of the yields from the stellar evolution models models. M01 and HG97 PN yields for initial LMC composition have been plotted respectively with solid lines and broken lines. The lower curves connect log C/O and log N/O for initial masses in the 0.85 – 3.5 $M_\odot$ (M01) and 0.8 – 3.5 $M_\odot$ (HG97) ranges. The upper curves are for $M > 3.5\ M_\odot$. The segmented high mass solid curve corresponds to M01 models with $M > 3.5\ M_\odot$ and $= 1.68$, 2, and 2.5.

The models seem to generally encompass the data. The group of PNe with high C/O and low N/O are in the same general area of the low-mass models. We confirm that no bipolar PNe are in the general area of the low-mass models. On the other hand, it seems that the high mass ($M > 3.5\ M_\odot$) models predict carbon and nitrogen yields that are higher than observed in LMC PNe. While the different assumptions in the M01 and HG97 models make the relative yields slightly different, they both over-predict the elemental abundance of C/O and N/O in most high-mass cases. The effect of over-prediction of carbon and nitrogen in the case of high-mass progenitors is even more evident in Figure 30, where we plot the elemental abundances of C and N relative to hydrogen. None of the examined models yields to log C/H < 4, observed in roughly half of the PNe.

We believe that there are three possible explanations to account for the inconsistency of the prediction with respect to the observed abundances. First, the initial conditions used in the M01 and HG97 models may not be appropriate for the correct description of our data. HG97 obtains all the initial abundance ratios (C/H, N/H, etc) from the observed solar abundance ratios (Grevesse, Noels, & Sauval 1996), scaled according to Y. When comparing the initial conditions chosen by GH97 for the LMC to actual LMC abundance measurements, for example in H II regions or supernova remnants (Russell & Dopita 1990; Leisy & Dennefeld 1996), we found $(\log C/H) \quad 0.5$ and $(\log N/H) \quad 0.63$, where represent the differences between the HG97 model assumptions and the observed initial abundance in the LMC. By looking at Figure 30 one can see that this initial abundance bias may account for the observed inconsistency. Obviously, one must get the correct yields from the models with the appropriate initial conditions to obtain the right comparison. Karakas (2003) used in her LMC models appropriate initial conditions, as derived from the observations. We can not compare her models to our data here, since she does not provide with the final yields. Such a comparison would be very important for future developments.

Second, while we have considered only models of single star evolution, some of the PNe might originate from close binary evolution. This may be true especially in the case of aspheric PNe, whose morphology may derive from common envelope evolution. Although

complete binary models that involve an AGB star, with initial composition similar to that of LMC, does not exist, Izzard & Tout (2003, 2004) have calculated yields from binary evolution with solar composition. They found that, if we exclude the evolution through the nova and supernova stages, the final yields of C, N, and O from binary evolution are respectively 0.86, 0.69, and 1 times the yields from single star evolution. If such results could be extrapolated in the case of the LMC models, we see that would not be enough to account for the observed inconsistencies. Nonetheless, this is an interesting explanation that is related to PN morphology, and we know that the discrepancy is certainly higher for aspherical PNe.

Third, the theoretical yields in PNe represent the ejecta of the final stages of the evolution of the AGB stars, while the observations determine the elements ratios in the ionized gas. Within the ionized region of a PNe there may be additional carbon, confined in carbonaceous dust particles (Kwok 2004). While the dust contribution to the C/H ratio may be very low, it may be a factor to consider in comparing models and data. Finally, the presence of CO in PNe may alter the comparison of theoretical yields and observed abundances, depending on the geometry of the nebulae. In a convex, regular (such as round or elliptical) PN, CO is dissociated by the ionization front, and it will not coexist with the ionized gas. As a consequence, the abundances measured within the ionized gas well represent the actual elemental concentration. On the other hand, in the case of concave (such as bipolar) PNe, CO may lie in a ring orthogonal to the lobal axis (Josselin, Bachiller, Manchado, & Guerrero 2000). The inclusion of the ring CO in bipolar PNe in the abundance analysis is not possible to date, lacking an accurate model for bipolar mass loss that follows stellar evolution from the AGB onward.

3.4. Comparison with the Galactic sample

In Figure 31 we plot [C/H] against [N/H] for the LMC (filled circles, this paper) and the Galactic (Henry, Kwitter, & Bates 2000) (crosses) PN samples, and compare them with the M01 yields. Both yields and data have been scaled to the corresponding solar values given by Grevesse, Noels, & Sauval (1996), and we use the standard notation $[X/H] = (X/X)/(H/H)$. The thick line connects the yields of [C/H] and [N/H] for $0.85 < M/M < 5$ and $= 1.68$ (LMC models), while the thin lines connects the yields of [C/H] and [N/H] for $0.85 < M/M < 5$ and $= 1.68$ (Galactic models). From the Figure one can infer that neither the Galactic nor the LMC model yields reach down to the observed [C/H] and [N/H] concentration of, respectively, the Galactic and the LMC PN samples. Similar results are obtained when comparing the data of both the LMC and Galactic samples with HG97 models, as shown

in Figure 32. Here we reproduce the same data as of Fig. 31, except we superimpose to them the HG97 models, for LMC (thick broken line) and Galactic (thin broken line) AGB evolution. Both Figs. 31 and 32 give the clear impression of a systematic offset between observations and models.

In Figure 33 we plot [C/H] versus [O/H] for the LMC and the Galactic PN samples. Here we superimpose the the theoretical yields by M01 (LMC: thick solid line; Galaxy: thin solid line) and HG97 (LMC: thick broken line; Galaxy: thin broken line). While the yields by HG97 seem to better encompass both LMC and Galactic data, none of the models predict the observations satisfactorily.

We use Figs. 31 through 33 to compare the group characteristics of the LMC and Galactic PNe, especially for what carbon abundances are concerned. The carbon abundance seem to peak at lower oxygen (and nitrogen) values in the LMC than in the Galactic PNe. Also, carbon, nitrogen, and oxygen abundances of LMC and Galactic PNe seem to follow the same trends but LMC abundances are typically lower for all three elements. For the given samples, the median C/H abundance is 2.63×10^{-4} in the LMC and 4.11×10^{-4} in the Galactic PNe. It is worth noting that the models are unable to predict the actual abundance ratios correctly both for LMC and Galactic PNe, but they do predict quite accurately the trends of both C/H vs. O/H and C/H vs. N/H for both PN samples, including their offsets. While it is not straightforward to compare directly the LMC and Galactic PN samples, due to the selection biases that strongly affect Galactic observations, it seems clear that the samples analyzed here show similar characteristics, with a shift of (initial) conditions, where the LMC PN progenitors originate from a lower metallicity environment.

4. Summary and Discussion

We acquired the UV spectra of 24 LMC PNe with HST/STIS, by using the G140L and G230L grisms to obtain spectral information from 1150 to 3000 Å. The interstellar extinction was measured both for the Galactic and the LMC contributions case-by-case for all targets. Since none of the present PNe was observed before in the UV range, we could not compare our results with those available in the literature. Instead, we checked for internal consistency of the data set and for UV to optical consistency, finding that our line intensities are sound and errors reasonable, with the exception of residual errors in the extinction correction, that in all cases are much lower than the internal instrumental errors related to the observations.

For each nebula we determine the consistency between the excitation class from the optical images, the Zanstra temperature (determined by Villaver, Stanghellini, & Shaw 2003)

and, in some cases, the color temperature of the central stars determined by a Planck fit of the UV continuum. The excitation of the nebula was related to the emission lines present in the UV spectra. Eight PNe present P-Cygni profile typically in the C IV and N V features. We have measured the terminal velocities relative to these P-Cygni features.

We used the measured carbon lines to determine the ionic abundances, and we present the ionic abundances for carbon and other ions. The ionic abundances of carbon have been used to infer elemental carbon abundances. The data presented here more than double the sample of LMC PNe whose carbon abundance have became available. We found that the median (and mean) carbon abundance varies considerably across morphological types, being almost one order of magnitude larger in bipolar than in round PNe. These relations, while hinted previously (SSBB), are now supported by a sizable and reliable data set. We also confirm the previously determined carbon and nitrogen abundance trends that disclose the occurrence of the third dredge-up and the HBB events in the more massive progenitor stars. This is the first time that carbon and nitrogen abundances can be directly correlated for a large sample of PNe whose morphological type is known. We confirm the link between bipolarity and carbon depletion, and between carbon enrichment and spherical or elliptical symmetry, in the LMC.

By comparing the abundances studied in this paper to stellar yields calculated from evolutionary models we found that the predicted carbon abundances are generally higher that those observed. Our data have also been compared to those of Galactic PNe, and a similar mismatch between data and predictions has been found in both samples. We suspect that the discrepant predicted yields (especially of carbon) are at least partially due to the choice of initial composition in the leading models for whose the final yields are available to date (M01, HG97). The comparison of the data to the yields calculated with adequate initial conditions (e.g., those of Karakas 2003) will allow us to determine other possible causes of discrepancy, including binary star evolution. Models with a set of different HBB efficiencies will also be useful to determine whether an increased HBB efficiency may reconcile theoretical yields and our data. A possible source of discrepancy is also the limitation of the carbon abundance studies to the ionized gas. Future quantitative analysis of solid (dust) carbon will help to constraint the evolutionary models. More accurate modeling of the aspheric mass loss at the tip of the TP-AGB is also needed to completely account for the different components of the PN that may contain carbon in ionized and neutral gaseous, or solid form.

One of the main reasons to study the LMC PNe is that their distance is known, and consequently the determination of the central star masses can be performed more reliably than for Galactic PNe. The determination of the central star masses, and their relation to chemistry (especially carbon and nitrogen) and morphology, allows to account for the

evolutionary path between the low- and intermediate-mass star in the AGB and the PNe. The sample of LMC PNe whose central star masses has been measured (Villaver, Stanghellini, & Shaw 2003) and whose carbon abundance are known (this paper) consists of only seven objects, too small a sample for meaningful statistical analysis. Nonetheless there are a few individual comparison that are worth mentioning.

The central star mass of SMP 4 and SMP 10 is identical within the errors ($M_{CS} = 0.58$ $M_\odot$); the carbon abundance of the former, an elliptical PN, is a factor of 20 higher than the carbon abundance of the latter, a point-symmetric PN. From the carbon depletion detected in SMP 10 it is reasonable to assume that its progenitor mass was much higher than the progenitor mass of SMP 4. The similarity of the central star masses may indicate that a much more powerful mass-loss process had occurred to strip the envelope of SMP 10 than that of SMP 4. Other such examples are available. SMP 19 (an elliptical PN with a bipolar core) and SMP 30 (a bipolar PN, likely) have very similar CS masses, yet the former has much higher carbon content than the latter, suggesting that SMP 30 is the progeny of a higher mass progenitor, that underwent heavy mass-loss.

If the carbon depletion really occurs mainly during the HBB process, we would conclude that SMP 10 and SMP 30 have much higher progenitor masses than, respectively, SMP 4 and SMP 19. Yet their central stars end up with the same masses. The evolutionary path that produces the bipolar and point-symmetric PNe, SMP 10 and SMP 30, seems to be related to a much higher total mass-loss than the processes that produces the elliptical PNe SMP 4 and SMP 19.

A much larger data set of central stars of LMC PNe, and a similar data set for SMC PNe, are being collected to further explore these ideas. In addition, efforts are in order to develop hydrodynamic and photo-ionization models for the individual Magellanic planetary nebulae whose central star mass, morphology, and carbon abundance have become available.

5. Acknowledgements

Many thanks to Chris Blades, Bruce Balick, Eva Villaver, and Anabel Arrieta for scientific discussion and their help in this project, and to Tom Brown, Charles Proffitt, Phil Hodge, and Max Mutchler for their help in the data analysis. It is a pleasure to thank Josef Gochermann for providing us with the color excess for our targets, using his data prior of publication, and Pierre Leisy for allowing us to use his 4686 Å emission line intensities prior of publication. Thanks are due to an anonymous Referee for important suggestions. This project was supported by NASA to grant GO-09120.01-A from the Space Telescope Science

Institute, which is operated by the Association of Universities for Research in Astronomy (AURA), Inc., under NASA contract NAS 5-26555.

REFERENCES

Aller, L. H. 1984, Physics of Thermal Gaseous Nebulae, ISBN 90-277-1814-8; Astrophysics & Space Science Library vol. 112

Cardelli, J. A., Clayton, G. C., & Mathis, J. S. 1989, ApJ, 345, 245

Cox, A. N. 2000, Allen's astrophysical quantities, 4th ed. Publisher: New York: AIP Press; Springer. Edited by Arthur N. Cox.

Dopita, M. A. et al. 1996, ApJ, 460, 320

Feibelman, W. A., Oliversen, N. A., Nicholsbohlin, J., & Garhart, M. P. 1988, IUE

Forestini, M. & Charbonnel, C. 1997, A&AS, 123, 241

Grevesse, N., Noels, A., & Sauval, A. J. 1996, ASP Conf. Ser. 99: Cosmic Abundances, 117

Henry, R. B. C., Kwitter, K. B., & Bates, J. A. 2000, ApJ, 531, 928

Howarth, I. D. 1983, MNRAS, 203, 301

Hulbert, S., Hodge, P., Busko, I. 1997, The STScI STIS Pipeline VII: Extraction of 1-D Spectra, STIS Instrument Science Report 97-02 (Baltimore: STScI)

Hyung, S., Aller, L. H., & Feibelman, W. A., 1994, PASP, 106, 745

Iben, I. & Renzini, A. 1983, ARA&A, 21, 271

Izzard, R. G. & Tout, C. A. 2003, Publications of the Astronomical Society of Australia, 20, 345

Izzard, R. G. & Tout, C. A. 2004, MNRAS, 350, L1

Josselin, E., Bachiller, R., Manchado, A., & Guerrero, M. A. 2000, A&A, 353, 363

Kaler, J. B., Shaw, R. A., & Browning, L. 1997, PASP, 109, 289

Karakas, A. I. 2003, Ph. D. thesis, CSPA (Australia)

Kingsburgh, R. L. & Barlow, M. J. 1994, MNRAS, 271, 257

Kwok, S. 2004, Nature, 430, 985

Lamers, H. J. G. L. M., Snow, T. P., & Lindholm, D. M. 1995, ApJ, 455, 269

Leisy, P. & Dennefeld, M. 1996, A&AS, 116, 95

Marigo, P. 2001, A&A, 370, 194 (M01)

McGrath, M. A., Busko, I., Hodge, P. 1999, CALSTIS6: Extraction of 1-D Spectra in the STIS Calibration Pipeline, STIS Instrument Science Report 99-03 (Baltimore: STScI)

Morgan, D. H. 1984, MNRAS, 208, 633

Osterbrock, D. E. 1989, Research supported by the University of California, John Simon Guggenheim Memorial Foundation, University of Minnesota, et al. Mill Valley, CA, University Science Books, 422 p.

Prott, C. et al. 2002, STIS Instrument Handbook, version 6.0, (Baltimore: STScI)

Reimers, D. 1975, Problems in stellar atmospheres and envelopes., 229

Renzini, A. & Voli, M. 1981, A&A, 94, 175

Russell, S. C. & Dopita, M. A. 1990, ApJS, 74, 93

Shaw, R. A., De La Pena, M. D., Katsanis, R. M., & Williams, R. E. 1998, in ASP Conf. Ser. 145, Astronomical Data Analysis Software and Systems VII, ed. R. Albrecht, R. N. Hook, & H. A. Bushouse (San Francisco: ASP), 192

Shaw, R. A., Stanghellini, L., Mutchler, M., Balick, B., & Blades, J. C. 2001, ApJ, 548, 727

Shaw, R. A. & Dufour, R. J. 1995, PASP, 107, 896

Schwering, P. B. W. & Israel, F. P. 1991, A&A, 246, 231

Stanghellini, L. & Renzini, A. 2000, ApJ, 542, 308

Stanghellini, L., Shaw, R. A., Balick, B., & Blades, J. C. 2000, ApJ, 534, L167 (SSBB)

Stanghellini, L., Shaw, R. A., Mutchler, M., Palen, S., Balick, B., & Blades, J. C. 2002, ApJ, 575, 178

Stanghellini, L., Shaw, R. A., Balick, B., Mutchler, M., Blades, J. C., & Villaver, E. 2003, ApJ, 596, 997

Stasinska, G., Richer, M. G., & McCall, M. L. 1998, A&A, 336, 667

van den Hoek, L. B. & Groenewegen, M. A. T. 1997, A&AS, 123, 305 (HG 97)

Vassiliadis, E. & Wood, P. R. 1994, ApJS, 92, 125

Vassiliadis, E. et al. 1998, ApJS, 114, 237

Villaver, E., Stanghellini, L., & Shaw, R. A. 2003, ApJ, 597, 298

This preprint was prepared with the AAS LaTeX macros v5.2.

Fig. 1.| G140L (a) and G230L (b) spectrograms of J41

Fig. 2.| As in Fig. 1, for SMP 04

Fig. 3.| As in Fig. 1, for SMP 09

Fig. 4.| As in Fig. 1, for SMP 10

Fig. 5.| As in Fig. 1, for SMP 16

Fig. 6.| As in Fig. 1, for SMP 18

Fig. 7.| As in Fig. 1, for SMP 19

Fig. 8.| As in Fig. 1, for SMP 25

Fig. 9.| As in Fig. 1, for SMP 27

Fig. 10.| As in Fig. 1, for SMP 28

Fig. 11.| As in Fig. 1, for SMP 30

Fig. 12.| As in Fig. 1, for SMP 34

Fig. 13.| As in Fig. 1, for SMP 45

Fig. 14.| As in Fig. 1, for SMP 46

Fig. 15.| As in Fig. 1, for SMP 48

Fig. 16.| As in Fig. 1, for SMP 59

Fig. 17.| As in Fig. 1, for SMP 71

Fig. 18.| As in Fig. 1, for SMP 72

Fig. 19.| As in Fig. 1, for SMP 79

Fig. 20.| As in Fig. 1, for SMP 80

Fig. 21.| As in Fig. 1, for SMP 81

Fig. 22.| As in Fig. 1, for SMP 93

Fig. 23.| As in Fig. 1, for SMP 95

Fig. 24.— As in Fig. 1, for SMP 102

Fig. 25.— Distributions of the Galactic foreground extinction constant (top) and the LMC extintion constant for the nebulae in our sample.

Fig. 26.— Cumulative gaussian distributions of the de-reddened intensities of the major emission lines in the nebulae of our sample. The emitting ion and its wavelength are indicated in the figure legend. The cross correspond to the mean flux in the given ion. The solid lines correspond to the domain $< F > \quad .$

Fig. 27.— N/H vs. C/H abundances for the sample od this paper (nitrogen abundances from Stasinska, Richer, & McCall (1998)) plotted with the sample in Stanghellini, Shaw, Balick, & Blades (2000). The symbols code the morphological types: open circles= round; asterisks= elliptical, filled triangles: round or elliptical with bipolar core; filled squares: bipolar, filled circles: point-symmetric PNe.

Fig. 28.— N/O vs. C/O abundances for the sample od this paper (nitrogen and oxygen abundances from Stasinska, Richer, & McCall (1998)) plotted with the sample in Stanghellini, Shaw, Balick, & Blades (2000). The symbols are codes as in Figure 27. Note that the arrow indicates the range of abundances in carbon stars.

Fig. 29.— Same as in Fig. 28, with superimposed the final yields from the LMC M01's models (solid lines; upper lines are for M 3.5 M and $=1.68$, 2, and 2.5; lower line is for M 3.5 and $=1.68$) and from the LMC HG97 models (broken lines; upper line is for M 3.5 M, lower line for M 3.5).

Fig. 30.— Same as in Fig. 29, but for the N/H vs. C/H ratios.

Fig. 31.— [C/H] vs. [N/H] for LMC (filled circles) and Galactic (crosses) PNe. Galactic PN data are from Henry, Kwitter, & Bates (2000). Thick solid line: LMC M01 yields for $=1.68$; thin solid line: Galactic M01 yields for $=1.68$.

Fig. 32.— [C/H] vs. [N/H] for LMC (filled circles) and Galactic (crosses) PNe, as in Fig. 30. Theoretical yields from HG97. Thick broken line: LMC HG97 yields; thin broken line: Galactic HG97 yields.

Fig. 33.— [C/H] vs. [O/H] for LMC (filled circles) and Galactic (crosses) PNe. Galactic PN data are from Henry, Kwitter, & Bates (2000). Thick solid line: LMC M01 yields for $=1.68$; thin solid line: Galactic M01 yields for $=1.68$. Thick broken line: LMC HG97 yields; thin broken line: Galactic HG97 yields.

Table 1. Observing log[a]

Name	data set	obs. date	t_{exp} [s]
J 41	o6cn01ngq	2002-01-31	1320
	o6cn01niq	2002-01-31	133
SMP 04	o6cn02ncq	2001-10-11	1440
	o6cn02ndq	2001-10-11	1445
SMP 09	o6cn03ceq	2002-08-03	2880
	o6cn03ciq	2002-08-04	1930
SMP 10	o6cn04gdq	2002-04-15	1320
	o6cn04gfq	2002-04-15	1260
SMP 16	o6cn05o0q	2002-01-31	1320
	o6cn05o2q	2002-01-31	1181
SMP 18	o6cn06o6q	2002-02-01	1320
	o6cn06o8q	2002-02-01	1195
SMP 19	o6cn07ocq	2002-02-01	1320
	o6cn07oeq	2002-02-01	1320
SMP 25	o6cn08pqq	2002-07-16	1320
	o6cn08psq	2002-07-16	1260
SMP 27	o6cn09u5q	2002-02-02	1320
	o6cn09u7q	2002-02-02	953
SMP 28	o6cn10l5q	2001-12-09	2964
	o6cn10l7q	2001-12-09	3013
SMP 30	o6cn11vlq	2002-02-02	1320
	o6cn11vnq	2002-02-02	1260
SMP 34	o6cn12y0q	2002-07-31	1320
	o6cn12y5q	2002-07-31	1235
SMP 45	o6cn13r9q	2002-01-19	1320
	o6cn13rbq	2002-01-19	1260
SMP 46	o6cn14wfq	2002-02-02	1320
	o6cn14whq	2002-02-02	1260
SMP 48	o6cn15tvq	2001-12-11	1080

Table 1 — Continued

Name	data set	obs. date	t_{exp} [s]
	o6cn15txq	2001-12-12	753
SMP 59	o6cn16l2q	2002-01-17	2956
	o6cn16l4q	2002-01-17	1891
SMP 71	o6cn17wmq	2002-02-02	1320
	o6cn17wooq	2002-02-02	1320
SMP 72	o6cn18adq	2002-02-03	1320
	o6cn18afq	2002-02-03	1320
SMP 79	o6cn19fzq	2001-12-08	1440
	o6cn19g0q	2001-12-08	1445
SMP 80	o6cn20ags	2001-10-15	1320
	o6cn20ais	2001-10-15	1320
SMP 81	o6cn21n7q	2001-10-11	1440
	o6cn21n8q	2001-10-11	1445
SMP 93	o6cn22q2q	2002-01-24	2880
	o6cn22q4q	2002-01-24	1055
SMP 95	o6cn23lbq	2002-07-19	1320
	o6cn23leq	2002-07-19	1260
SMP 102	o6cn24l0q	2002-07-19	1320
	o6cn24l3q	2002-07-19	1260

[a]Format of table is G230L grating spectrum followed by G140L spectrum for each target

Table 2. Observed and Corrected Emission Line Flux Ratios

Name		ID	F /F	c_G	c_{LMC}	I /I	note
J41	1907/09	C iii]	1.49	0.096	0.000	1.99	
SMP 4	1175/76	C iii	0.74	0.131	0.000	1.43	
	1239/43	N v	0.25	0.131	0.000	0.44	two components
	1335/36	C ii	0.29	0.131	0.000	0.47	emission overlying absorption
	1548/50	C iv	2.49	0.131	0.000	3.62	deblended from [Ne v]
	1575	[Ne v]	0.53	0.131	0.000	0.76	deblended from C iv, id uncertain
	1640	He ii	1.51	0.131	0.000	2.16	Balmer-, Voigt profile, G140L
	1907/09	C iii]	3.09	0.131	0.000	4.59	
SMP 9	1335/36	C ii	0.14	0.079	0.154	0.43	
	1397/1407	O iv]	0.06	0.079	0.154	0.18	
	1548/50	C iv	2.33	0.079	0.154	5.68	Voigt profile
	1640	He ii	0.91	0.079	0.154	2.08	Balmer-, Voigt profile, G140L
	1640	He ii	1.37	0.079	0.154	3.11	Balmer-, Voigt profile, G230L
	1907/09	C iii]	3.75	0.079	0.154	7.94	Voigt profile
	2325-29	C ii]	1.23	0.079	0.154	2.43	
	2423/25	[Ne iv]	0.12	0.079	0.154	0.22	
	2470	[O ii]	0.07	0.079	0.154	0.13	
	2733	He ii	0.06	0.079	0.154	0.09	Paschen-
	2796/2803	Mg ii	0.23	0.079	0.154	0.34	could be 2784 [Mg v]
SMP 10	1239/43	N v	0.09	0.103	0.072	0.22	possible separate 1239 feature, P-Cygni, Voigt profile
	1548/50	C iv	0.32	0.103	0.072	0.58	
	1640	He ii	0.19	0.103	0.072	0.33	Balmer-, G140L
	1907/09	C iii]	1.59	0.103	0.072	2.76	single feature, uncertain id
SMP 16	1239/43	N v	0.36	0.088	0.063	0.80	
	1397/1407	O iv]	0.20	0.088	0.063	0.37	
	1483/87	N iv]	0.58	0.088	0.063	1.01	
	1548/50	C iv	0.41	0.088	0.063	0.70	
	1640	He ii	1.40	0.088	0.063	2.29	Balmer-, deblended from O iii], G140L
	1658-1666	O iii]	0.14	0.088	0.063	0.23	deblended from Balmer-
	1750	N iii]	0.53	0.088	0.063	0.84	
	1907/09	C iii]	0.92	0.088	0.063	1.49	
	2325-29	C ii]	0.17	0.088	0.063	0.26	deblended from [Ne iv] and [O ii], Voigt profile
	2423/25	[Ne iv]	1.01	0.088	0.063	1.47	deblended from C ii] and [O ii], Voigt profile
	2470	[O ii]	0.05	0.088	0.063	0.07	deblended from C ii] and [Ne iv], Voigt profile
SMP 18	1239/43	N v	0.69	0.076	0.000	0.96	P-Cygni
	1548/50	C iv	0.49	0.076	0.000	0.61	P-Cygni
	1907/09	C iii]	2.89	0.076	0.000	3.64	Voigt profile, G230L
	1993	C i	0.21	0.076	0.000	0.27	marginal, deblended from C iii], Voigt profile, G140L
	2325-29	C ii]	0.14	0.076	0.000	0.17	marginal, high errors
SMP 19	1247	C iii	0.11	0.076	0.117	0.31	could be 1239/43 N v
	1335/36	C ii	0.07	0.076	0.117	0.17	
	1397/1407	O iv]	0.10	0.076	0.117	0.23	
	1483/87	N iv]	0.07	0.076	0.117	0.15	
	1548/50	C iv	2.44	0.076	0.117	5.03	Voigt profile
	1640	He ii	1.22	0.076	0.117	2.38	Balmer-, G140L, Voigt, deblended from O iii]

Table 2 | Continued

Name	ID	F /F	c_G	c_{LMC}	I /I	note
1640	He ii	1.68	0.076	0.117	3.28	Balmer- , G230L, extreme edge of spectrum
1658-66	O iii]	0.21	0.076	0.117	0.40	deblended from He ii, G140L
1907/09	C iii]	6.11	0.076	0.117	11.31	
2325-29	C ii]	1.15	0.076	0.117	2.01	
2423/25	[Ne iv]	0.34	0.076	0.117	0.56	deblended from [O ii] and He ii
2470	[O ii]	0.11	0.076	0.117	0.17	deblended from C ii] and He ii
2511	He ii	0.05	0.076	0.117	0.07	Paschen- , deblended from [Ne iv] and [O ii]
2733	He ii	0.07	0.076	0.117	0.09	Paschen- , deblended from Ar v and C ii
2786	Ar v	0.06	0.076	0.117	0.08	deblended from Paschen- and C ii
2837/38	C ii	0.08	0.076	0.117	0.10	Bowen uorescence, deblended from Paschen- and Ar v
3043/47	O iii	0.14	0.076	0.117	0.18	Bowen uorescence, two components deblended
3133	O iii	0.55	0.076	0.117	0.70	Bowen uorescence, two components deblended
SMP 25 1239/43	N v	0.82	0.050	0.080	1.70	P-Cygni
1335/36	C ii	0.22	0.050	0.080	0.41	
1548/50	C iv	0.97	0.050	0.080	1.58	P-Cygni
1658-66	O iii]	0.63	0.050	0.080	0.99	marginally P-Cygni
1907/09	C iii]	1.56	0.050	0.080	2.37	
2325-29	C ii]	0.29	0.050	0.080	0.43	
2470	[O ii]	0.05	0.050	0.080	0.07	
SMP 27 1239/43	N v	0.98	0.184	0.000	2.20	P-Cygni
1548/50	C iv	0.59	0.184	0.000	1.01	P-Cygni
1907/09	C iii]	1.85	0.184	0.000	3.23	
2325-29	C ii]	0.17	0.184	0.000	0.30	
SMP 28 1239/43	N v	0.86	0.046	0.281	6.24	
1397/14037	O iv]	0.05	0.046	0.281	0.26	uncertain id, 3-line blend
1397-1407	O iv]	0.08	0.046	0.281	0.37	uncertain id, 3-line blend
1397-1407	O iv]	0.08	0.046	0.281	0.36	uncertain id, 3-line blend
1483/87	N iv]	0.27	0.046	0.281	1.14	
1548/50	C iv	0.08	0.046	0.281	0.30	
1640	He ii	0.34	0.046	0.281	1.19	Balmer- , G140L, Voigt pro le
1640	He ii	0.63	0.046	0.281	2.19	Balmer- , G230L
1658-1666	O iii]	0.15	0.046	0.281	0.52	G140L
1658-1666	O iii]	0.22	0.046	0.281	0.75	G230L
1747-1754	N iii]	0.45	0.046	0.281	1.40	marginally double feature
1892	Si iii]	0.16	0.046	0.281	0.47	deblended from C iii]
1907/09	C iii]	0.13	0.046	0.281	0.37	deblended from Si iii
2145	:::	0.08	0.046	0.281	0.23	not identi ed
2334-50	[S ii]	0.12	0.046	0.281	0.29	
2423/25	[Ne iv]	0.12	0.046	0.281	0.28	Voigt pro le
2470	[O ii]	0.09	0.046	0.281	0.19	Voigt pro le
2511	He ii	0.03	0.046	0.281	0.05	Paschen-
2629	Fe ii?	0.06	0.046	0.281	0.11	
2837/38	C ii	0.12	0.046	0.281	0.20	Bowen uorescence
3133	O iii	0.16	0.046	0.281	0.24	Bowen uorescence
SMP 30 1397/1407	O iv]	0.19	0.176	0.000	0.35	

Table 2 | Continued

Name		ID	F /F	c_G	c_{LMC}	I /I	note
	1483/87	N iv]	0.80	0.176	0.000	1.36	
	1548/50	C iv	0.35	0.176	0.000	0.58	
	1640	He ii	2.26	0.176	0.000	3.66	Balmer-, Voigt profile, G140L
	1747-1754	N iii]	1.56	0.176	0.000	2.51	noisy, smoothed with box=3
	1907/09	C iii]	0.86	0.176	0.000	1.46	noisy, smoothed with box=3
	2423/25	[Ne iv]	0.67	0.176	0.000	1.03	
SMP 34	1239/43	N v	0.07	0.047	0.024	0.10	P-Cygni
	1548/50	C iv	0.12	0.047	0.024	0.15	P-Cygni
	1907/09	C iii]	0.89	0.047	0.024	1.11	
	2325-29	C ii]	0.16	0.047	0.024	0.19	could be 2321/31 [O iii]
SMP 45	1548/50	C iv	0.14	0.162	0.000	0.22	
	1640	He ii	0.25	0.162	0.000	0.39	Balmer-, G140L
	1907/09	C iii]	0.79	0.162	0.000	1.28	low S/N
SMP 46	1548/50	C iv	1.01	0.069	0.116	2.05	Voigt profile
	1640	He ii	0.51	0.069	0.116	0.97	Balmer-, G140L
	1658-1666	O iii]	0.08	0.069	0.116	0.15	
	1907/09	C iii]	3.39	0.069	0.116	6.14	
	2325-29	C ii]	1.19	0.069	0.116	2.04	
	2423/25	[Ne iv]	0.10	0.069	0.116	0.15	deblended from [O ii]
	2470	[O ii]	0.13	0.069	0.116	0.19	deblended from [Ne iv]
	3133	O iii	0.24	0.069	0.116	0.31	low S/N, Bowen fluorescence
SMP 48	1239/43	N v	0.01	0.147	0.000	0.026	
	1548/50	C iv	0.02	0.147	0.000	0.04	P-Cygni, Voigt profile
	1658-1666	O iii]	0.04	0.147	0.000	0.06	Voigt profile
	1907/09	C iii]	1.13	0.147	0.000	1.76	Voigt profile
	2325-29	C ii]	0.29	0.147	0.000	0.45	Voigt profile
	2470	[O ii]	0.06	0.147	0.000	0.09	
	2837	O iii	0.02	0.147	0.000	0.02	Bowen fluorescence
SMP 59	1483/87	N iv]	0.22	0.097	0.000	0.29	
	1548/50	C iv	0.19	0.097	0.000	0.25	
	1640	He ii	0.68	0.097	0.000	0.88	Balmer-, Voigt profile, G140L
	1907/09	C iii]	0.50	0.097	0.000	0.67	low S/N spectrum
	2306	He ii	0.10	0.097	0.000	0.14	low S/N, Paschen-, deblended from [Ne iv]
	2423/25	[Ne iv]	0.36	0.097	0.000	0.46	low S/N, deblended from He ii
SMP 71	1335/36	C ii	0.18	0.062	0.182	0.60	marginal feature, smoothed with box=3
	1397/1407	O iv]	0.12	0.062	0.182	0.37	Voigt profile
	1483/87	N iv]	0.04	0.062	0.182	0.12	
	1520	:::	0.01	0.062	0.182	0.02	not identified
	1548/50	C iv	3.33	0.062	0.182	8.75	
	1575	[Ne v]	0.04	0.062	0.182	0.09	deblended from [Ne iv]
	1602	[Ne iv]	0.03	0.062	0.182	0.06	deblended from [Ne v]
	1640	He ii	0.95	0.062	0.182	2.32	Balmer-, Voigt function, deblended from O iii, G140L
	1640	He ii	1.27	0.062	0.182	3.09	Balmer-, Voigt function, G230L
	1658-1666	O iii]	0.10	0.062	0.182	0.25	deblended from He ii, G140L
	1907/09	C iii]	4.21	0.062	0.182	9.29	

Table 2 | Continued

Name		ID	F /F	c_G	c_{LMC}	I /I	note
	2306	He ii	0.10	0.062	0.182	0.21	marginal, Paschen- , deblended from C ii]
	2325-29	C ii]	0.52	0.062	0.182	1.06	Voigt pro le, deblended from He ii
	2423/25	[Ne iv]	0.21	0.062	0.182	0.38	
	2470	[O ii]	0.05	0.062	0.182	0.08	
	2511	He ii	0.02	0.062	0.182	0.03	marginal, Paschen-
	2733	He ii	0.06	0.062	0.182	0.09	Paschen-
	2784	[Mg v]?	0.04	0.062	0.182	0.06	Possibly 2786 [Ar v]
	2837/38	C ii	0.05	0.062	0.182	0.08	Bowen uorescence
	3023	O iii	0.02	0.062	0.182	0.03	marginal, Bowen uor., deblended from 3043/47 O iii
	3043/47	O iii	0.08	0.062	0.182	0.10	Bowen uorescence, deblended from 3023 O iii
	3133	O iii	0.42	0.062	0.182	0.57	Bowen uorescence
SMP 72	1397/1407	O iv]	0.61	0.191	0.000	1.15	di use spectrum
	1548/50	C iv	4.37	0.191	0.000	7.54	
	1640	He ii	3.45	0.191	0.000	5.81	Balmer- , G140L
	1907/09	C iii]	4.80	0.191	0.000	8.55	
	2423/25	[Ne iv]	1.09	0.191	0.000	1.75	
SMP 79	1175/76	C iii	0.16	0.221	0.000	0.48	
	1239/43	N v	0.07	0.221	0.000	0.19	marginally P-Cygni
	1335/36	C ii	0.06	0.221	0.000	0.13	
	1371	O v	0.06	0.221	0.000	0.12	marginally P-Cygni
	1548/50	C iv	0.90	0.221	0.000	1.69	Voigt pro le
	1575	[Ne v]	0.04	0.221	0.000	0.07	
	1640	He ii	0.39	0.221	0.000	0.72	Balmer- , Voigt pro le, G140L
	1640	He ii	0.33	0.221	0.000	0.61	Balmer- , G230L
	1658-1666	O iii]	0.07	0.221	0.000	0.12	
	1907/09	C iii]	4.50	0.221	0.000	8.77	Voigt pro le
	2297	C iii	0.05	0.221	0.000	0.11	deblended from C ii]
	2325-29	C ii]	0.62	0.221	0.000	1.20	deblended from C iii
	2423/25	[Ne iv]	0.01	0.221	0.000	0.02	
	2470	[O ii]	0.06	0.221	0.000	0.09	
	2733	He ii	0.02	0.221	0.000	0.03	Paschen-
	2784/2929	Mg v	0.01	0.221	0.000	0.02	
	2837/38	C ii	0.04	0.221	0.000	0.05	P-Cygni
	3043/47	O iii	0.03	0.221	0.000	0.04	Bowen uorescence
	3133	O iii	0.15	0.221	0.000	0.19	Bowen uorescence
SMP 80	1239/43	N v	0.02	0.044	0.046	0.04	P-Cygni
	1548/50	C iv	0.06	0.044	0.046	0.08	low S/N, P-Cygni, Voigt pro le
	1907/09	C iii]	0.23	0.044	0.046	0.30	
	2325-29	C ii]	0.08	0.044	0.046	0.05	marginal feature
SMP 81	1239/43	N v	0.04	0.221	0.056	0.14	P-Cygni
	1483/87	N iv]	0.01	0.221	0.056	0.02	marginal feature
	1548/50	C iv	0.03	0.221	0.056	0.06	
	1658-1666	O iii]	0.03	0.221	0.056	0.06	two components deblended, G140L
	1658-1666	O iii]	0.06	0.221	0.056	0.14	two components deblended, G140L
	1658-1666	O iii]	0.07	0.221	0.056	0.16	primary spatial component, G230L

Table 2 | Continued

Name		ID	F /F	c_G	c_{LMC}	I /I	note
	1658-1666	O iii]	0.08	0.221	0.056	0.18	two spatial components summed, G230L
	1747-1754	N iii]	0.03	0.221	0.056	0.06	primary spatial component
	1747-1754	N iii]	0.04	0.221	0.056	0.08	two spatial components
	1892	Si iii]	0.04	0.221	0.056	0.10	primary spatial component, deblended from C iii]
	1892	Si iii]	0.03	0.221	0.056	0.07	two spatial components, deblended from C iii]
	1907/09	C iii]	0.18	0.221	0.056	0.42	primary spatial component, deblended from Si iii]
	1907/09	C iii]	0.26	0.221	0.056	0.62	two spatial components, deblended from Si iii]
	2321/31	[O iii]	0.05	0.221	0.056	0.10	primary spatial component
	2321/31	[O iii]	0.05	0.221	0.056	0.12	two spatial components
	2470	[O ii]	0.04	0.221	0.056	0.076	primary spatial component
	2470	[O ii]	0.04	0.221	0.056	0.077	two spatial components
SMP 93	1483/87	N iv]	0.15	0.056	0.000	0.17	diuse, low S/N spectrum
	1548/50	C iv	0.18	0.056	0.000	0.21	marginal feature
	1640	He ii	0.52	0.056	0.000	0.60	Balmer- , G140L
	1907/09	C iii]	0.49	0.056	0.000	0.58	low S/N
	2325-29	C ii	0.28	0.056	0.000	0.33	low S/N
SMP 95	1335/36	C ii	0.18	0.096	0.031	0.31	
	1397-1407	O iv]	0.06	0.096	0.031	0.09	
	1548/50	C iv	1.84	0.096	0.031	2.76	
	1640	He ii	1.40	0.096	0.031	2.05	Balmer- , G140L
	1640	He ii	1.90	0.096	0.031	2.78	Balmer- , G230L
	1907/09	C iii]	4.96	0.096	0.031	7.33	
	2325-29	C ii]	1.69	0.096	0.031	2.46	
	2423/25	[Ne iv]	0.11	0.096	0.031	0.15	
	2796/2803	Mg ii	0.09	0.096	0.031	0.11	
SMP 102	1342	O iv	0.04	0.162	0.000	0.07	marginal feature
	1548/50	C iv	4.86	0.162	0.000	7.72	Voigt prole
	1640	He ii	2.59	0.162	0.000	4.03	Balmer- , G140L
	1907/09	C iii]	6.16	0.162	0.000	10.0	
	2321/31	[O iii]	0.47	0.162	0.000	0.77	
	2423/25	[Ne iv]	0.34	0.162	0.000	0.51	
	2511	He ii	0.09	0.162	0.000	0.13	Paschen-
	2733	He ii	0.23	0.162	0.000	0.30	Paschen-
	3043/47	O iii	0.15	0.162	0.000	0.18	low S/N, Bowen uorescence
	3133	O iii	0.39	0.162	0.000	0.47	low S/N, Bowen uorescence

Table 3. Velocities from P-Cygni profiles

Name	[Å]	ID	v_1 [km s^{-1}]
SMP 18	1239/43	N v	1670
	1548/50	C iv	1570
SMP 25	1239/43	N v	1830
	1548/50	C iv	1900
SMP 27	1239/43	N v	1840
	1548/50	C iv	1770
SMP 34	1239/43	N v	(1680)[a]
	1548/50	C iv	1920
SMP 48	1239/43	N v	(2200)[a]
	1548/50	C iv	1320
SMP 79	1371	O v	(3200)[a]
	2837/38	C ii	4200
SMP 80	1239/43	N v	3000
	1548/50	C iv	2800
SMP 81	1239/43	N v	(3042)[a]

[a]very uncertain measurement, low S/N

Table 4. Plasma Diagnostics and Nebular Excitation Class

Name	N_e			T_e			EC
	low	medium	high	low	medium	high	
J 41	500	500	500	10000	10000	10000	
SMP 4	5000	5000	5000	11800	11800	11800	
SMP 9	3000	3000	3000	14800	14800	14800	6–7
SMP 10	2800	2800	2800	17900	17900	17900	6–7
SMP 16	600	600	600	12000	19800	19800	8
SMP 18	400	400	400	11600	11600	11600	2–6
SMP 19	3000	4000	4000	12000	13000	13500	7
SMP 25	16600	16600	16600	10900	13000	13000	
SMP 27	500	500	500	11500	17200	17200	3–6
SMP 28	2000	2000	2000	10000	10000	10000	6–7
SMP 30	400	400	400	12300	15700	15700	8
SMP 34	5000	5000	5000	10000	10000	10000	2
SMP 45	1000	1000	1000	16300	16300	16300	6
SMP 46	2500	2500	2500	11800	11800	11800	6
SMP 48	1900	1900	1900	8800	11300	11300	3–4
SMP 59	200	200	200	12400	15000	15000	7–9?
SMP 71	7500	10000	10000	11500	12800	12800	6–7
SMP 72	100	100	100	16000	16000	16000	7
SMP 79	3100	3100	3100	13600	12900	12900	5
SMP 80	4500	8700	8700	12500	9800	10000	2–4
SMP 81	10000	20000	20000	15000	15000	15000	5
SMP 93	300	300	300	11000	17100	17100	8
SMP 95	1000	1000	1000	11300	12700	12700	5–7
SMP 102	1000	1000	1000	13700	13700	13700	7

Table 5. Emission Lines Used for Ionic Abundances

Ion	Spectrum	Wavelengths (Å)	Ionization Zone
C^{+}	C II]	2326+2328	Low
C^{2+}	C III]	1907+1909	Med
C^{3+}	C IV[a]	1548+1550	Med
N^{2+}	N III]	1749+1752	Med
N^{3+}	[N IV]	1483+1487	Med
N^{4+}	N V[a]	1239+1243	High
O^{3+}	O III]	1400+1401+1405+1407	High
Ne^{3+}	Ne IV]	2423+2425	High

[a]Abundance not derived in nebular software

Table 6. Ionic Abundances

Name (1)	C^{+}/H^{+} (2)	C^{2+}/H^{+} (3)	C^{3+}/H^{+} (4)	C/H (5)	N^{2+}/H^{+} (6)	N^{3+}/H^{+} (7)	N^{4+}/H^{+} (8)	O^{3+} (9)	Ne^{3+}/H^{+} (10)
J41		9.80e-05		9.80e-05					
SMP04		2.27e-04	2.27e-04	4.54e-04				2.10e-04	
SMP09	5.42e-05	1.52e-04	6.59e-05	2.72e-04					4.90e-05 5.44e-06
SMP10		2.02e-05	2.09e-06	2.23e-05				3.09e-06	
SMP16	1.30e-05	6.96e-06	1.46e-06	2.14e-05	1.50e-05	1.25e-05	5.74e-06	2.19e-05	1.12e-05
SMP18	1.42e-05	1.79e-04	4.41e-05	2.38e-04				5.45e-04	
SMP19	9.80e-05	4.61e-05	1.47e-04	2.91e-04		3.09e-05			1.46e-04 2.15e-05
SMP25	4.91e-05	9.76e-05	4.62e-05	1.93e-04				3.15e-04	
SMP27	3.65e-05	2.85e-05	4.59e-06	6.96e-05				4.09e-05	
SMP28		1.83e-05	8.29e-05	1.01e-04	3.52e-03	1.75e-03	1.87e-02		5.53e-05
SMP30		5.11e-05	4.59e-06	5.57e-05	2.80e-04	6.15e-05			6.51e-05 1.91e-05
SMP34	3.76e-05	5.50e-05	4.14e-05	1.34e-04				2.90e-04	
SMP45		3.67e-05	1.38e-06	3.81e-05					
SMP46	1.46e-04	3.03e-04	1.29e-04	5.78e-04					1.13e-05
SMP48	2.18e-04	3.13e-05	3.62e-06	2.53e-04				1.95e-05	
SMP59		1.19e-05	2.66e-06	1.45e-05		1.75e-05			1.03e-05
SMP71	8.80e-05	4.19e-04	2.88e-04	7.94e-04		2.22e-05			2.62e-04 2.01e-05
SMP72		1.08e-04	5.30e-05	1.61e-04					1.92e-04 2.98e-05
SMP79	4.02e-05	3.74e-04	5.23e-05	4.67e-04				3.73e-05	9.49e-07
SMP80	5.20e-06	5.37e-06	2.21e-05	3.27e-05				1.17e-04	
SMP81	2.51e-06	1.12e-05	6.38e-07	1.44e-05	7.46e-06	2.69e-06	7.65e-06		
SMP93	3.57e-05	5.26e-06	9.87e-07	4.19e-05		4.61e-06			
SMP95	2.26e-04	3.44e-04	9.64e-05	6.67e-04					7.49e-06
SMP102		2.96e-04	1.53e-04	4.50e-04					1.75e-05

Table 7. Average C/H abundances

	median	mean	sigma	N
R	3.16e-04	3.23e-04	3.59e-04	8
E	3.39e-04	5.11e-04	4.88e-04	8
BC	2.91e-04	3.19e-04	2.06e-04	14
B	3.81e-05	3.58e-05	1.93e-05	8
P	1.01e-04	6.17e-05	5.60e-05	2

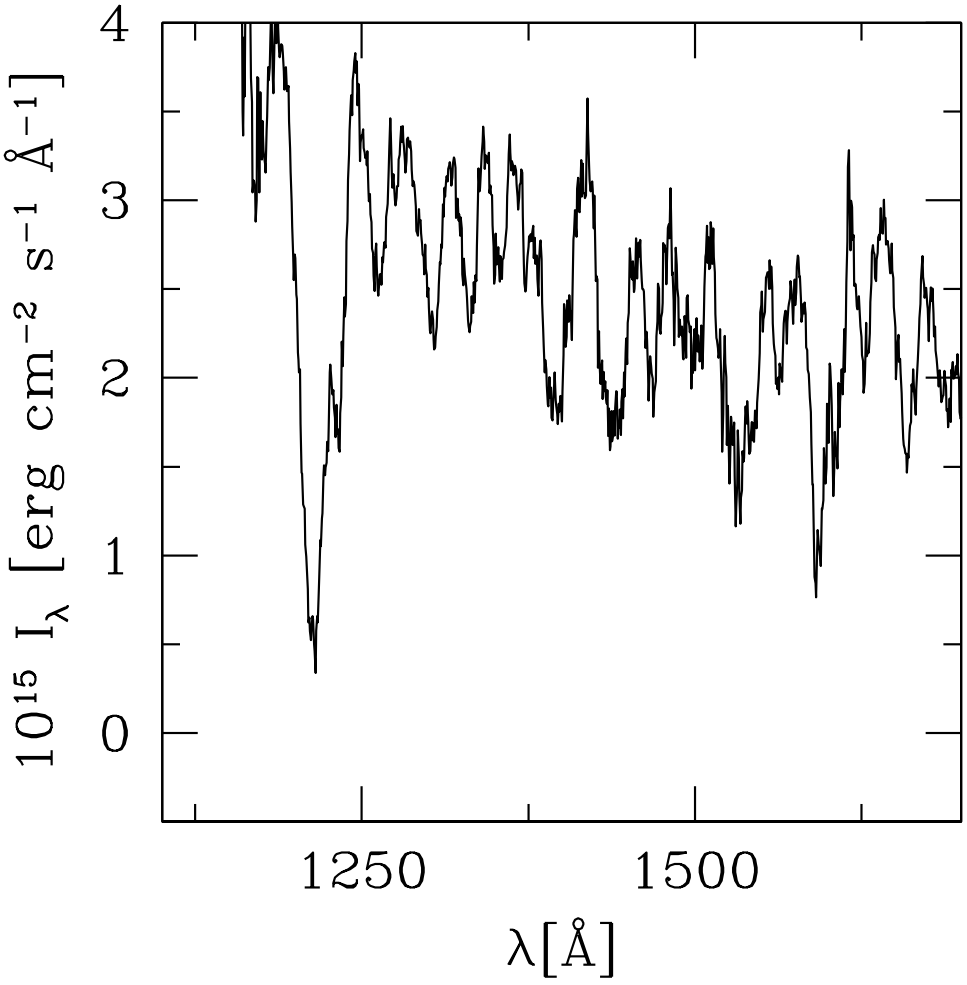
4
3
2
1
0
10^{15} I_λ [erg cm^{-2} s^{-1} Å^{-1}]
1250
1500
λ[Å]

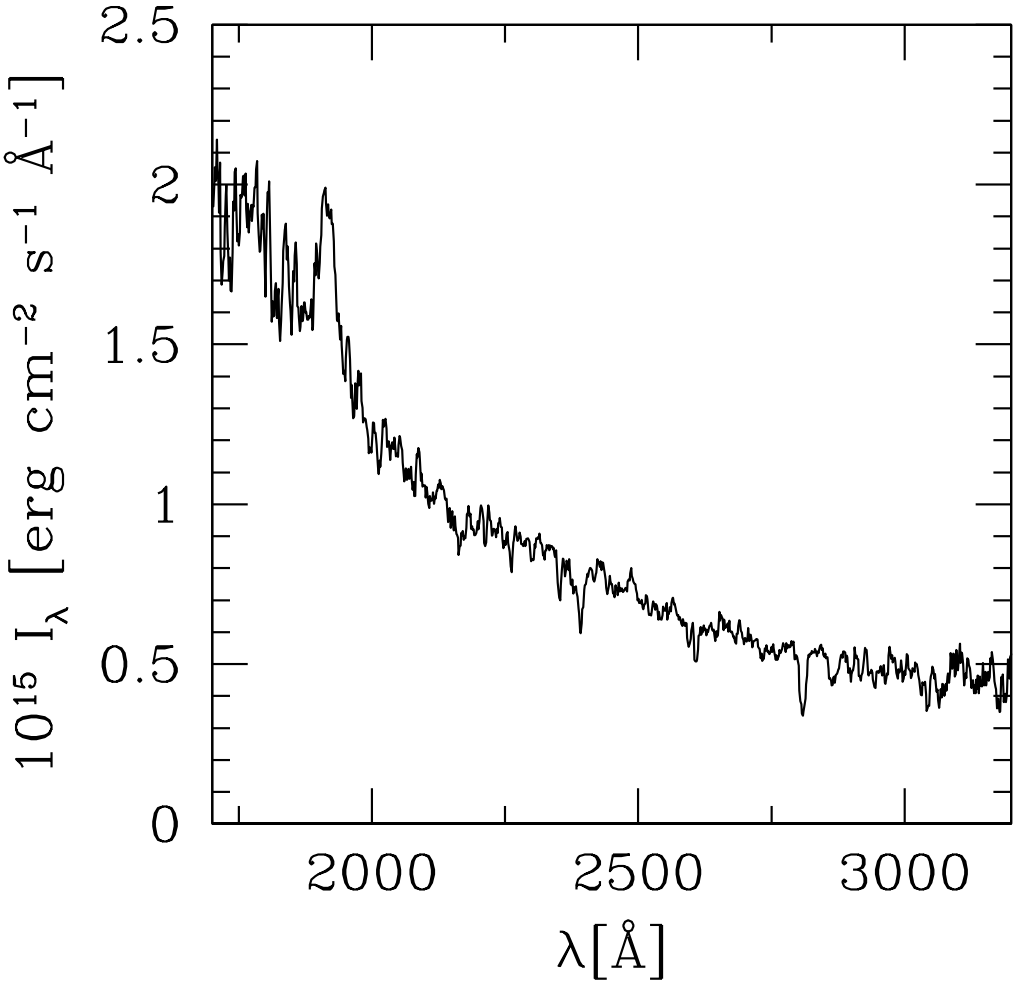
2.5
2
1.5
1
0.5
0
10^{15} I_λ [erg cm^{-2} s^{-1} Å^{-1}]
2000
2500
3000
λ[Å]

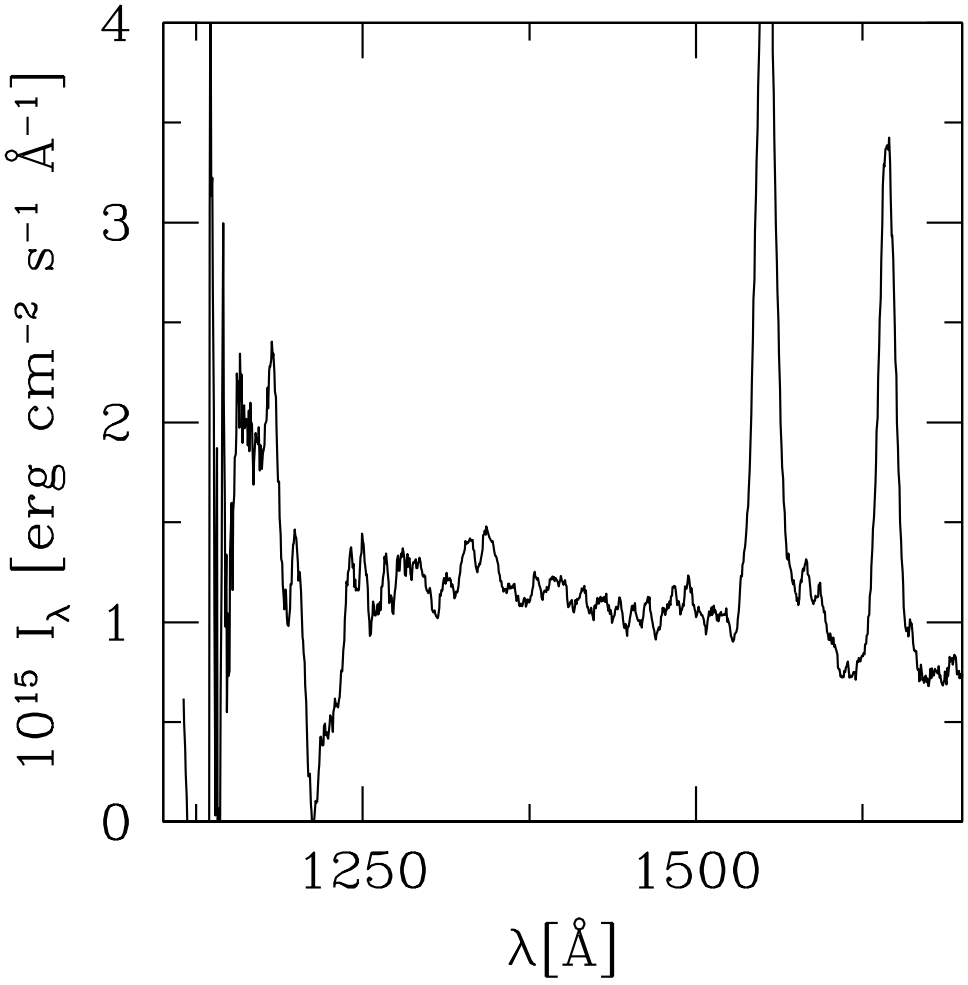
4
3
2
1
0
10^{15} I_λ [erg cm^{-2} s^{-1} Å^{-1}]
1250
1500
λ[Å]

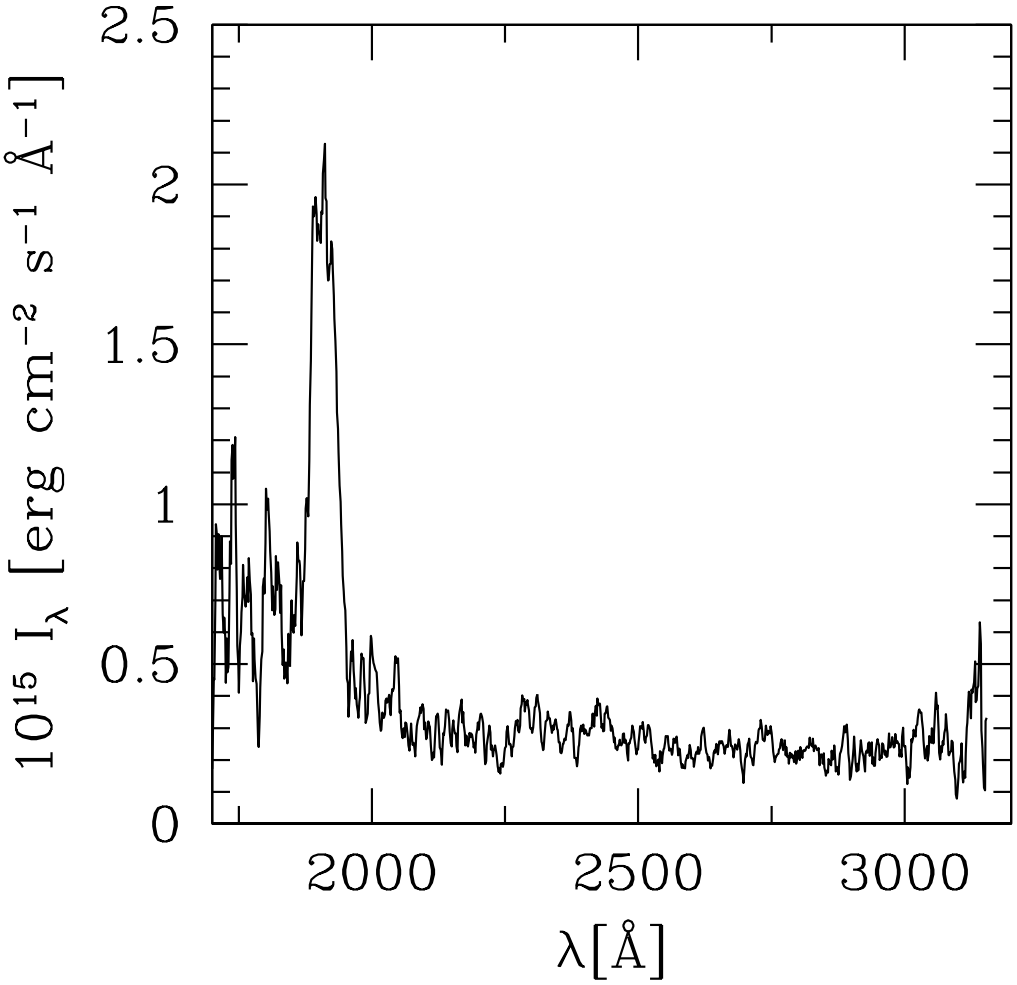
2.5
2
1.5
1
0.5
0
2000
2500
3000
λ[Å]
10¹⁵ I_λ [erg cm⁻² s⁻¹ Å⁻¹]

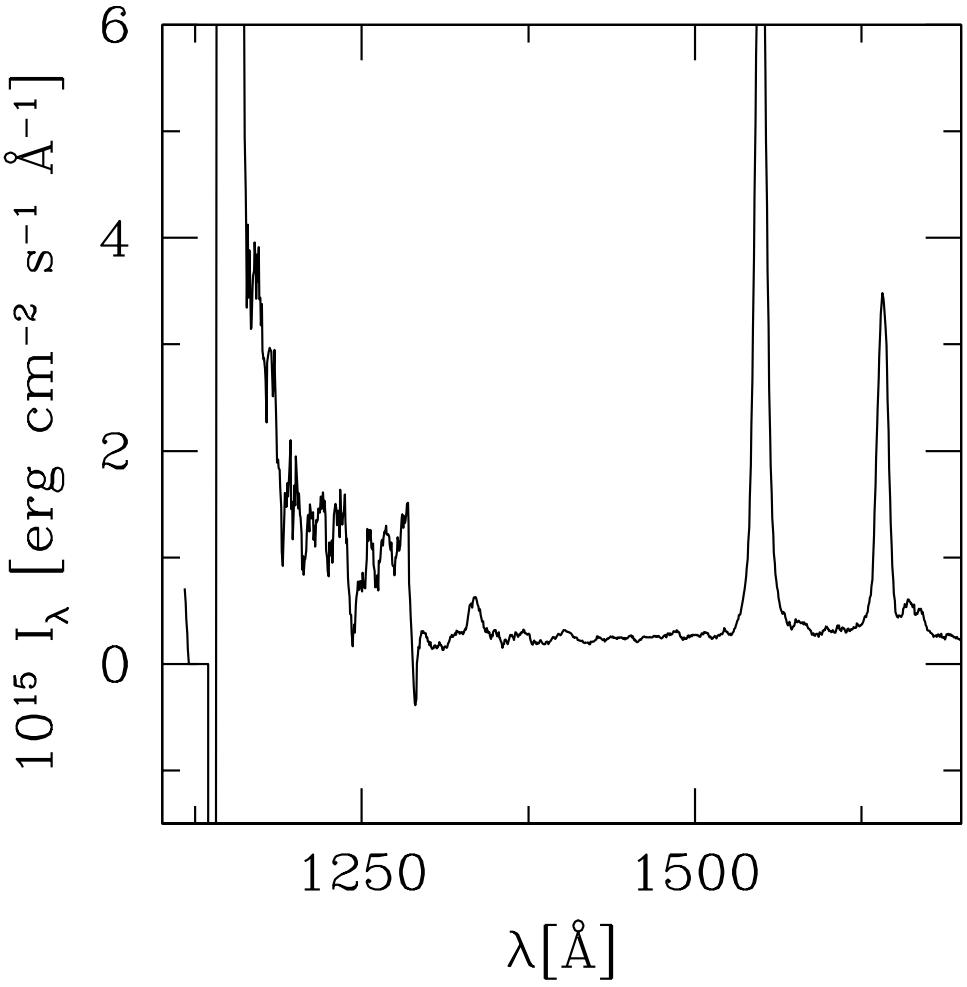
6
4
2
0
10^{15} I_λ [erg cm^{-2} s^{-1} Å^{-1}]
1250
1500
λ[Å]

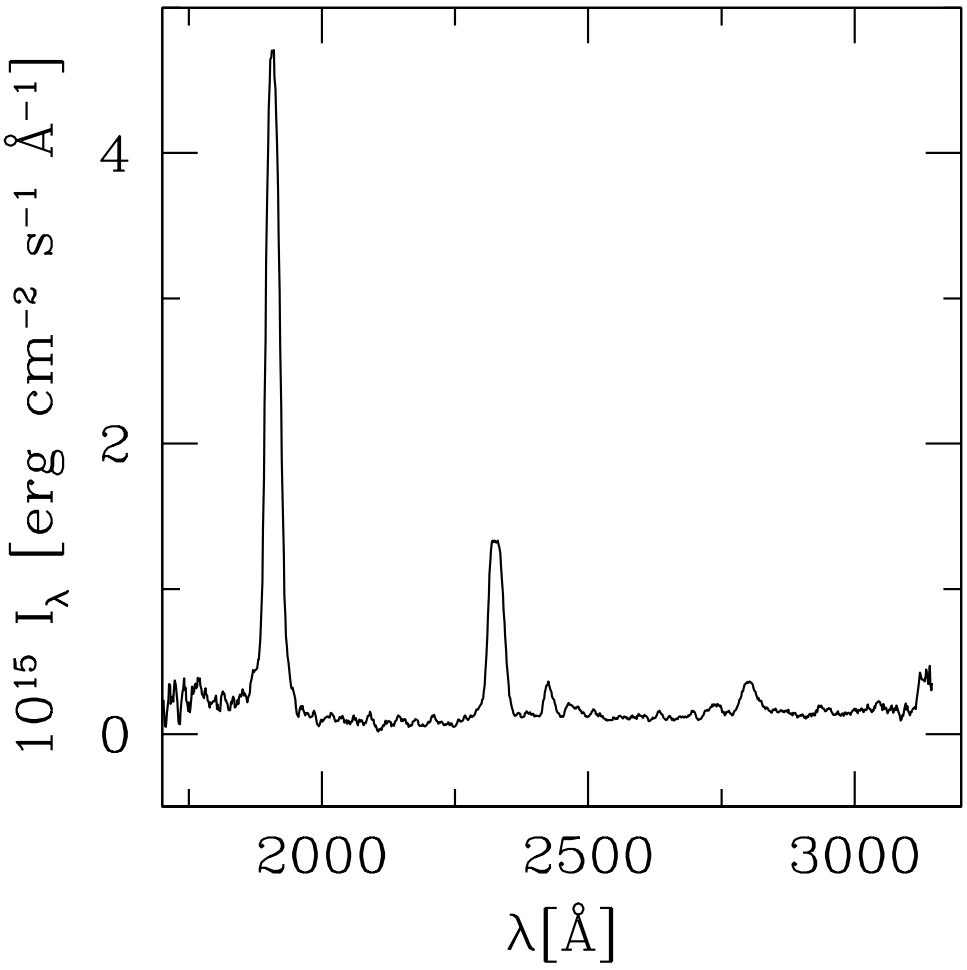
10^{15} I_λ [erg cm^{-2} s^{-1} Å^{-1}]
0
2
4
2000
2500
3000
λ[Å]

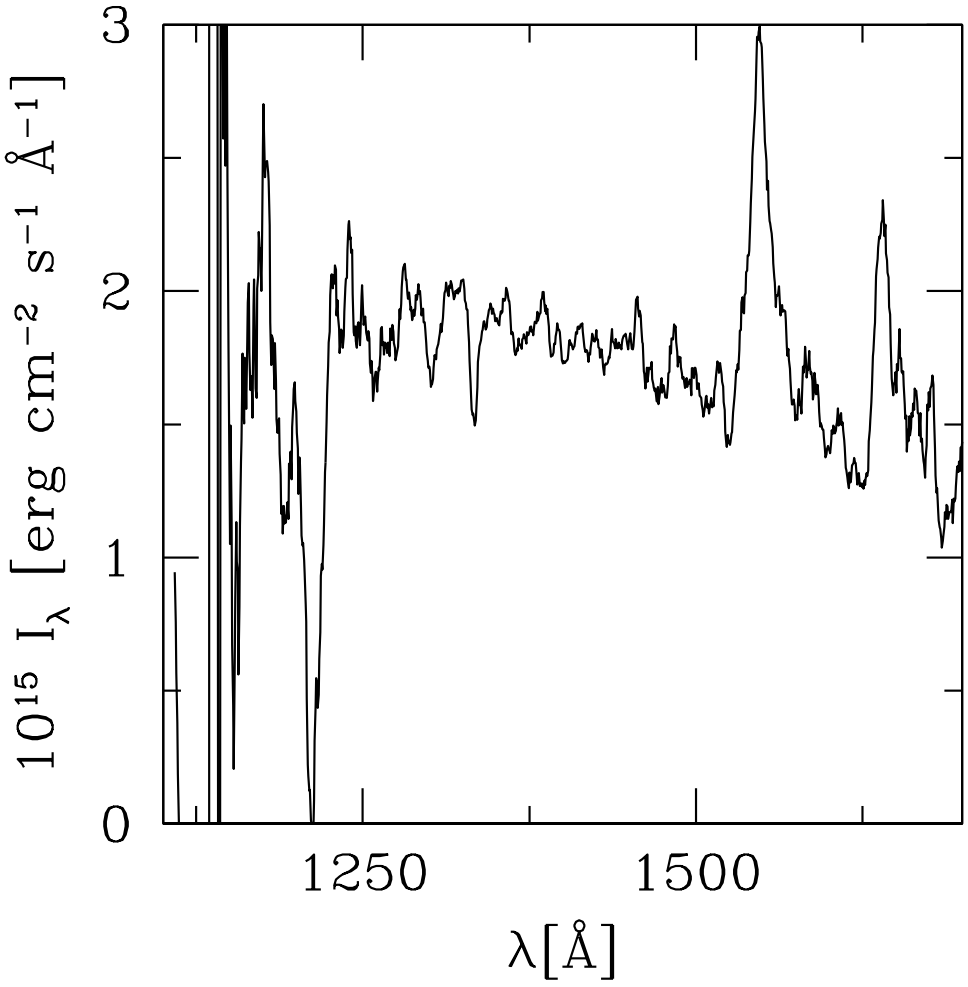
3
2
1
0
1250
1500
λ[Å]
10¹⁵ I_λ [erg cm⁻² s⁻¹ Å⁻¹]

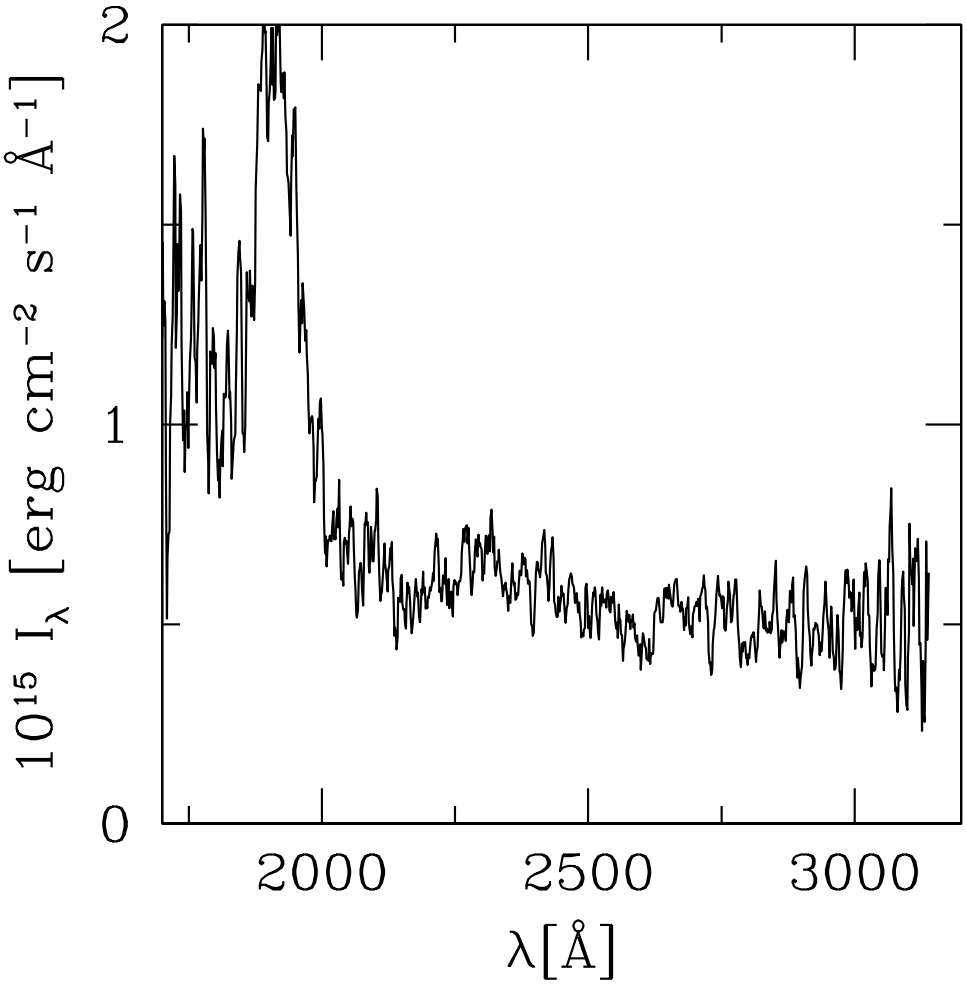
2
1
0
10^{15} I_λ [erg cm^{-2} s^{-1} Å^{-1}]
2000
2500
3000
λ[Å]

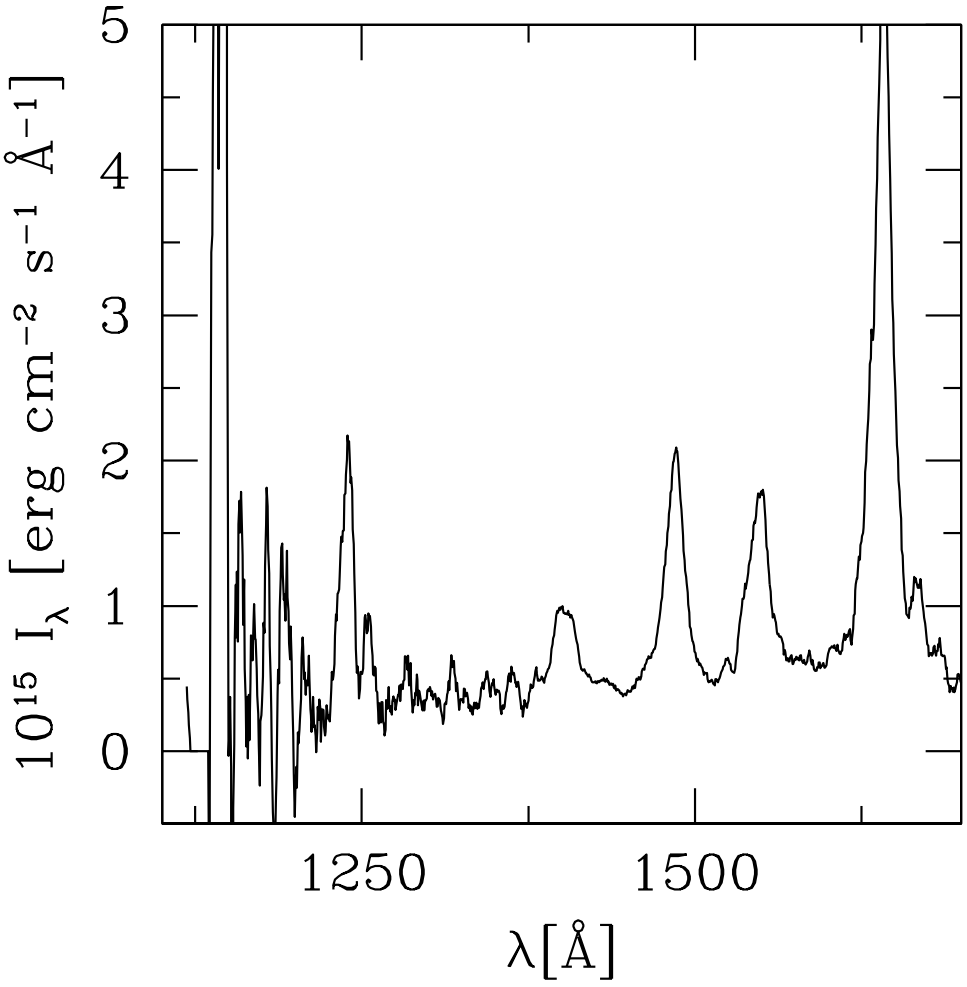
5
4
3
2
1
0
10^{15} I_λ [erg cm^{-2} s^{-1} Å^{-1}]
1250
1500
λ[Å]

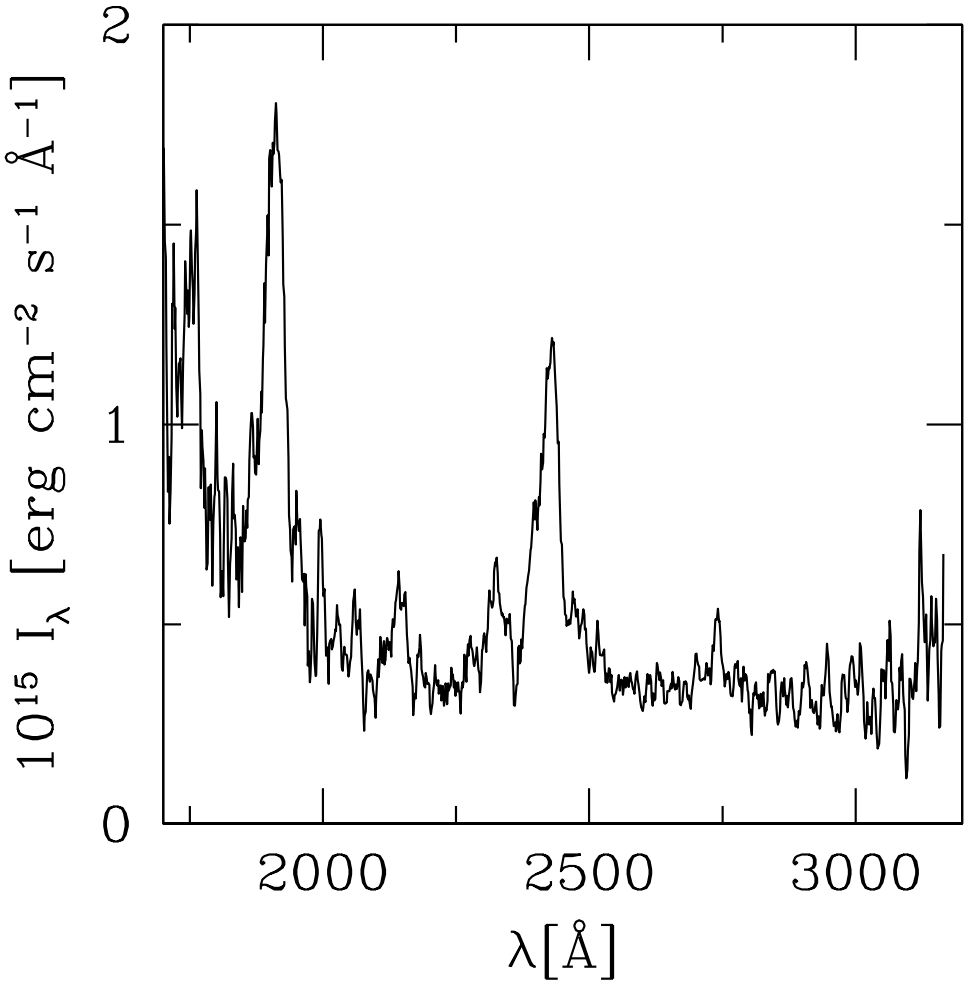
2
1
0
10^{15} I_λ [erg cm^{-2} s^{-1} Å^{-1}]
2000
2500
3000
λ[Å]

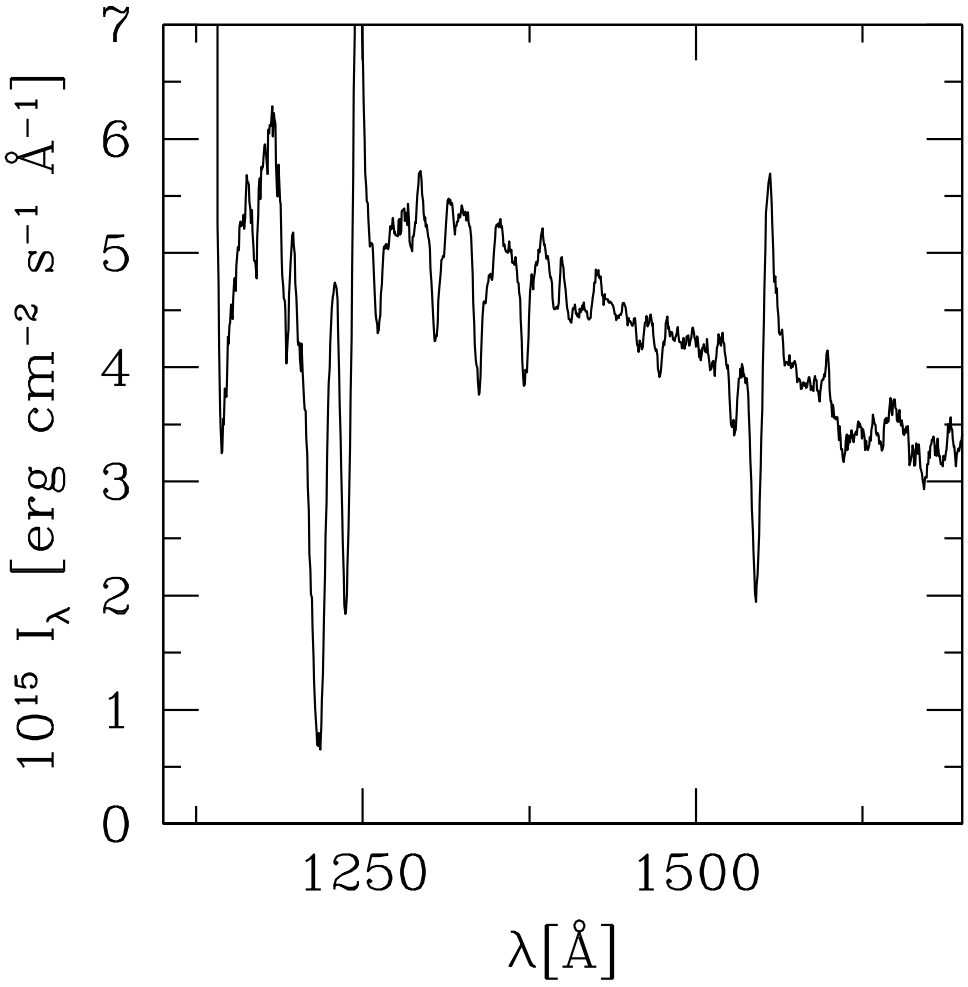
0
1
2
3
4
5
6
7
1250
1500
λ[Å]
10^{15} I_λ [erg cm^{-2} s^{-1} Å^{-1}]

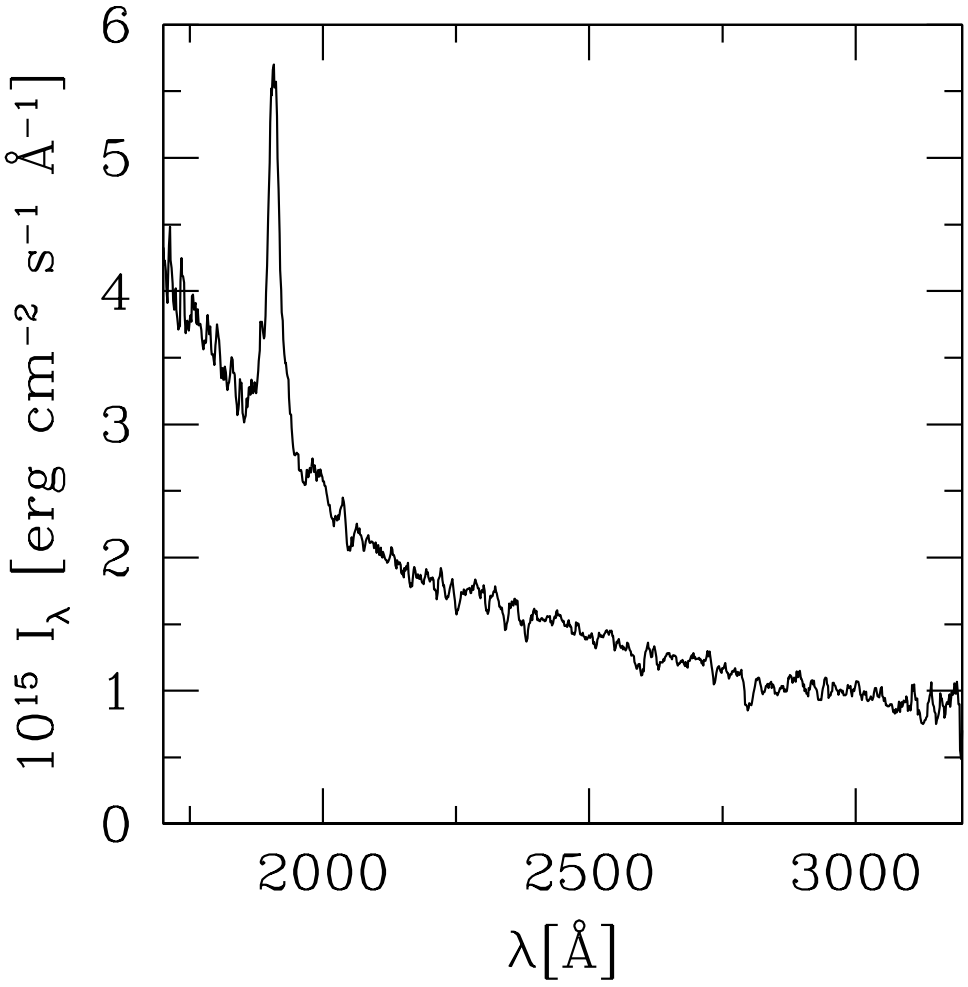
6
5
4
3
2
1
0
10^{15} I_λ [erg cm^{-2} s^{-1} Å^{-1}]
2000
2500
3000
λ[Å]

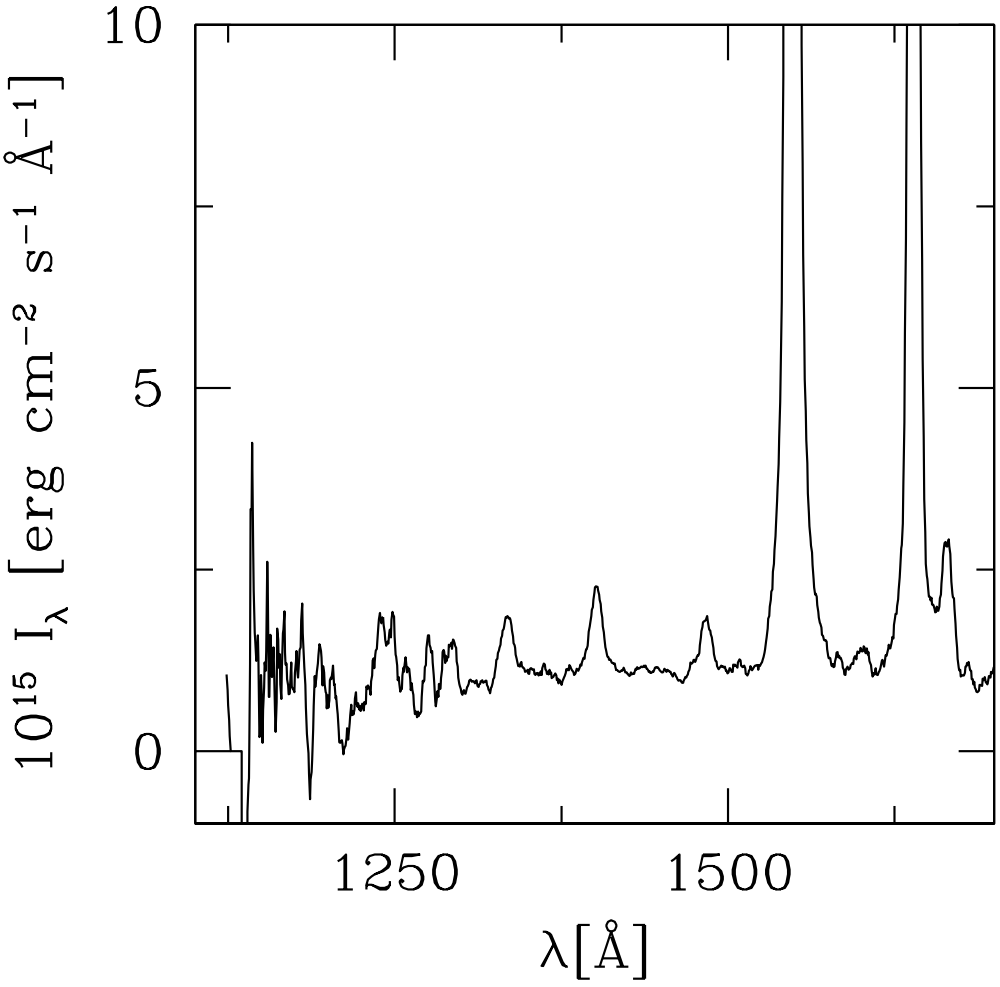
10
5
0
10^{15} I_λ [erg cm^{-2} s^{-1} Å^{-1}]
1250
1500
λ[Å]

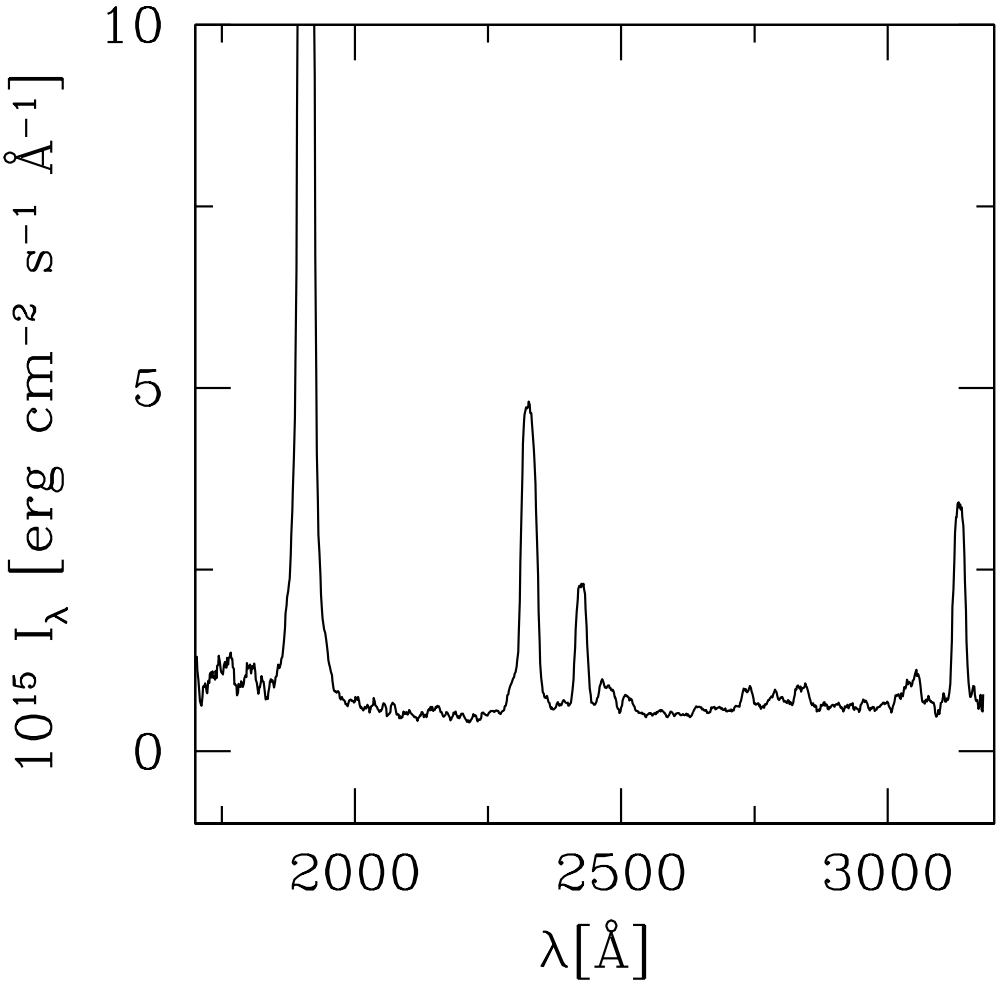
10
5
0
10^{15} I_λ [erg cm^{-2} s^{-1} Å^{-1}]
2000
2500
3000
λ[Å]

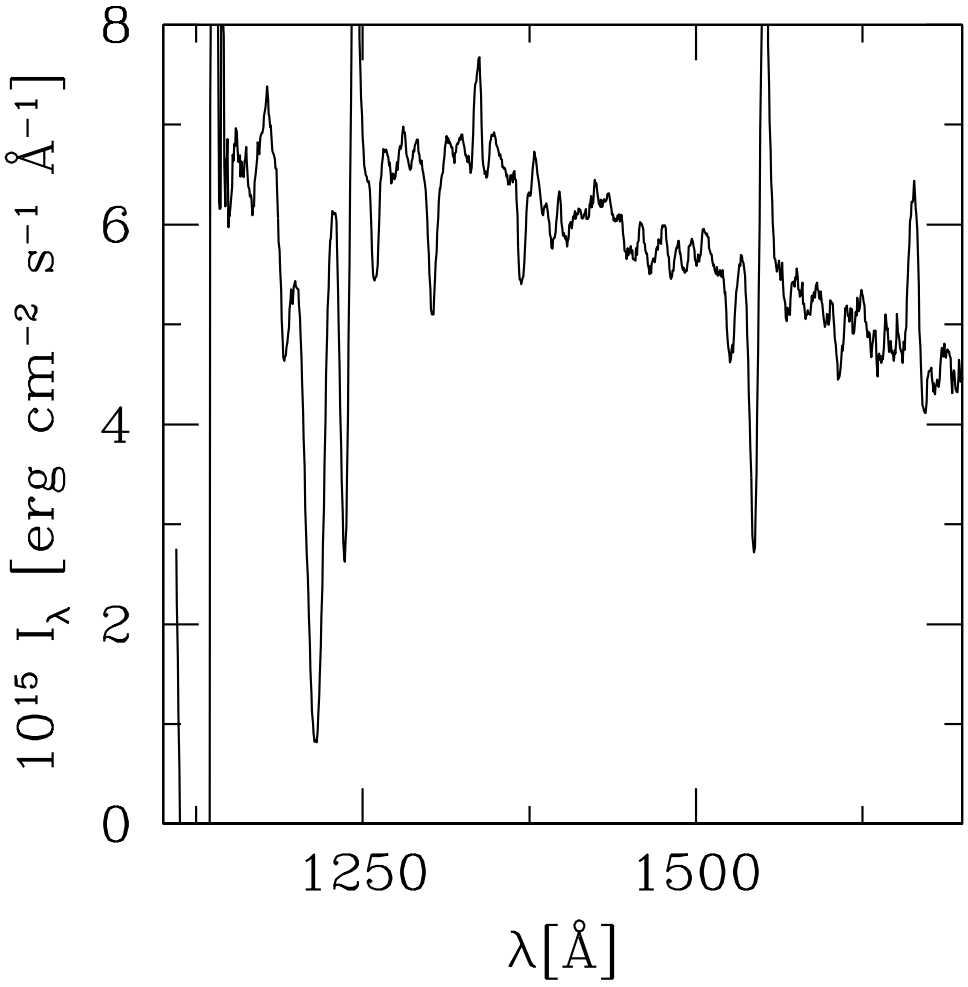
8
6
4
2
0
10^{15} I_λ [erg cm^{-2} s^{-1} Å^{-1}]
1250
1500
λ[Å]

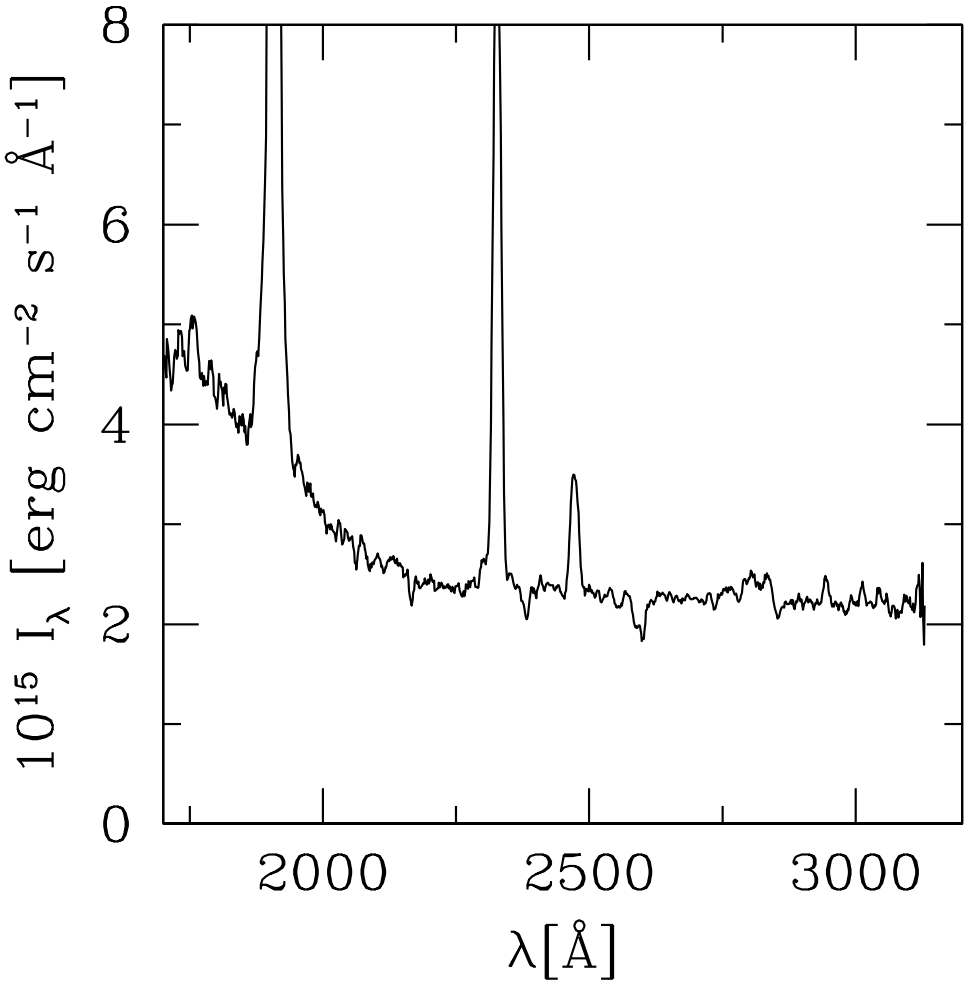
8
6
4
2
0
2000
2500
3000
λ[Å]
10^{15} I_λ [erg cm^{-2} s^{-1} Å^{-1}]

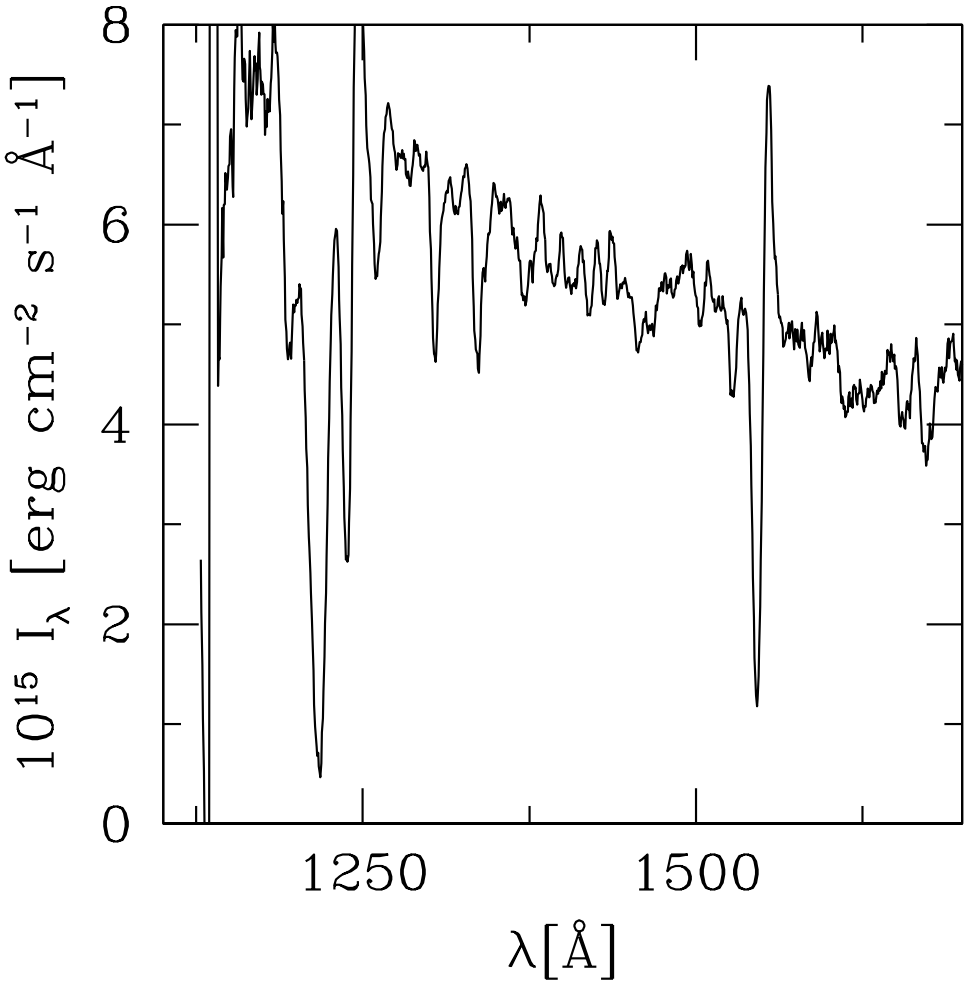
8
6
4
2
0
1250
1500
λ[Å]
10^{15} I_λ [erg cm^{-2} s^{-1} Å^{-1}]

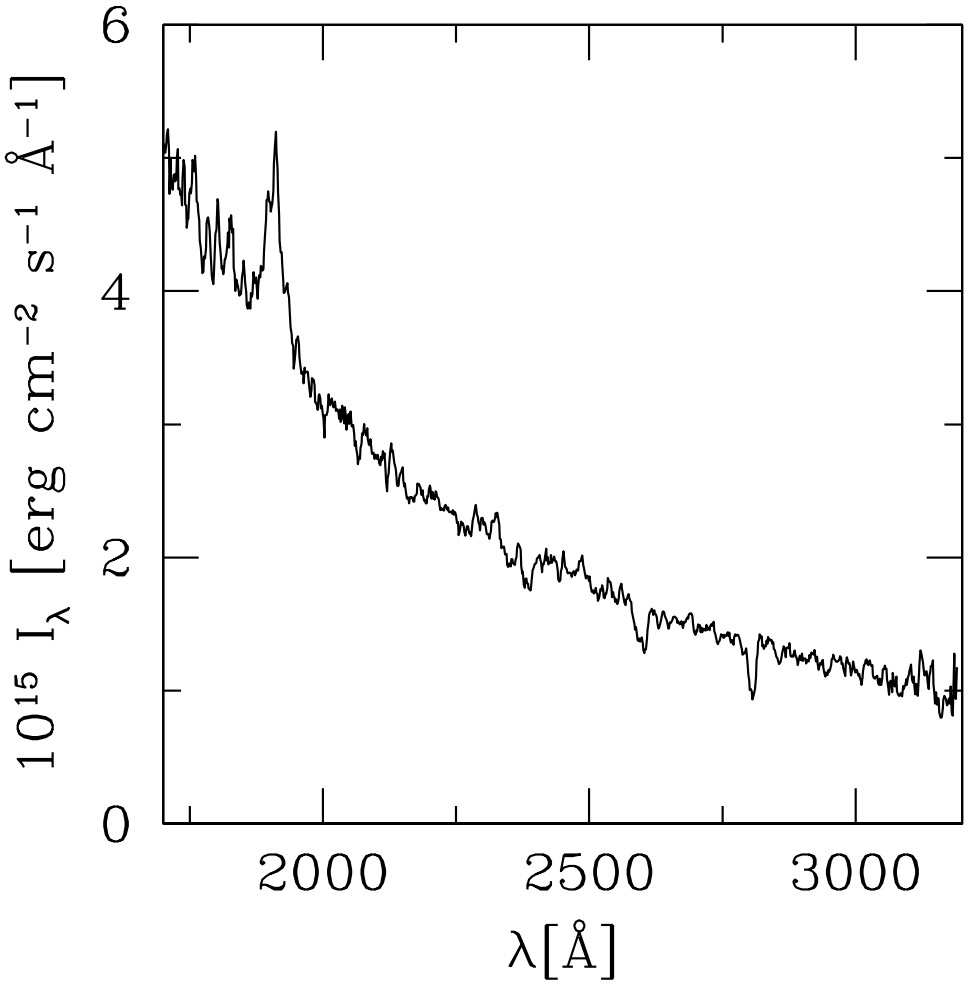
6
4
2
0
2000
2500
3000
10^{15} I_λ [erg cm^{-2} s^{-1} Å^{-1}]
λ[Å]

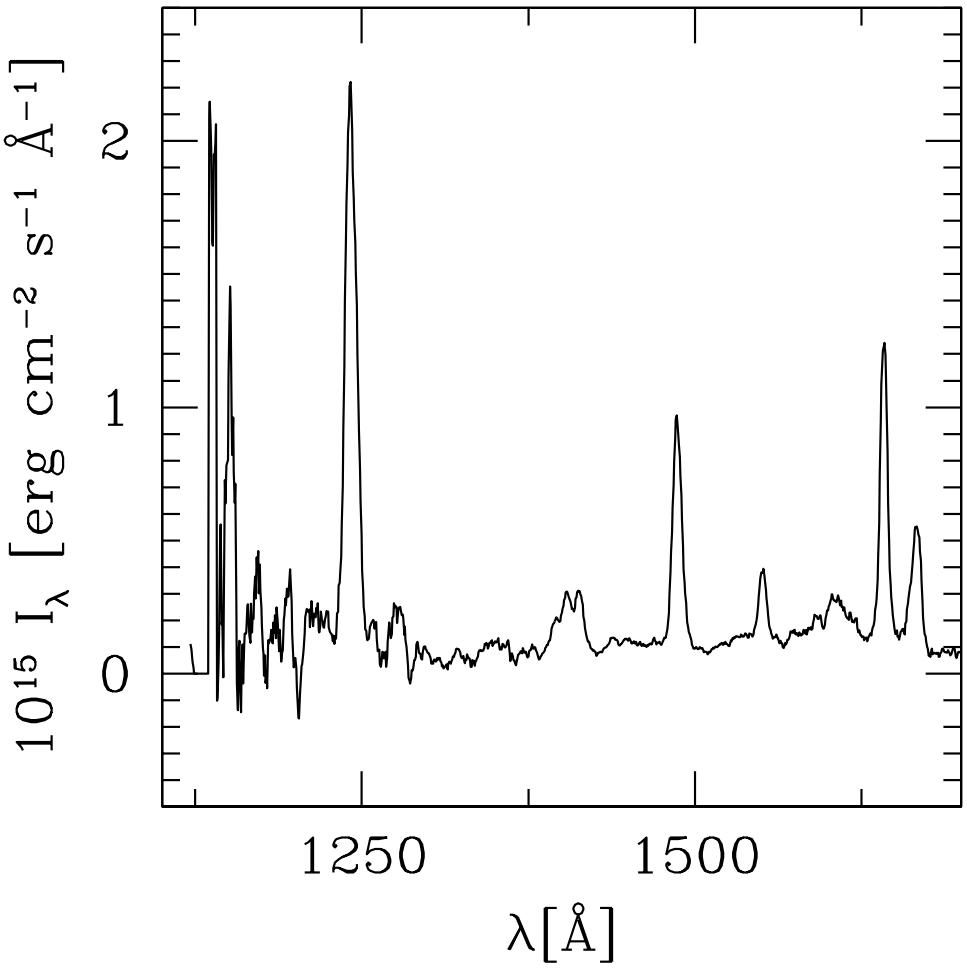
10^{15} I_λ [erg cm^{-2} s^{-1} Å^{-1}]
0
1
2
1250
1500
λ[Å]

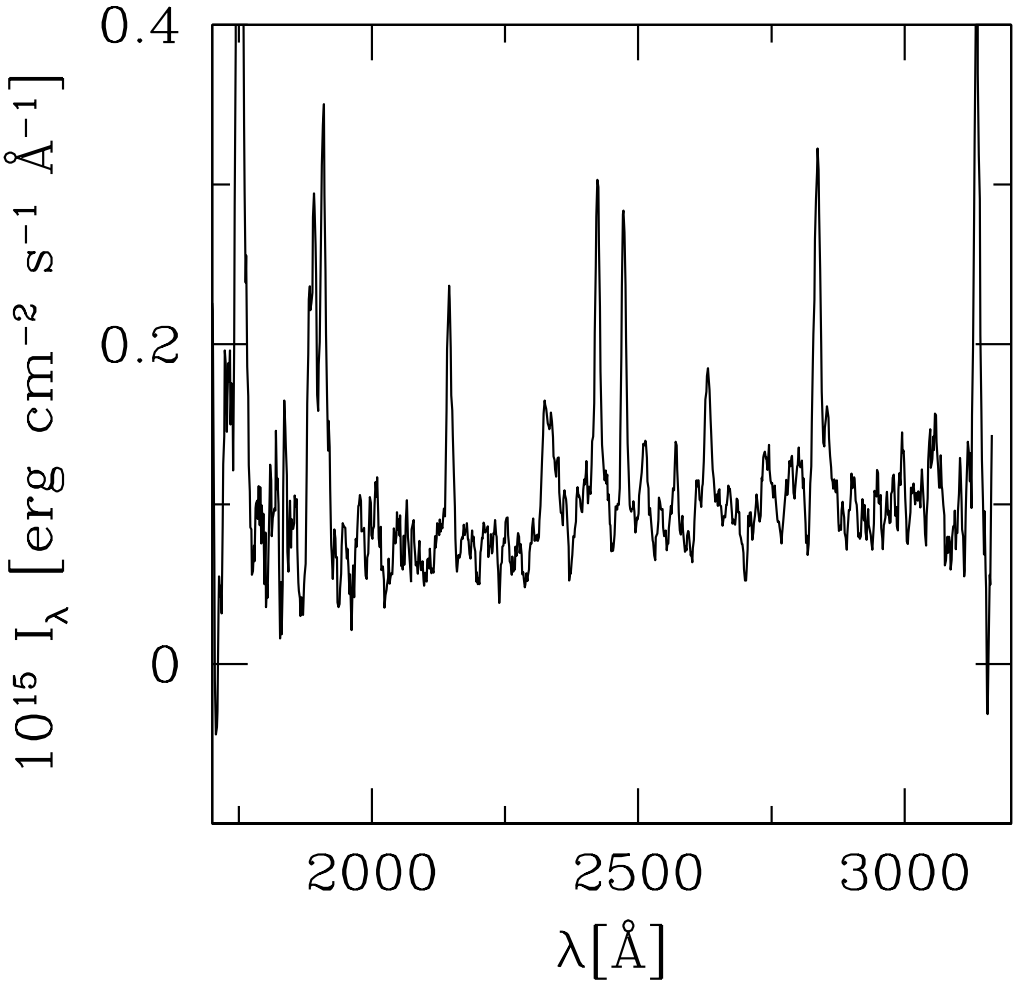
0.4
0.2
0
10^{15} I_λ [erg cm^{-2} s^{-1} Å^{-1}]
2000
2500
3000
λ[Å]

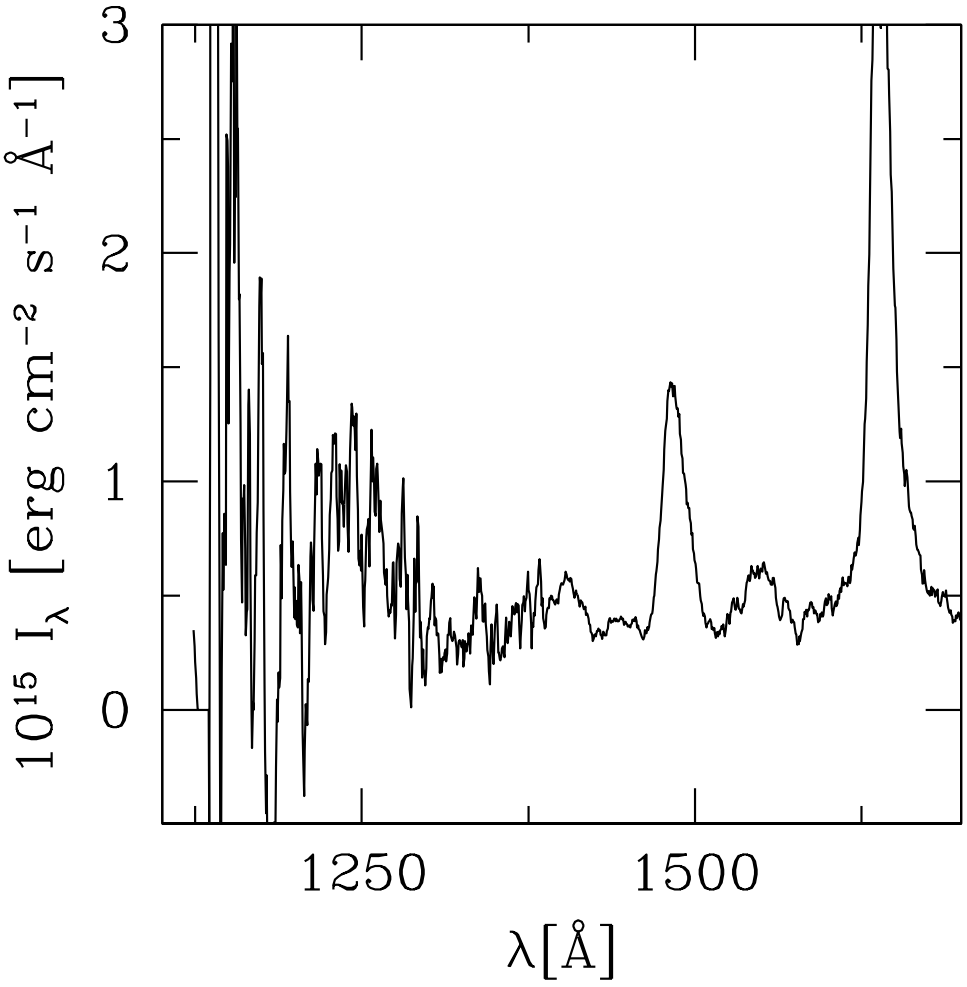
3
2
1
0
10^{15} I_λ [erg cm^{-2} s^{-1} Å^{-1}]
1250
1500
λ[Å]

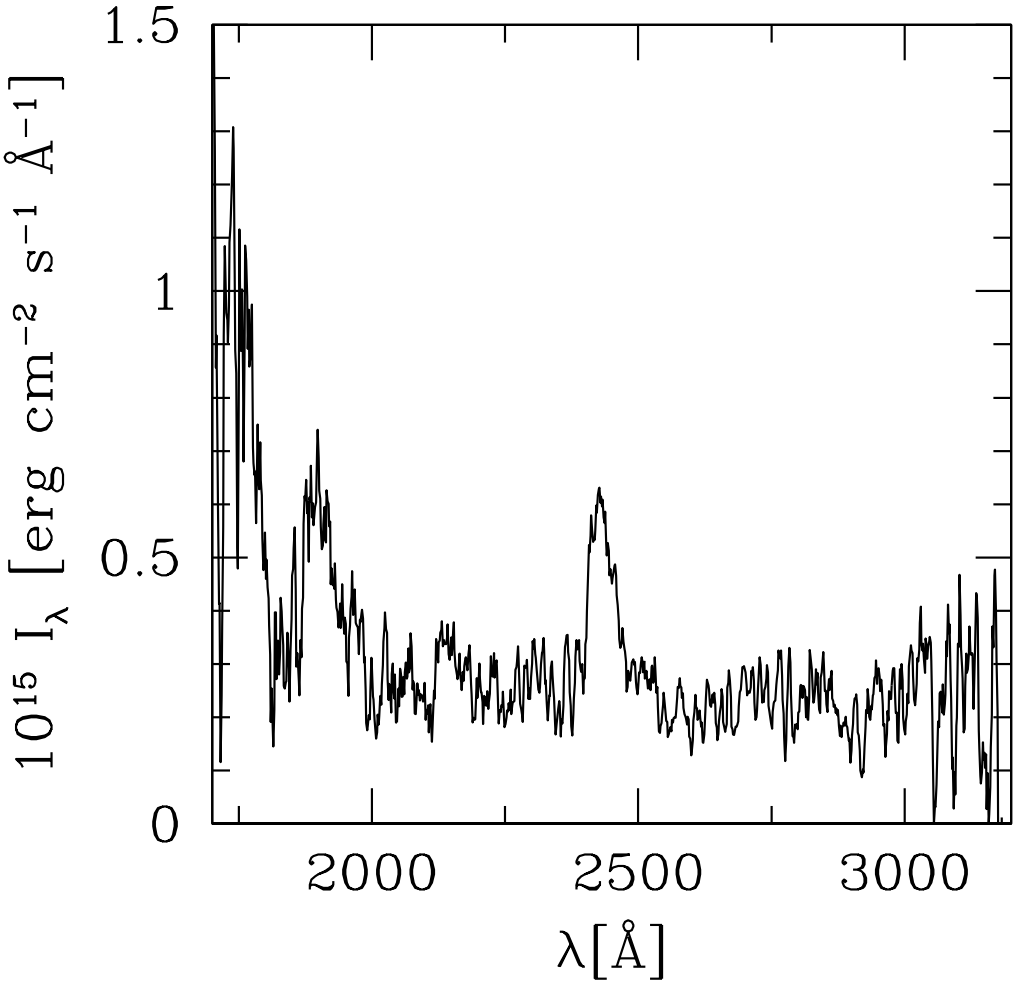
1.5
1
0.5
0
2000
2500
3000
λ[Å]
10¹⁵ I_λ [erg cm⁻² s⁻¹ Å⁻¹]

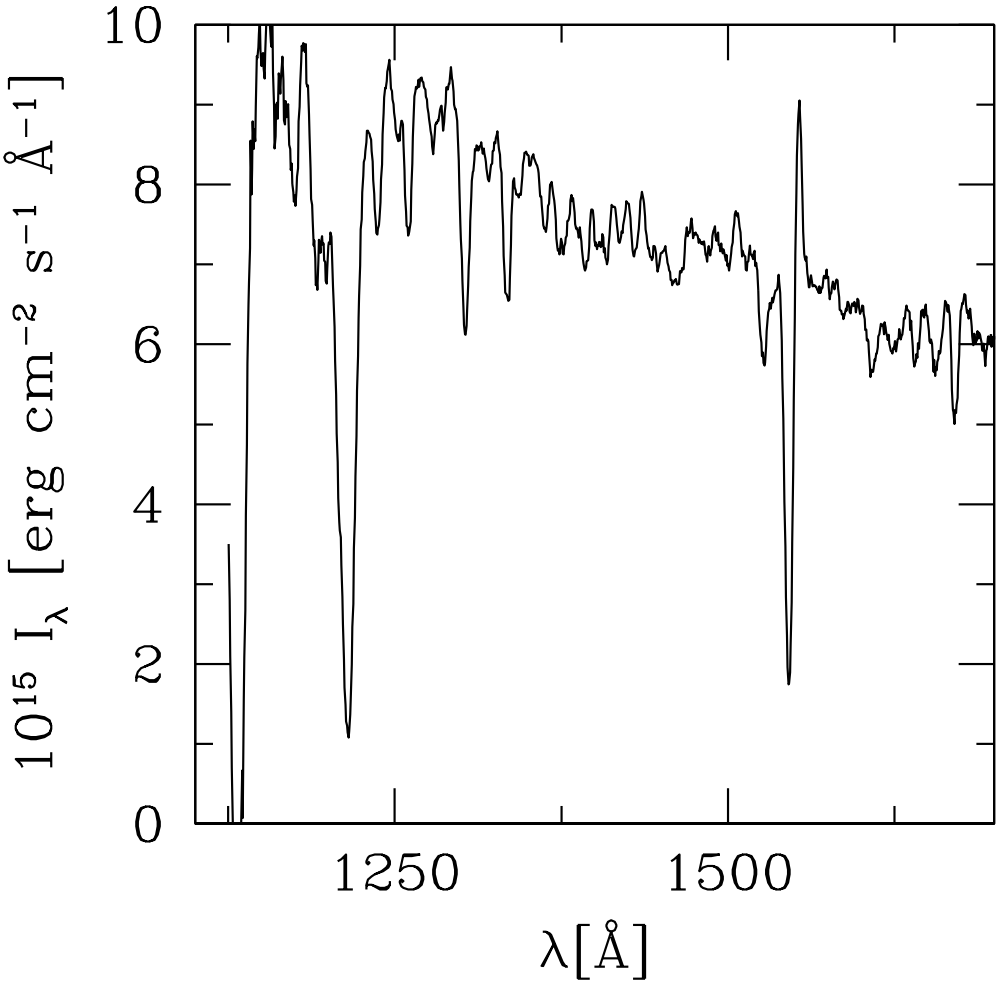
10
8
6
4
2
0
1250
1500
λ[Å]
10^{15} I_λ [erg cm^{-2} s^{-1} Å^{-1}]

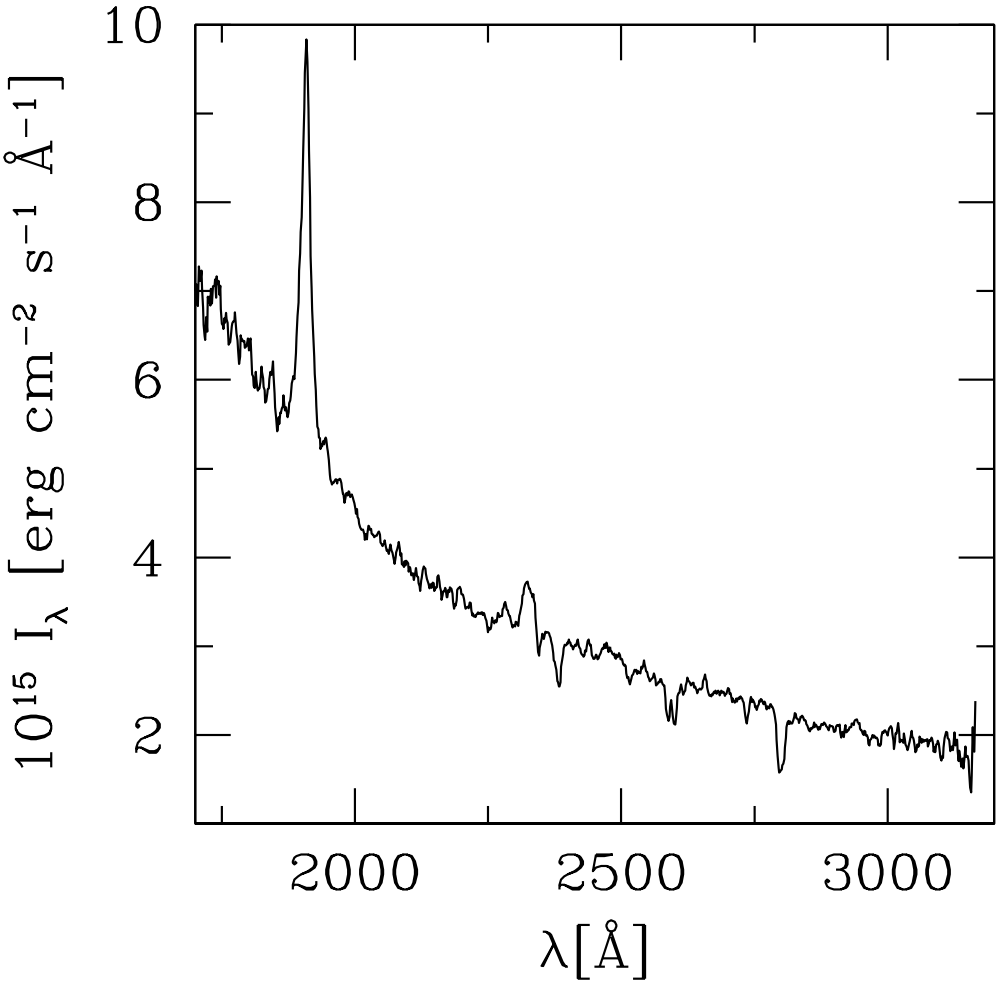
10
8
6
4
2
10^{15} I_λ [erg cm^{-2} s^{-1} Å^{-1}]
2000
2500
3000
λ[Å]

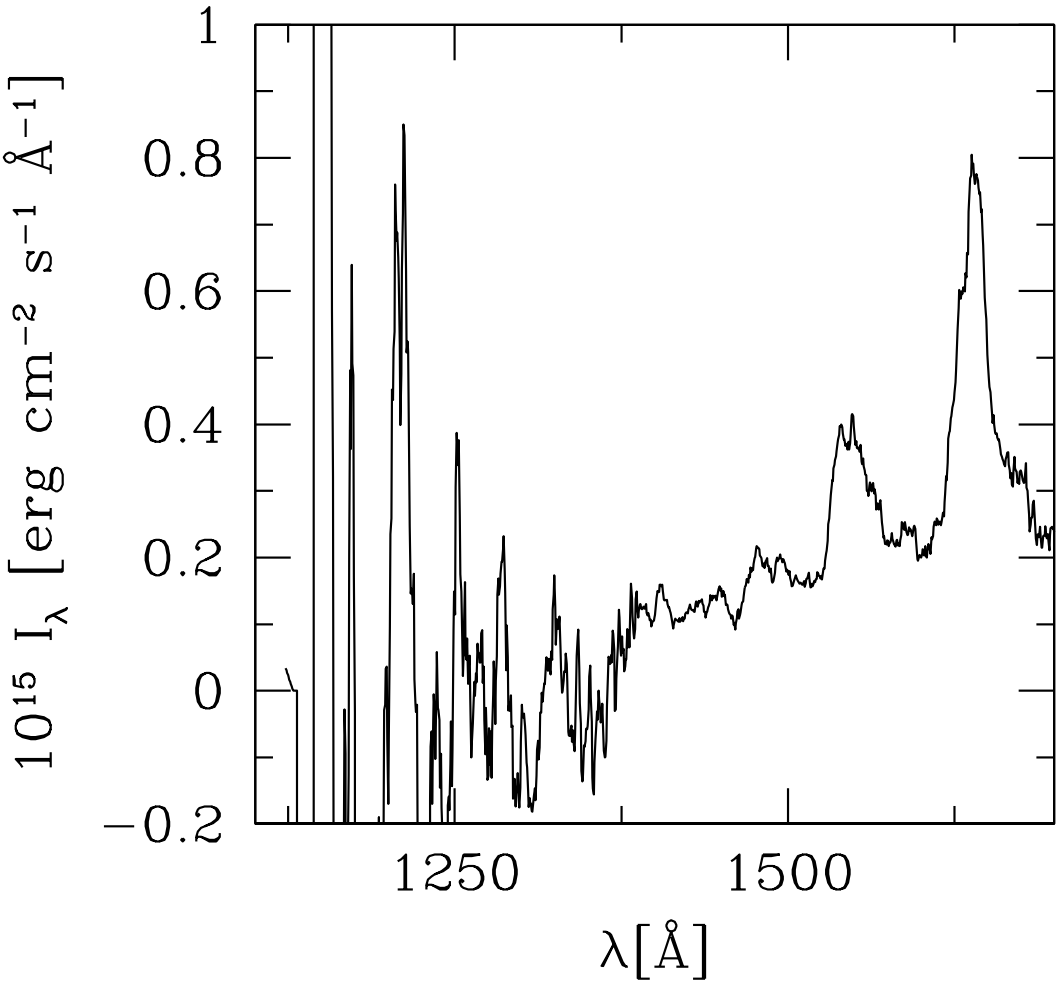
1
0.8
0.6
0.4
0.2
0
−0.2
1250
1500
λ[Å]
10^{15} I_λ [erg cm^{-2} s^{-1} Å^{-1}]

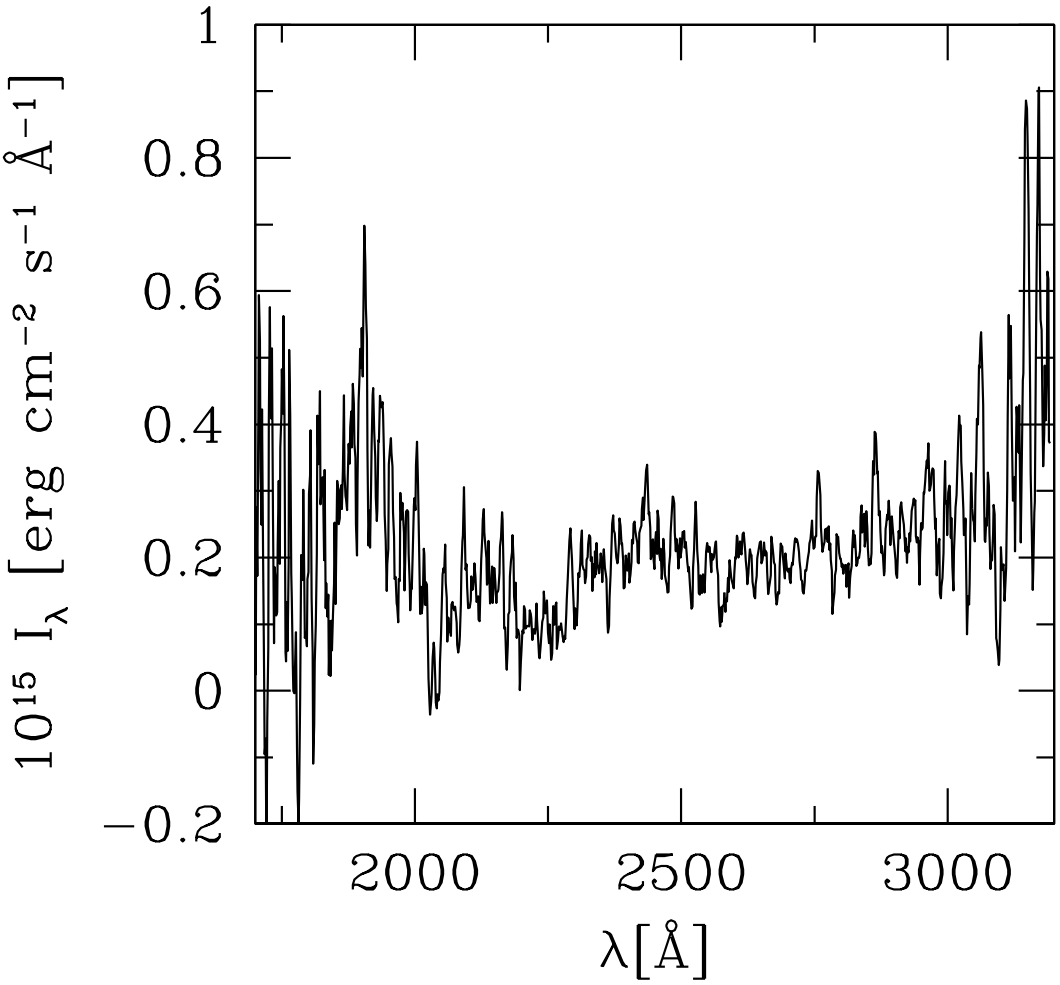
1
0.8
0.6
0.4
0.2
0
−0.2
2000
2500
3000
λ[Å]
10¹⁵ I_λ [erg cm⁻² s⁻¹ Å⁻¹]

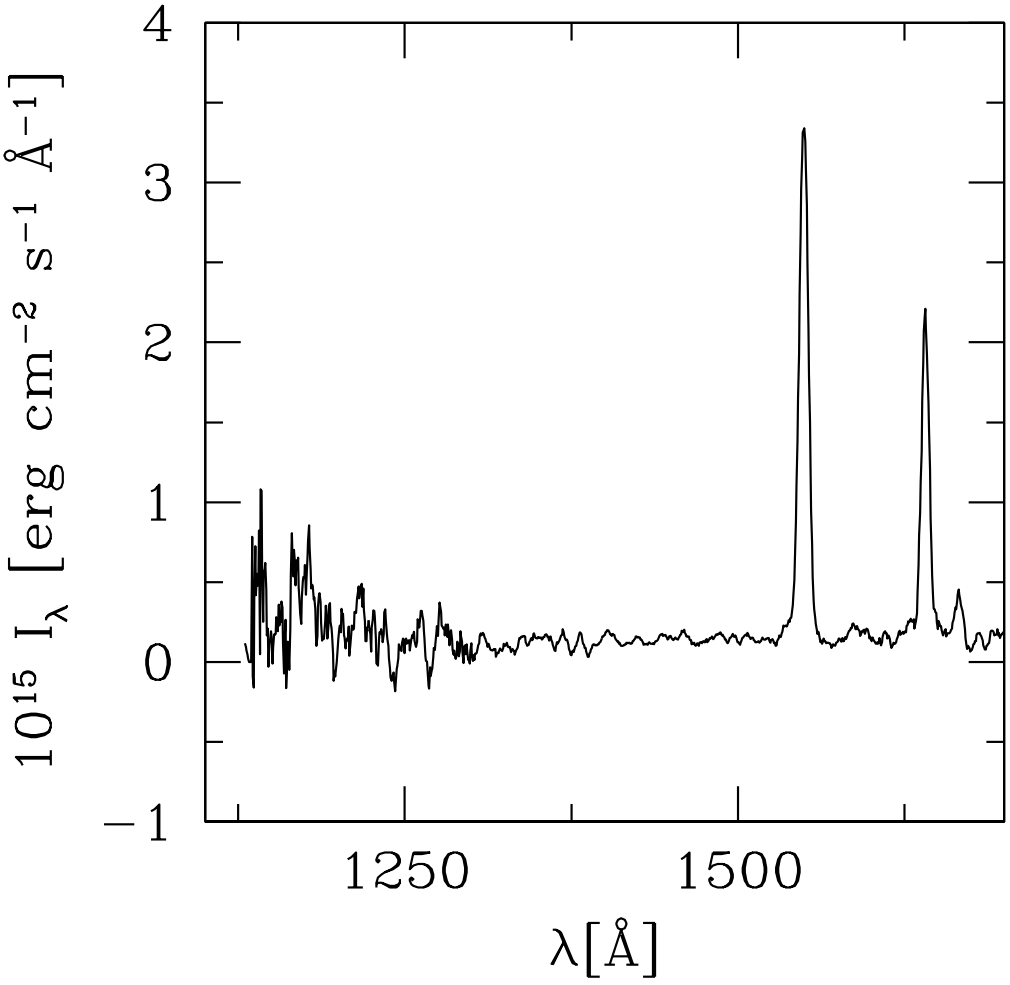
4
3
2
1
0
−1
1250
1500
λ[Å]
10^{15} I_λ [erg cm^{-2} s^{-1} Å^{-1}]

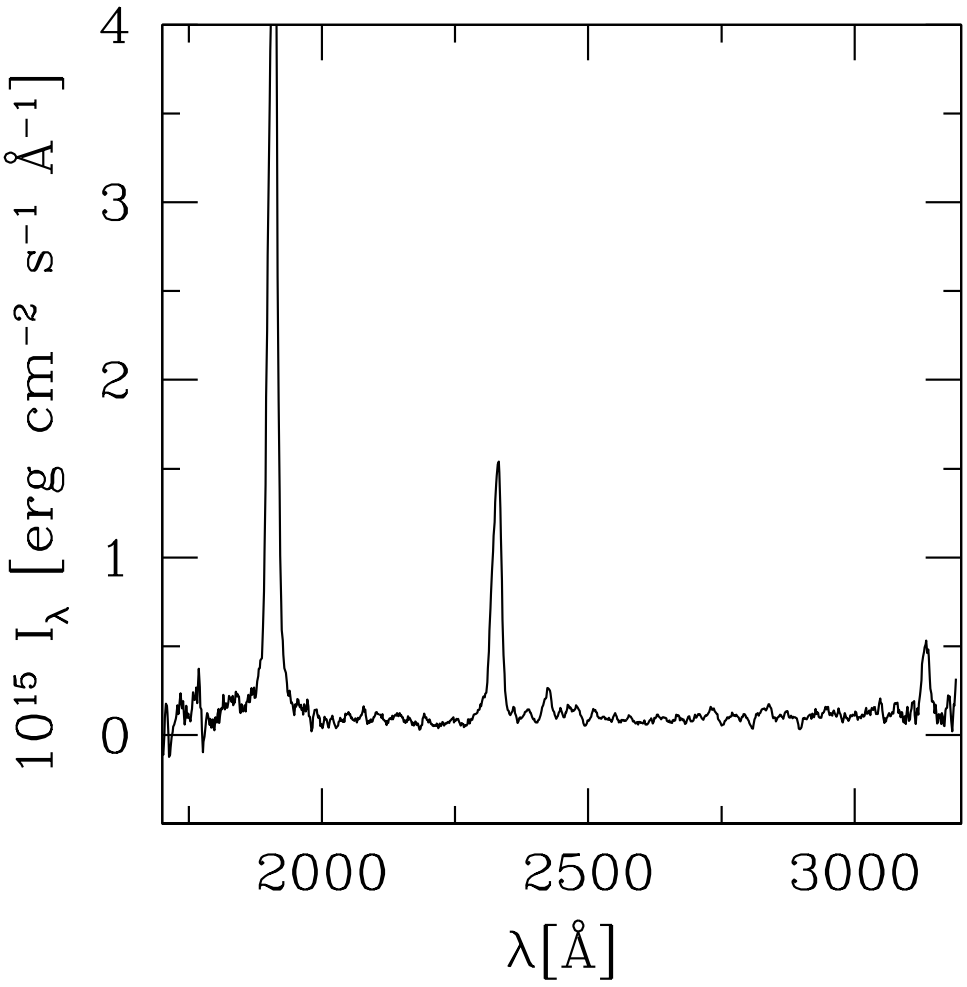
4
3
2
1
0
10^{15} I_λ [erg cm^{-2} s^{-1} Å^{-1}]
2000
2500
3000
λ[Å]

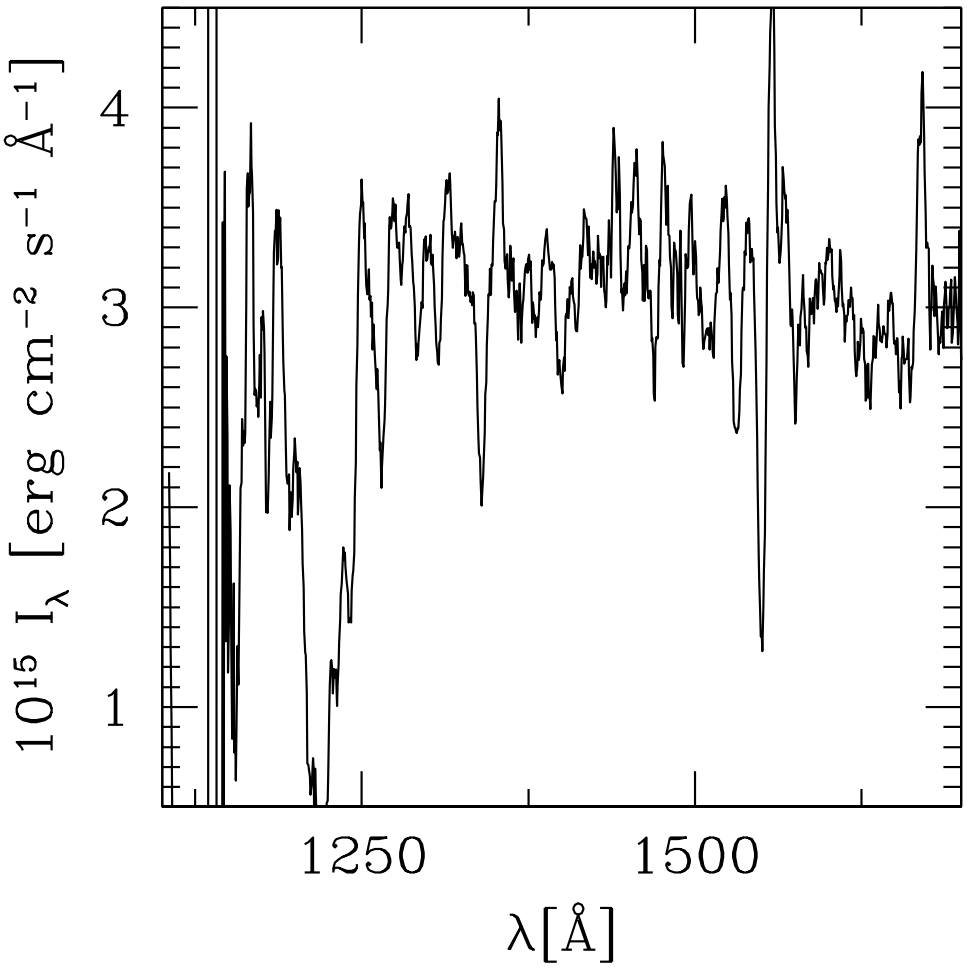
10^{15} I_λ [erg cm^{-2} s^{-1} Å^{-1}]
1
2
3
4
1250
1500
λ[Å]

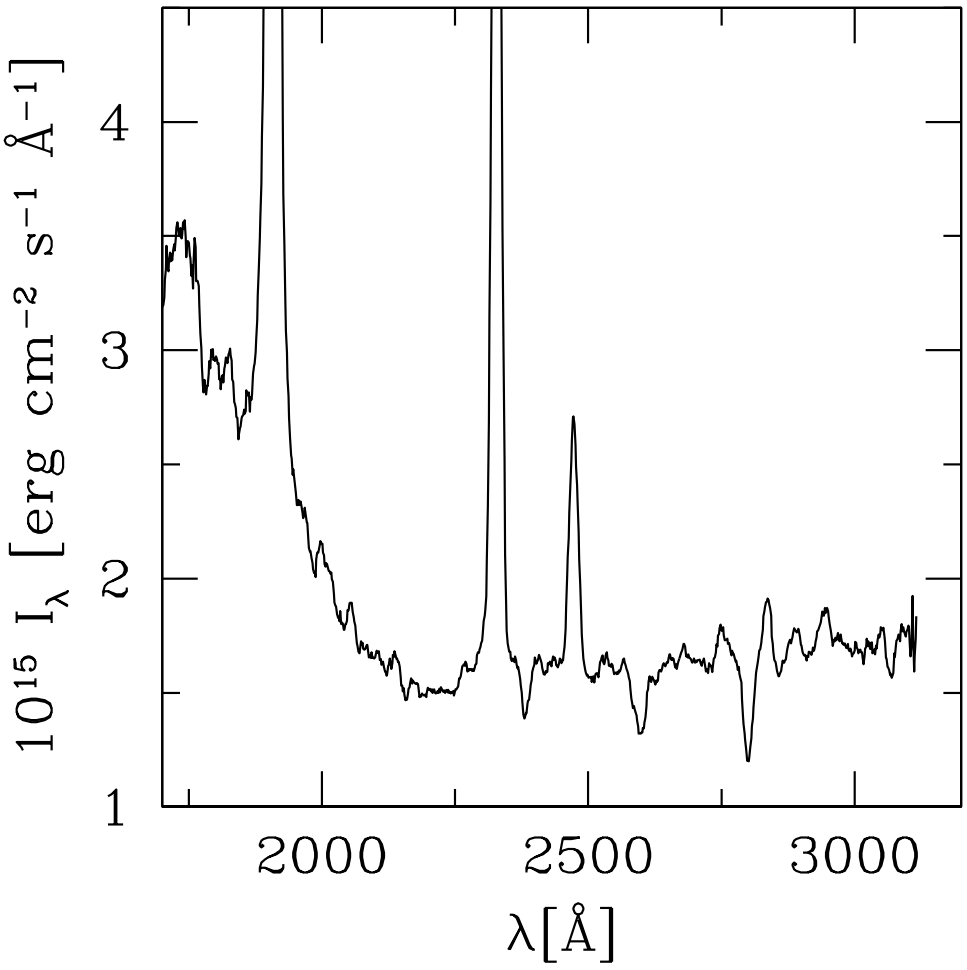
10^{15} I_λ [erg cm^{-2} s^{-1} Å^{-1}]
1
2
3
4
2000
2500
3000
λ[Å]

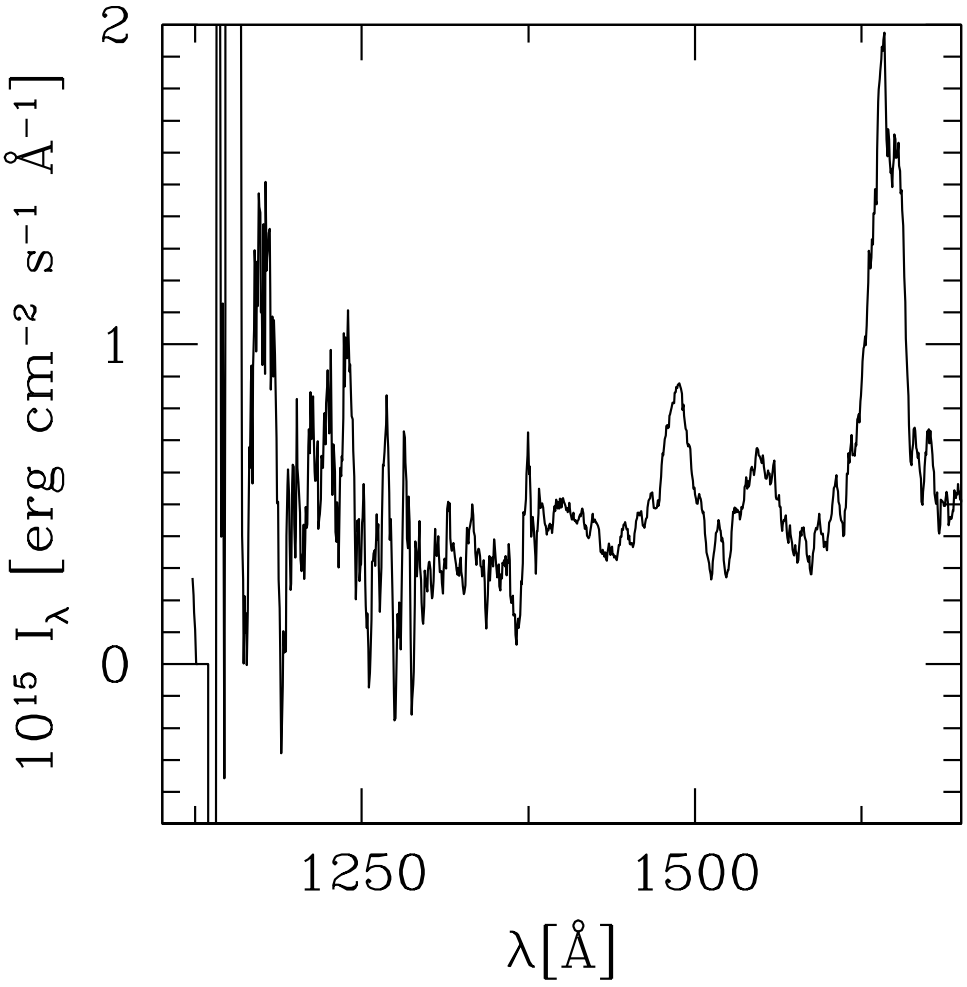
2
1
0
10^{15} I_λ [erg cm^{-2} s^{-1} Å^{-1}]
1250
1500
λ[Å]

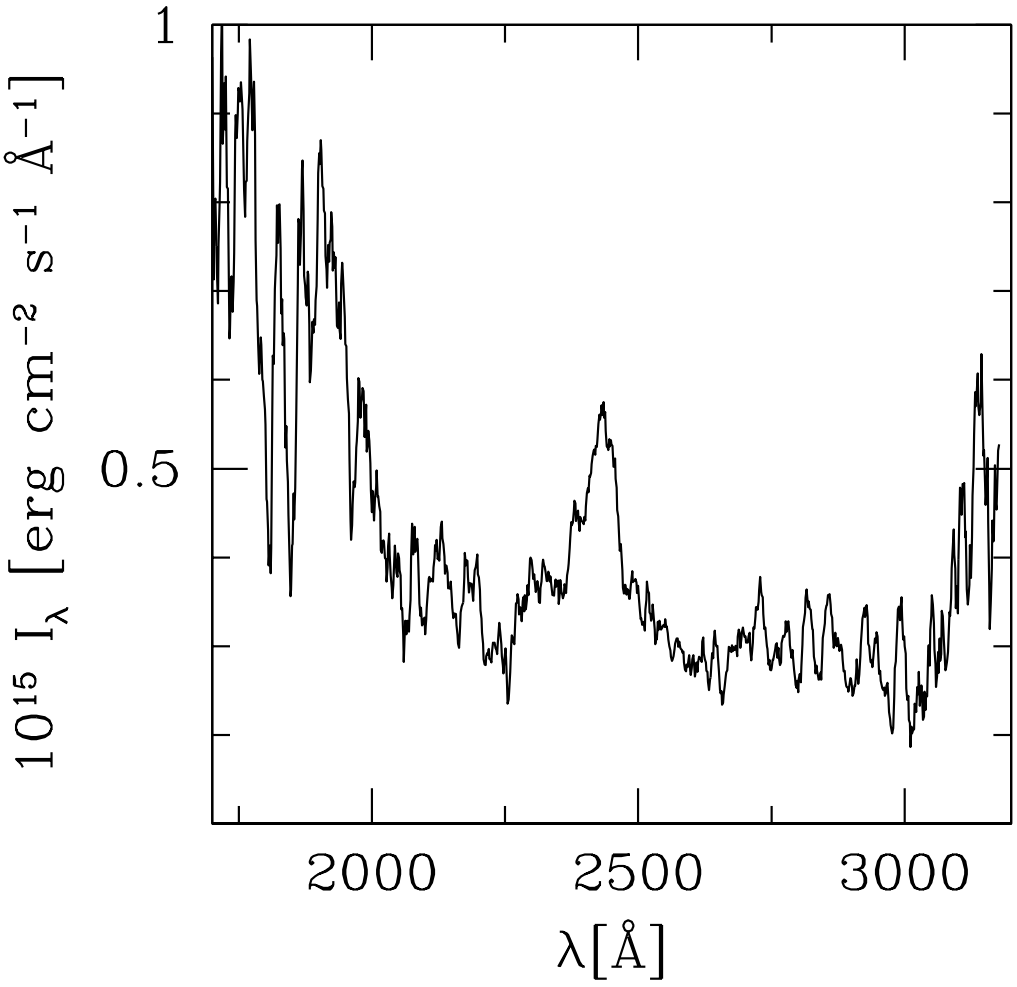
1
0.5
10^{15} I_λ [erg cm^{-2} s^{-1} Å^{-1}]
2000
2500
3000
λ[Å]

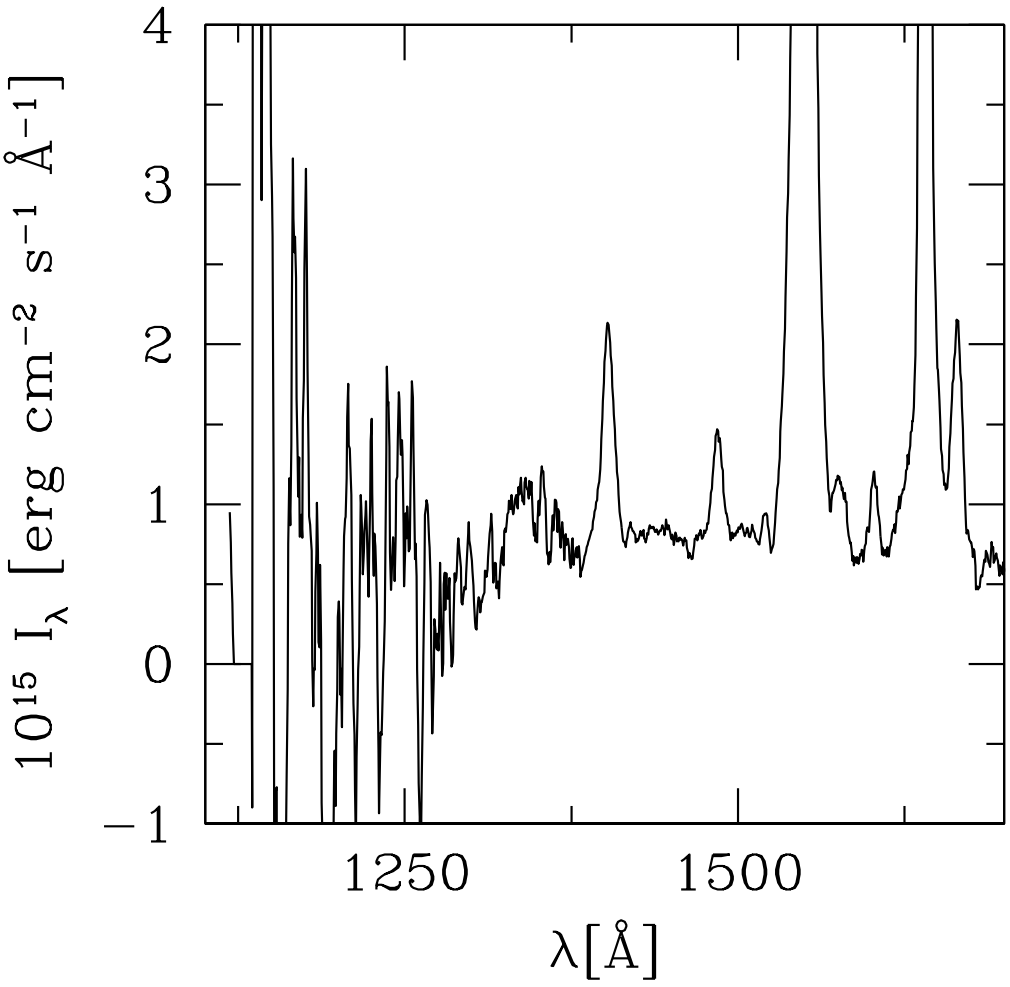
4
3
2
1
0
−1
1250
1500
λ[Å]
10^{15} I_λ [erg cm^{-2} s^{-1} Å^{-1}]

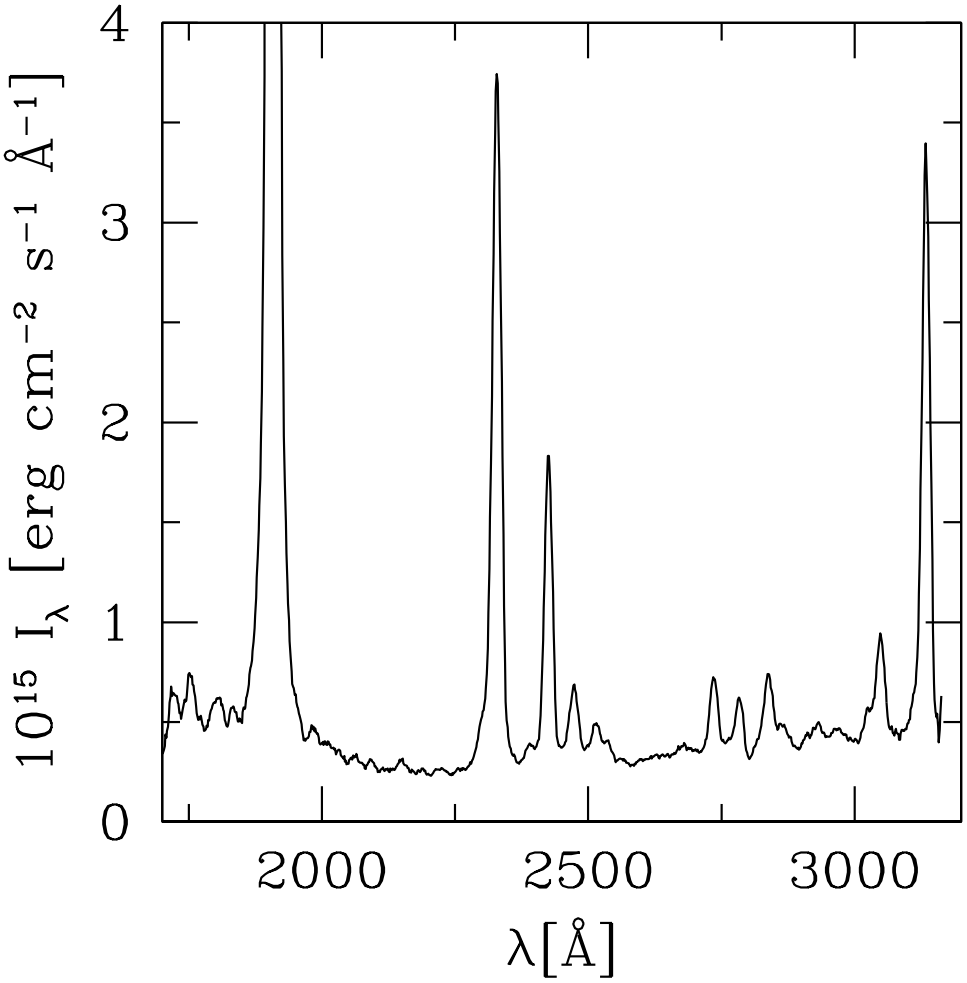
4
3
2
1
0
2000
2500
3000
λ[Å]
10¹⁵ I_λ [erg cm⁻² s⁻¹ Å⁻¹]

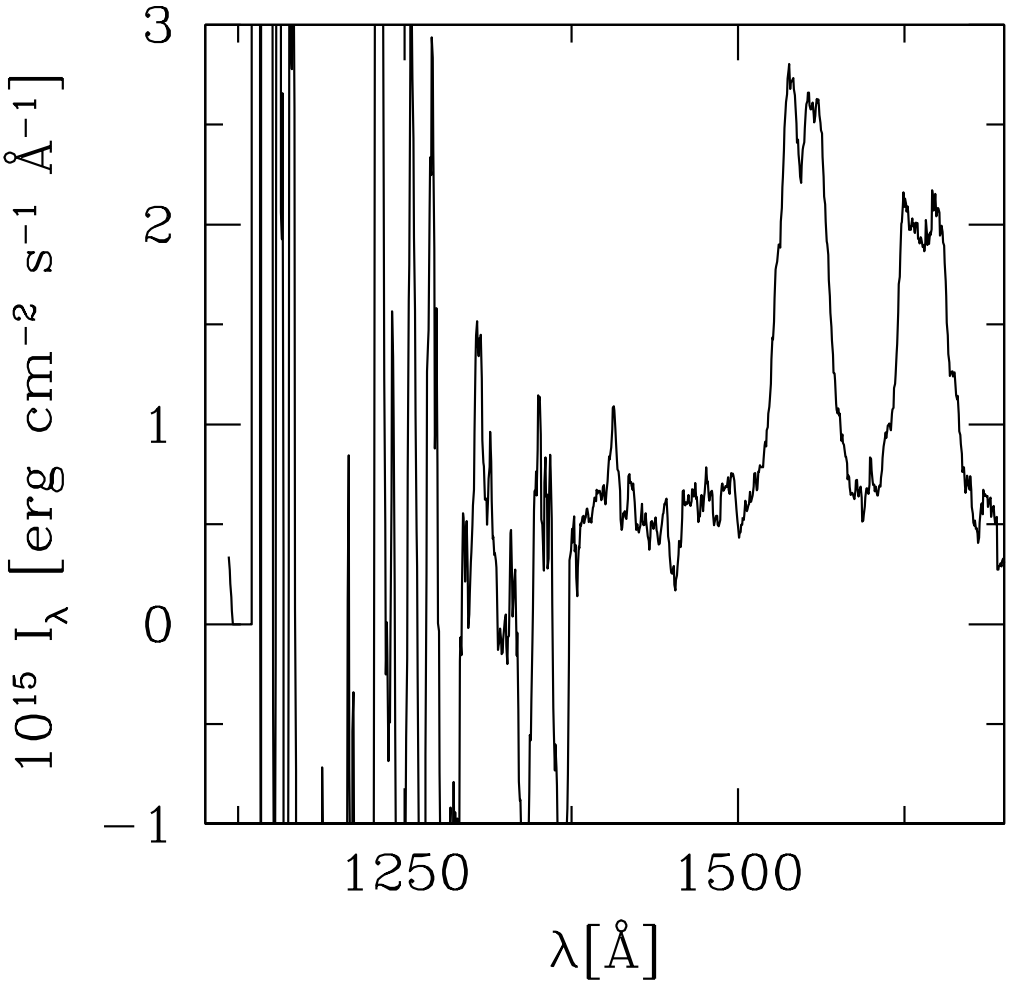
3
2
1
0
−1
1250
1500
λ[Å]
10^{15} I_λ [erg cm^{-2} s^{-1} Å^{-1}]

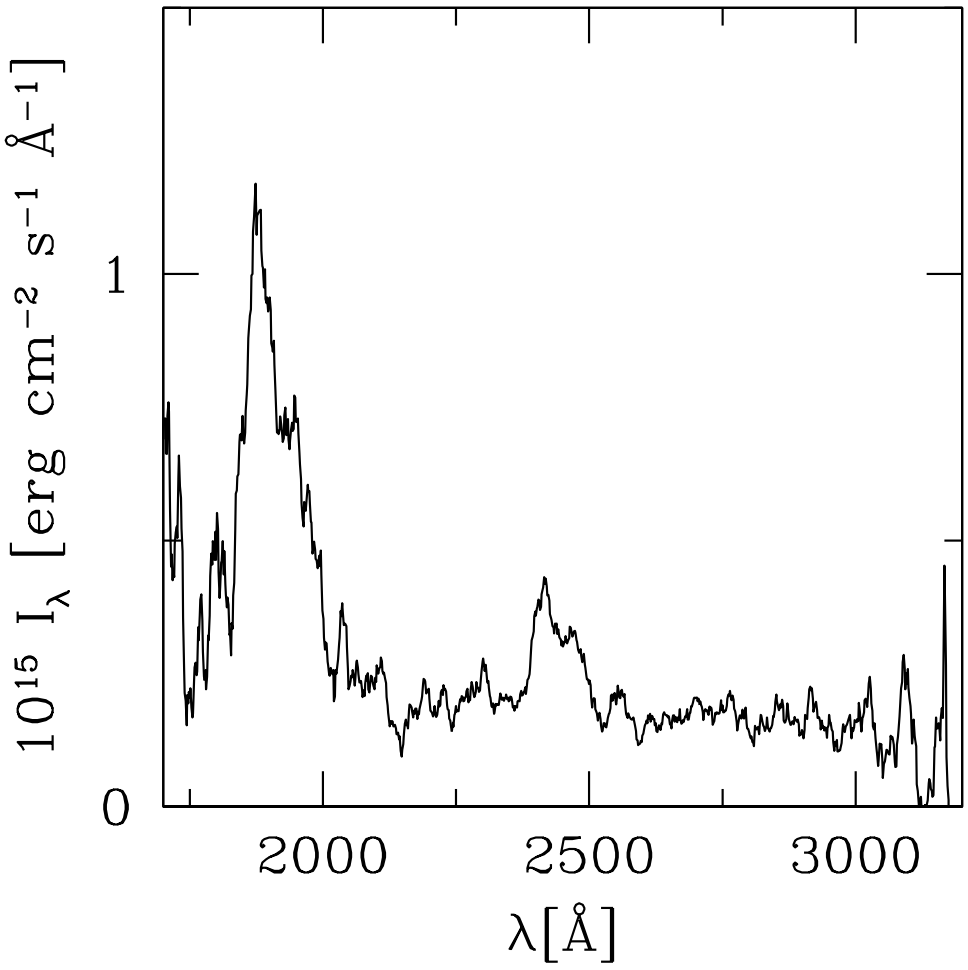
10^{15} I_λ [erg cm^{-2} s^{-1} Å^{-1}]
1
0
2000
2500
3000
λ[Å]

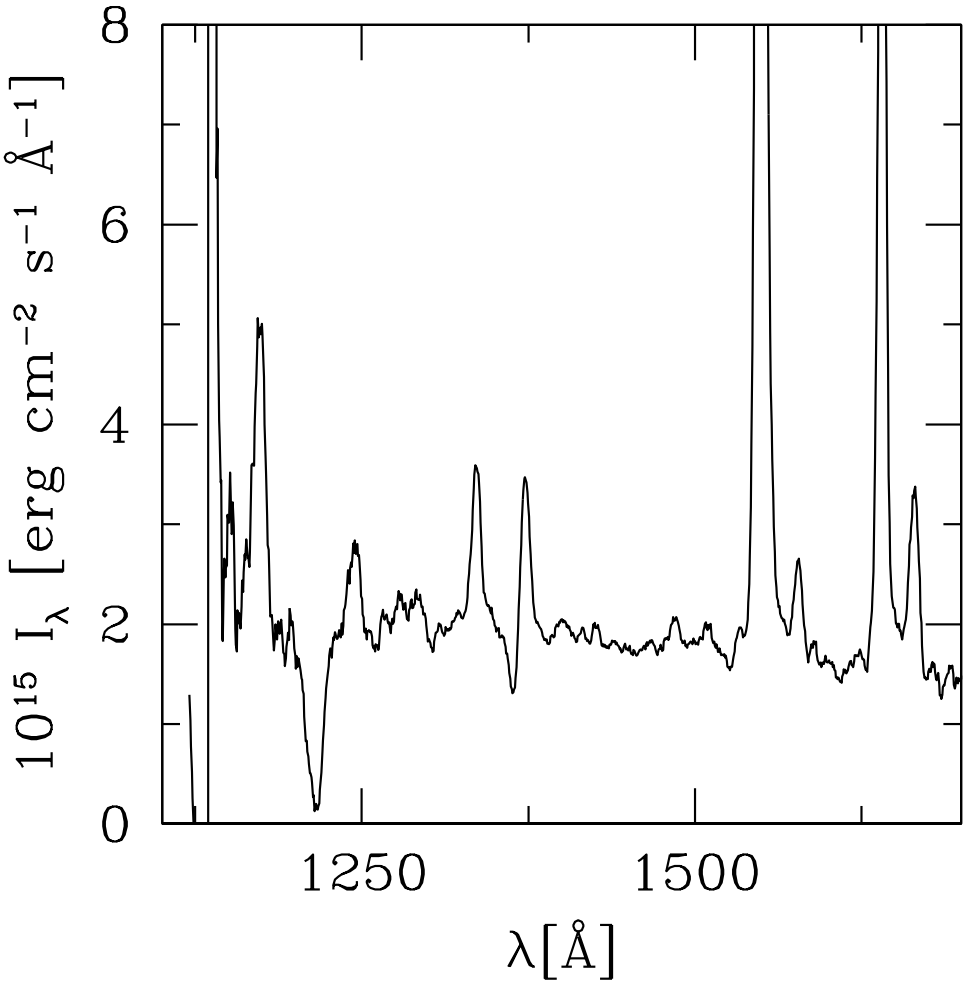
8
6
4
2
0
1250
1500
λ[Å]
10^{15} I_λ [erg cm^{-2} s^{-1} Å^{-1}]

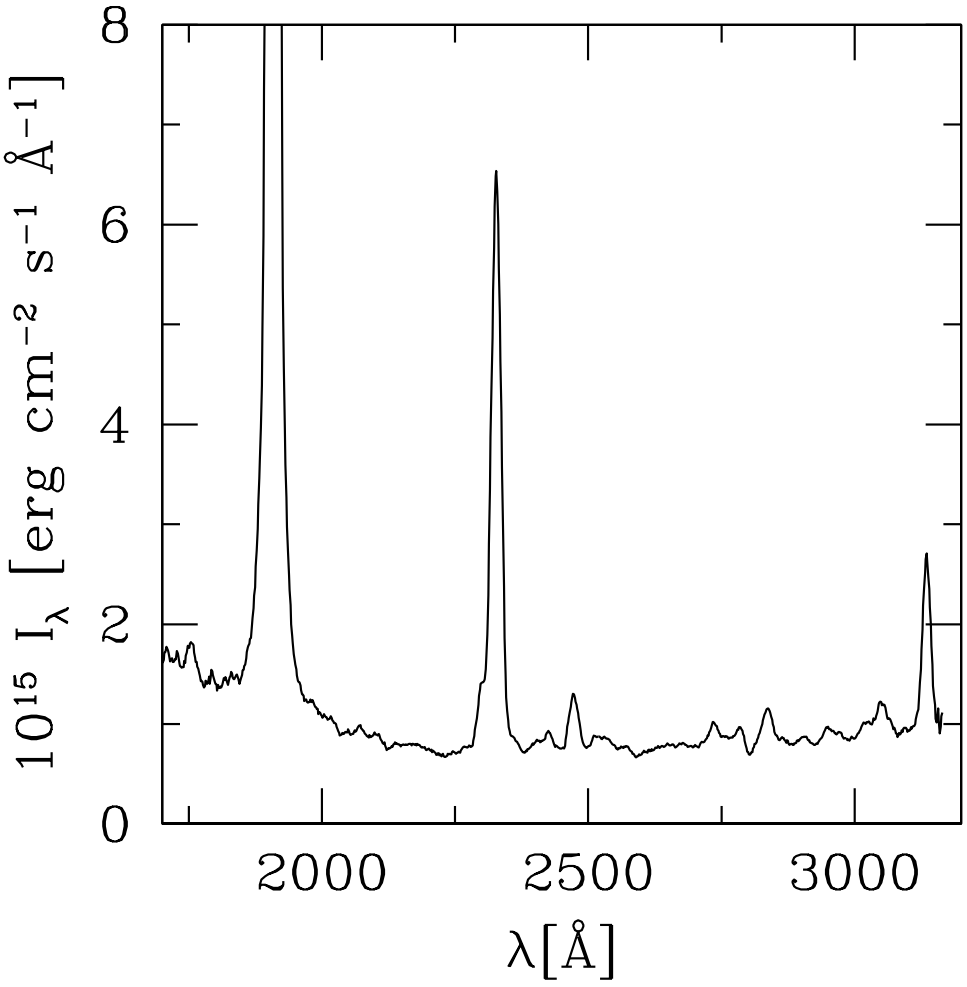
8
6
4
2
0
2000
2500
3000
λ[Å]
10^{15} I_λ [erg cm^{-2} s^{-1} Å^{-1}]

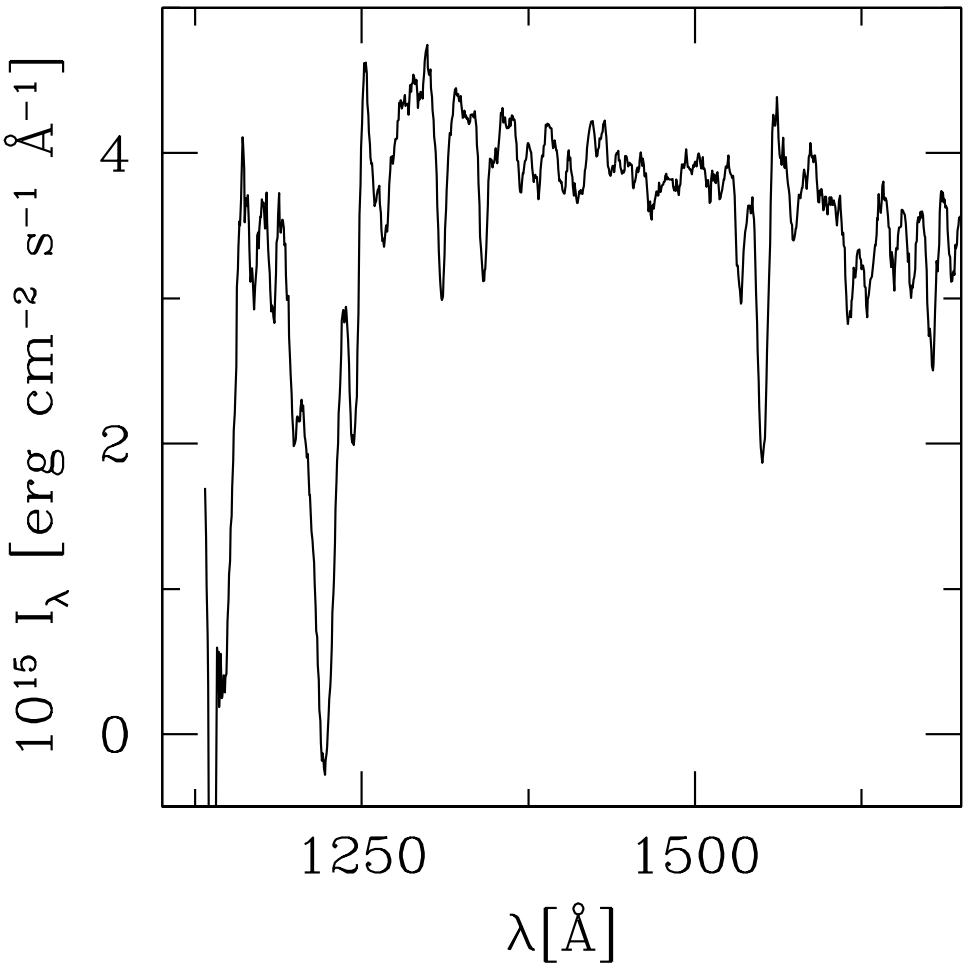
10^{15} I_λ [erg cm^{-2} s^{-1} Å^{-1}]
0
2
4
1250
1500
λ[Å]

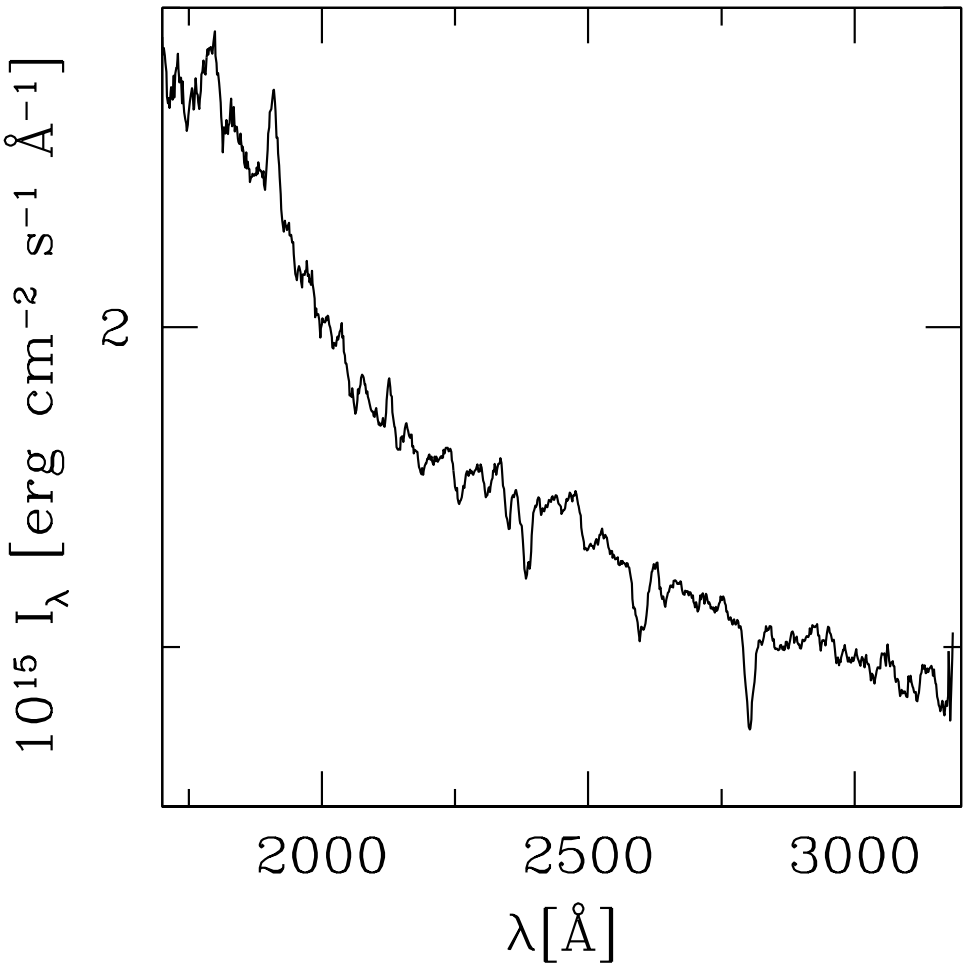
10^{15} I_λ [erg cm^{-2} s^{-1} Å^{-1}]
2000
2500
3000
λ[Å]

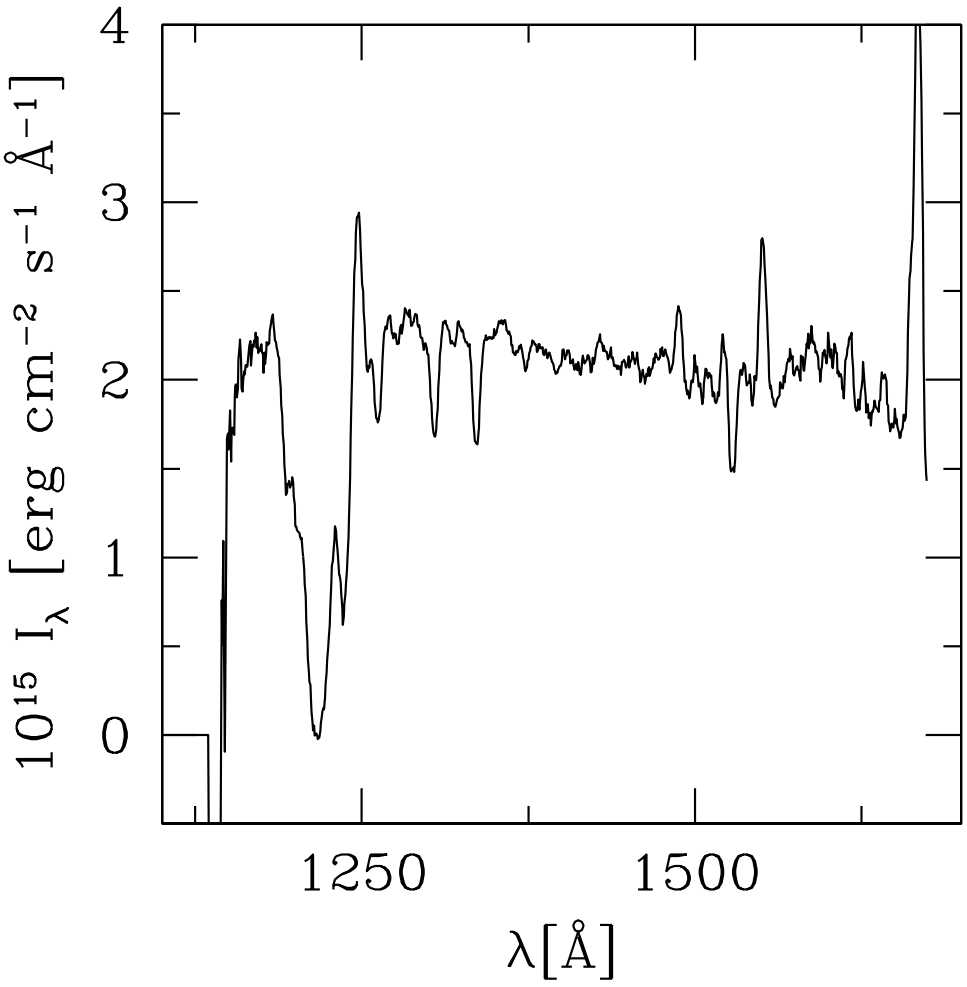
4
3
2
1
0
10^{15} I_λ [erg cm^{-2} s^{-1} Å^{-1}]
1250
1500
λ[Å]

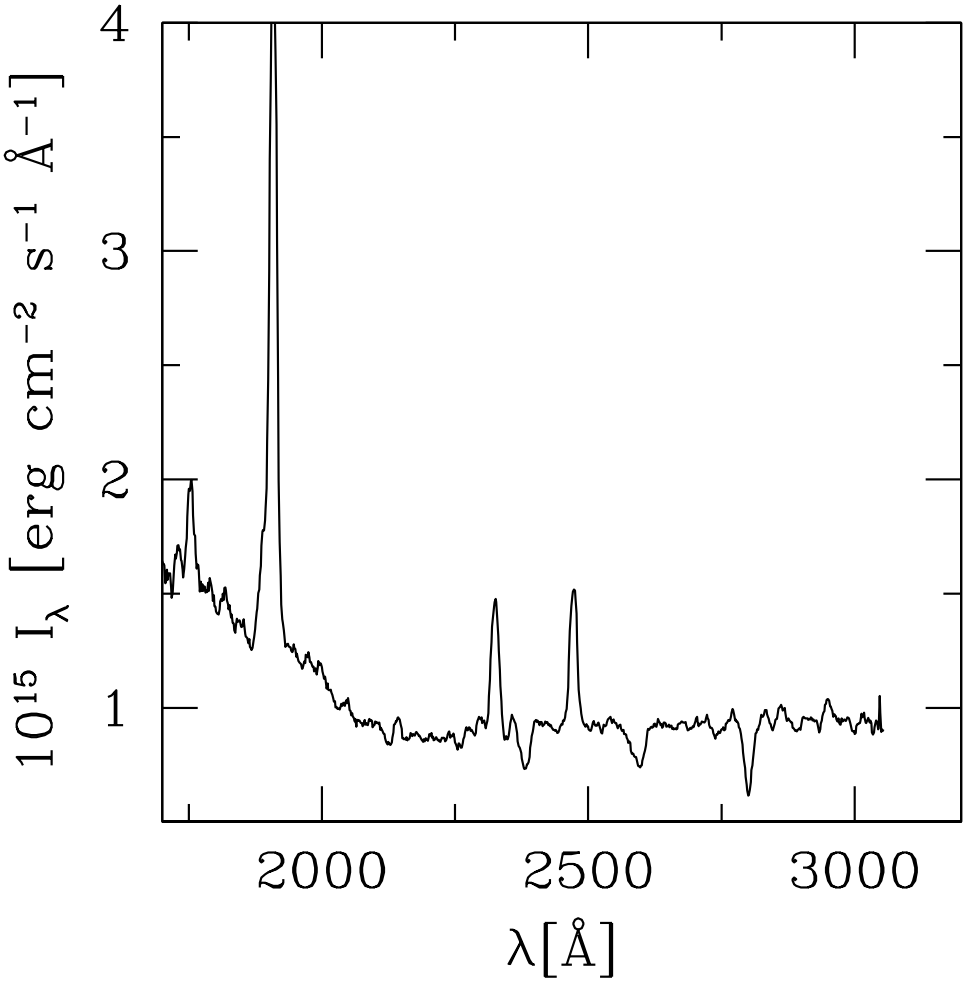
4
3
2
1
10^{15} I_λ [erg cm^{-2} s^{-1} Å^{-1}]
2000
2500
3000
λ[Å]

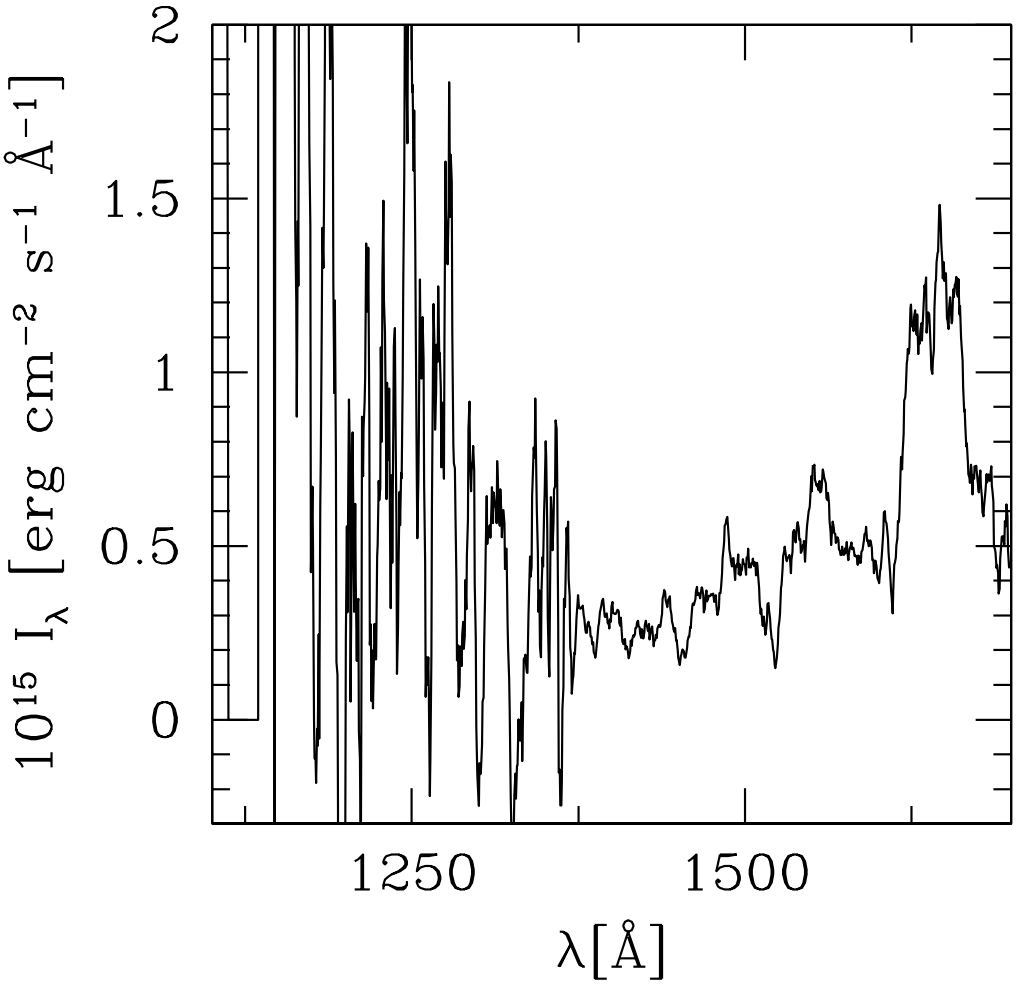
2
1.5
1
0.5
0
10^{15} I_λ [erg cm^{-2} s^{-1} Å^{-1}]
1250
1500
λ[Å]

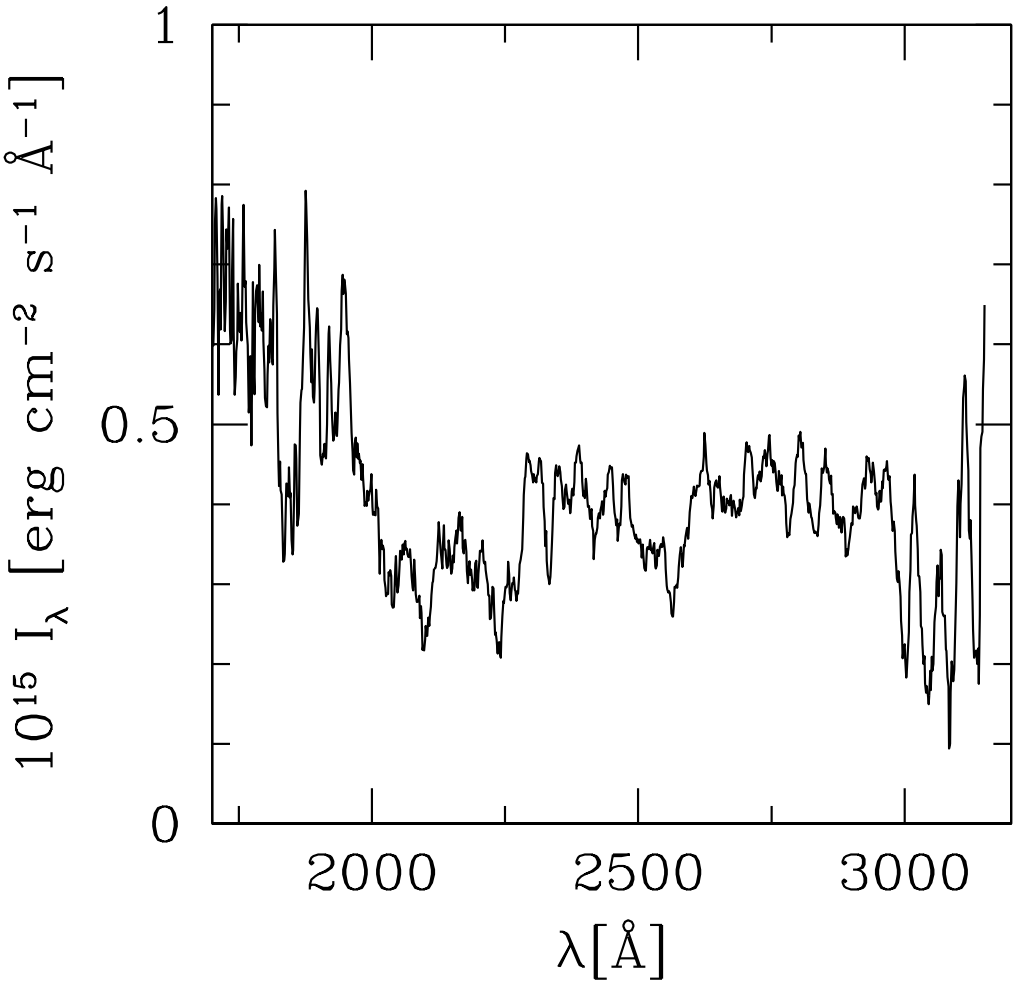
1
0.5
0
2000
2500
3000
λ[Å]
10^{15} I_λ [erg cm^{-2} s^{-1} Å^{-1}]

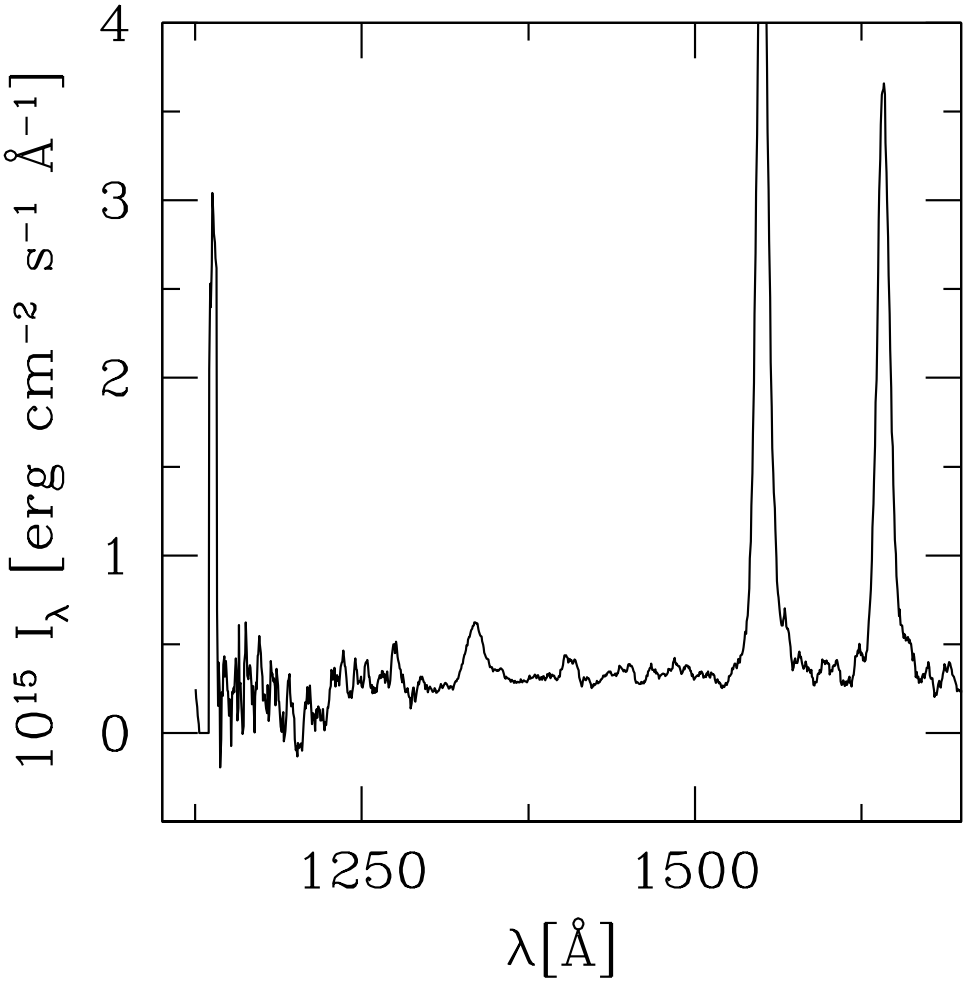
4
3
2
1
0
10^{15} I_λ [erg cm^{-2} s^{-1} Å^{-1}]
1250
1500
λ[Å]

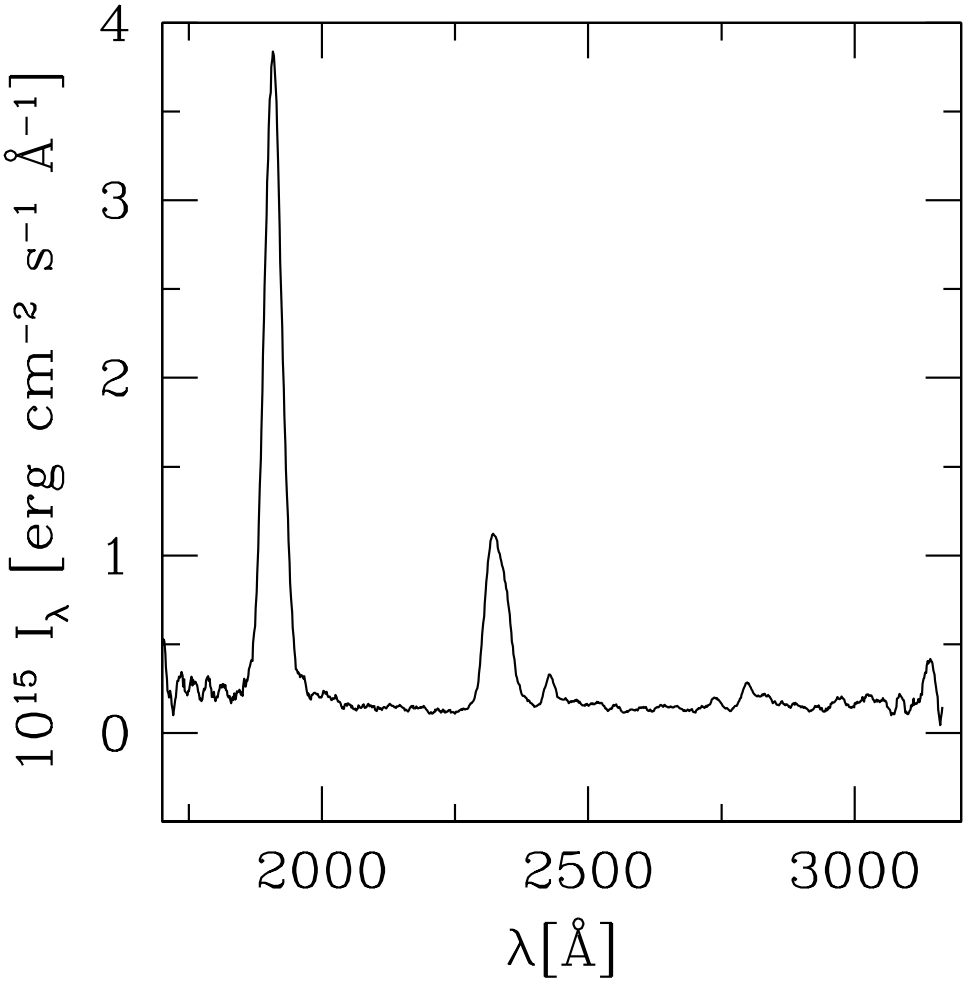
4
3
2
1
0
10^{15} I_λ [erg cm^{-2} s^{-1} Å^{-1}]
2000
2500
3000
λ[Å]

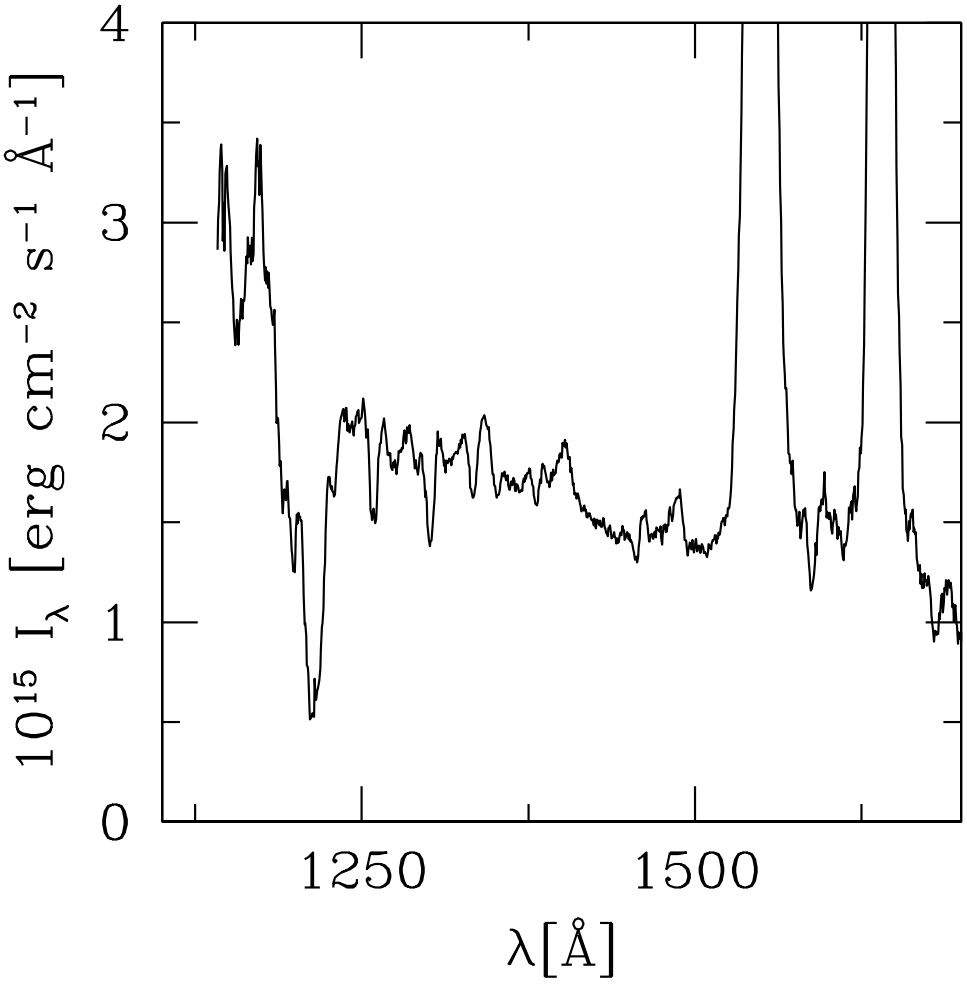
4
3
2
1
0
10^{15} I_λ [erg cm^{-2} s^{-1} Å^{-1}]
1250
1500
λ[Å]

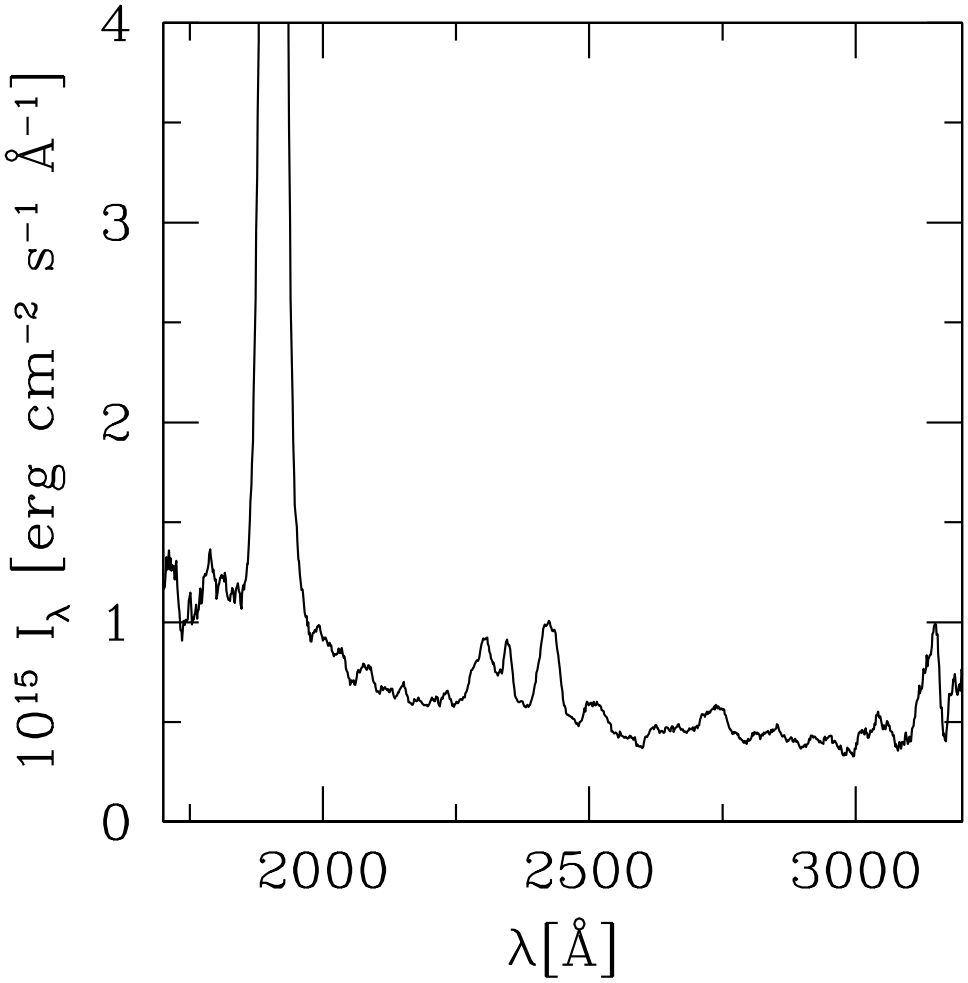
4
3
2
1
0
2000
2500
3000
λ[Å]
10¹⁵ I_λ [erg cm⁻² s⁻¹ Å⁻¹]

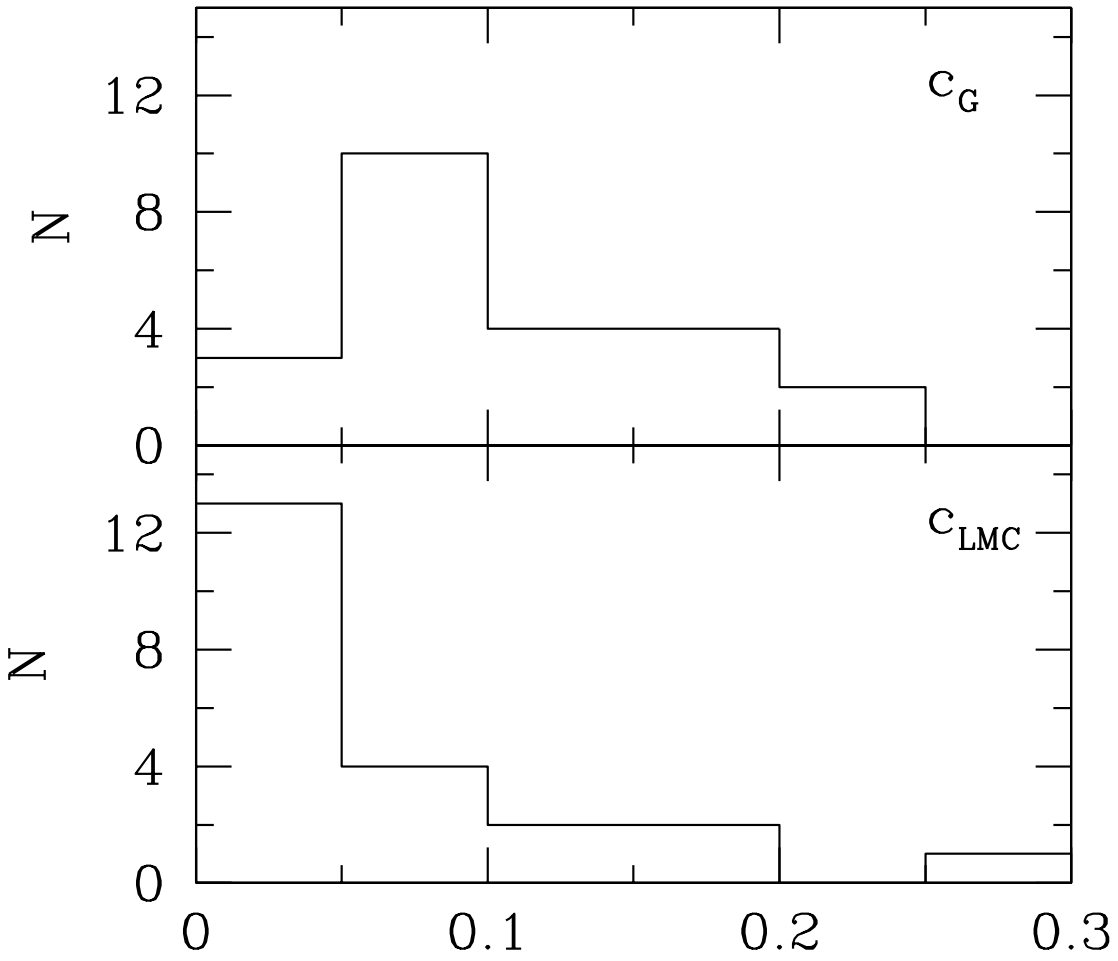
12
8
4
0
N
c_G
12
8
4
0
N
c_{LMC}
0
0.1
0.2
0.3

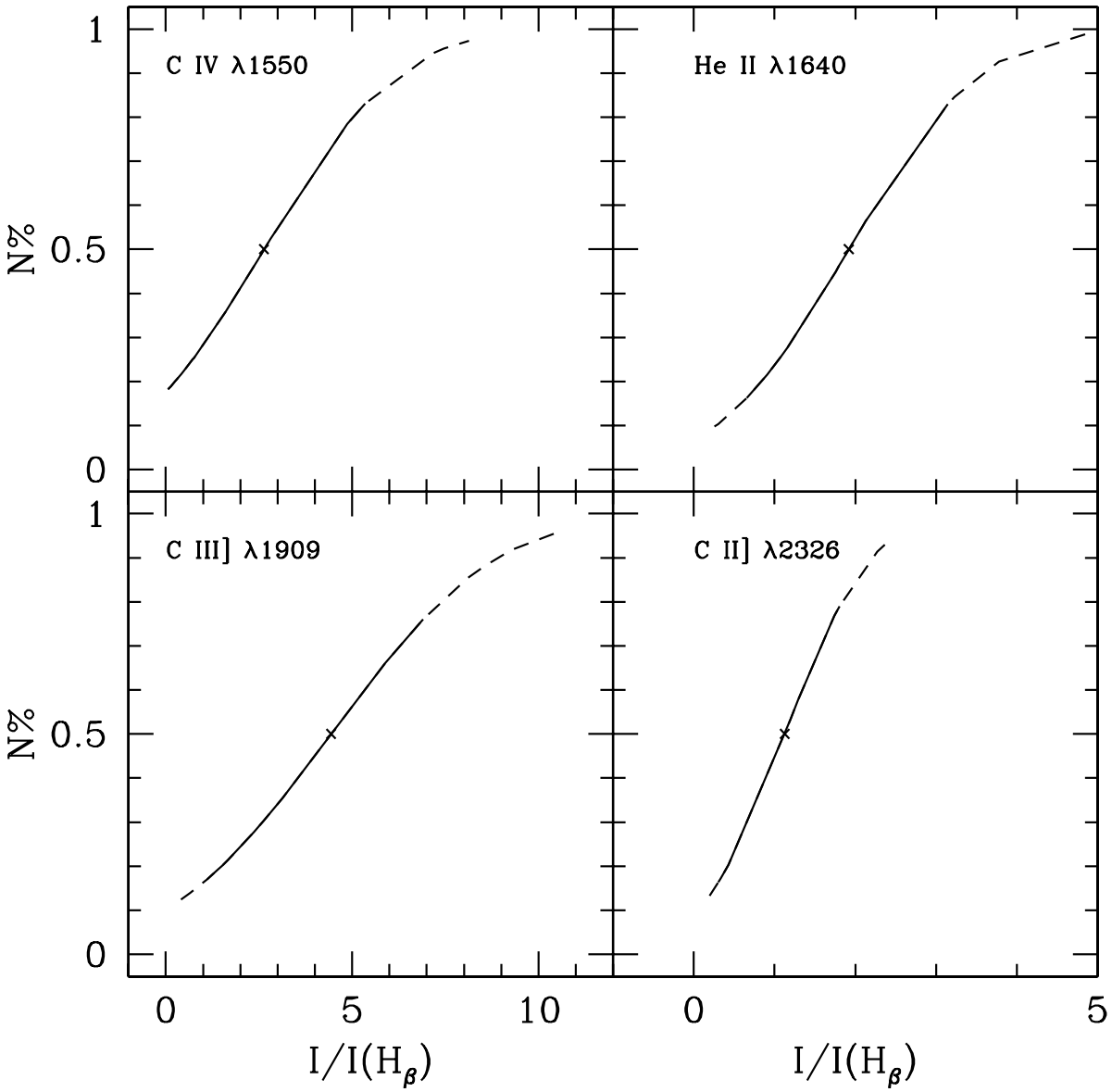
C IV λ1550
He II λ1640
C III] λ1909
C II] λ2326
N%
1
0.5
0
0
5
10
I/I(Hβ)

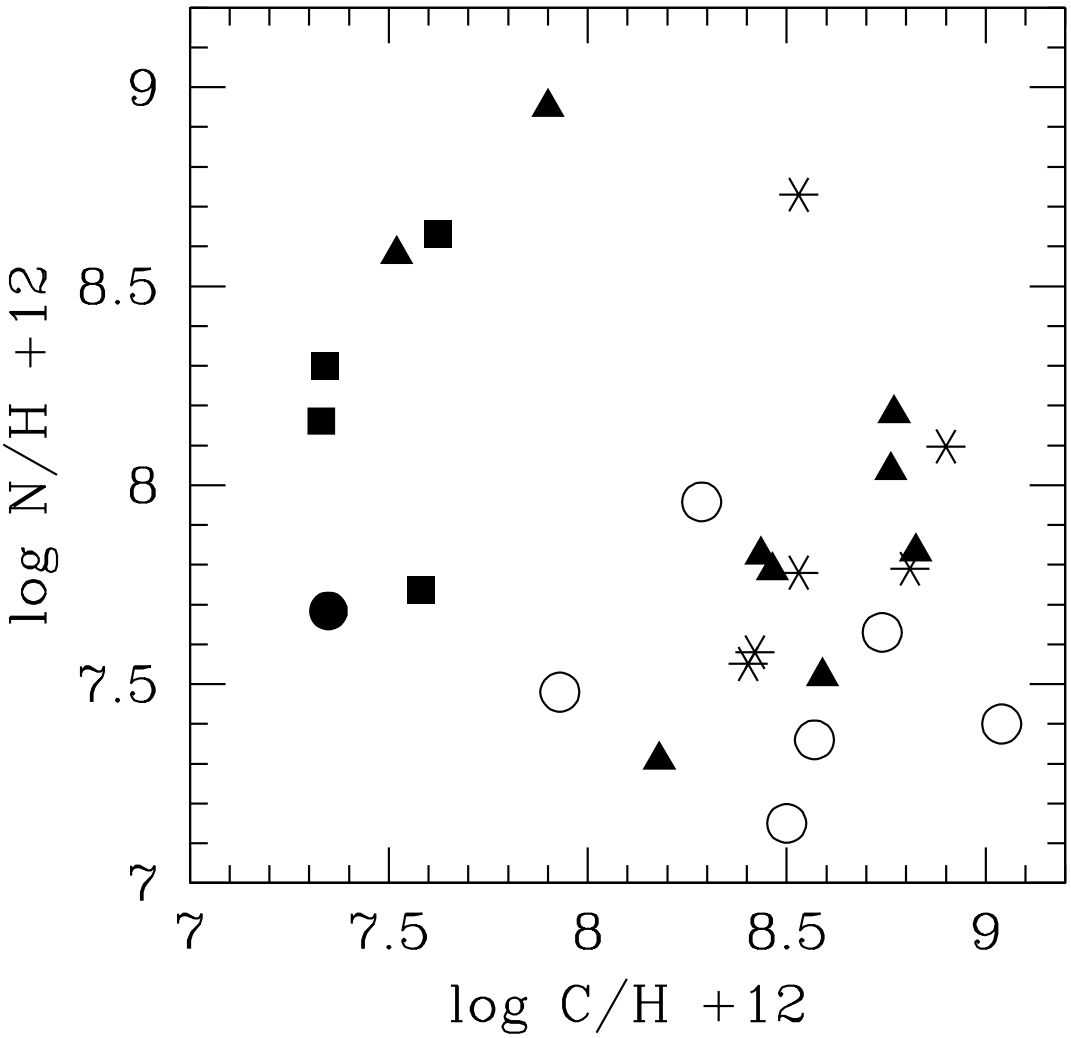
9
8.5
8
7.5
7
log N/H +12
7
7.5
8
8.5
9
log C/H +12

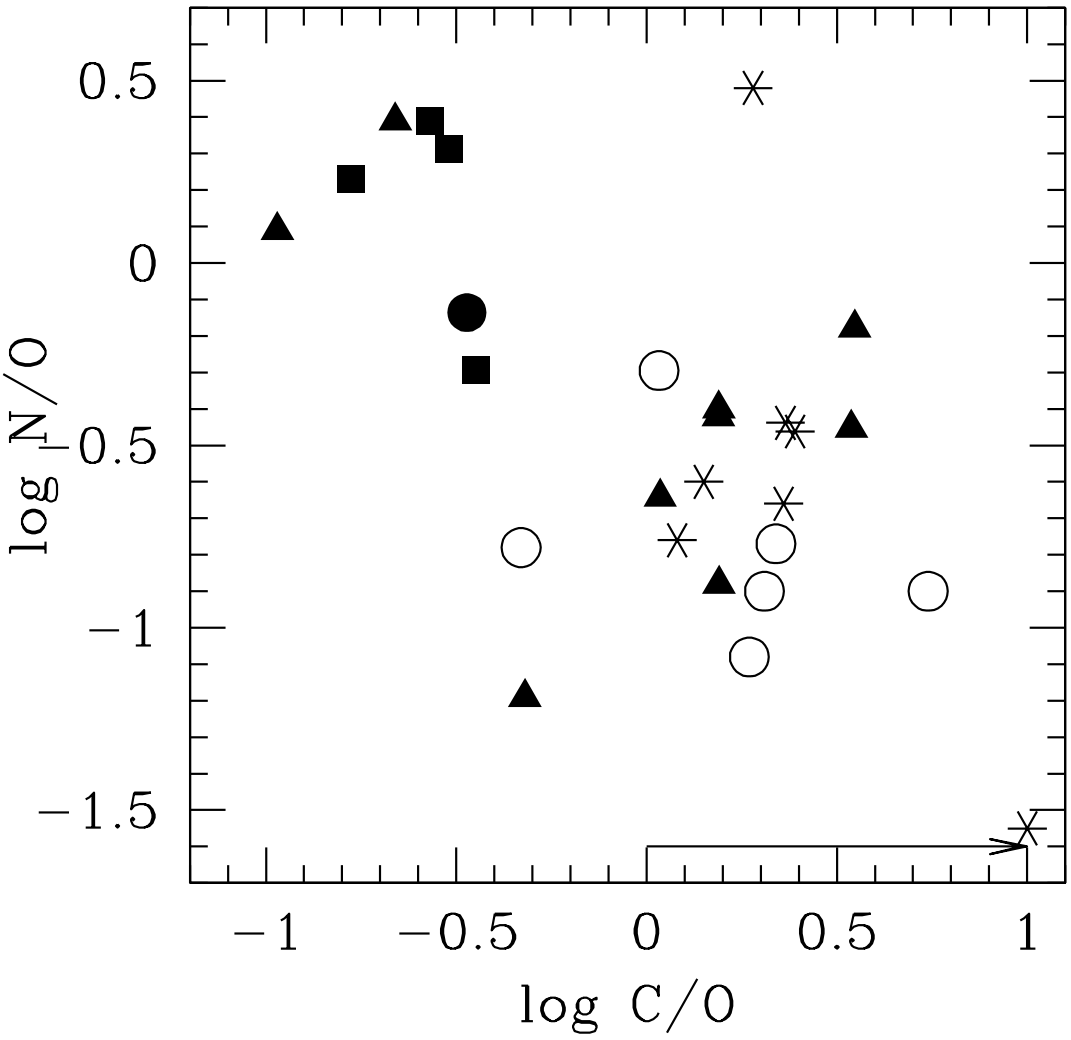
0.5
0
−0.5
−1
−1.5
log N/O
−1
−0.5
0
0.5
1
log C/O

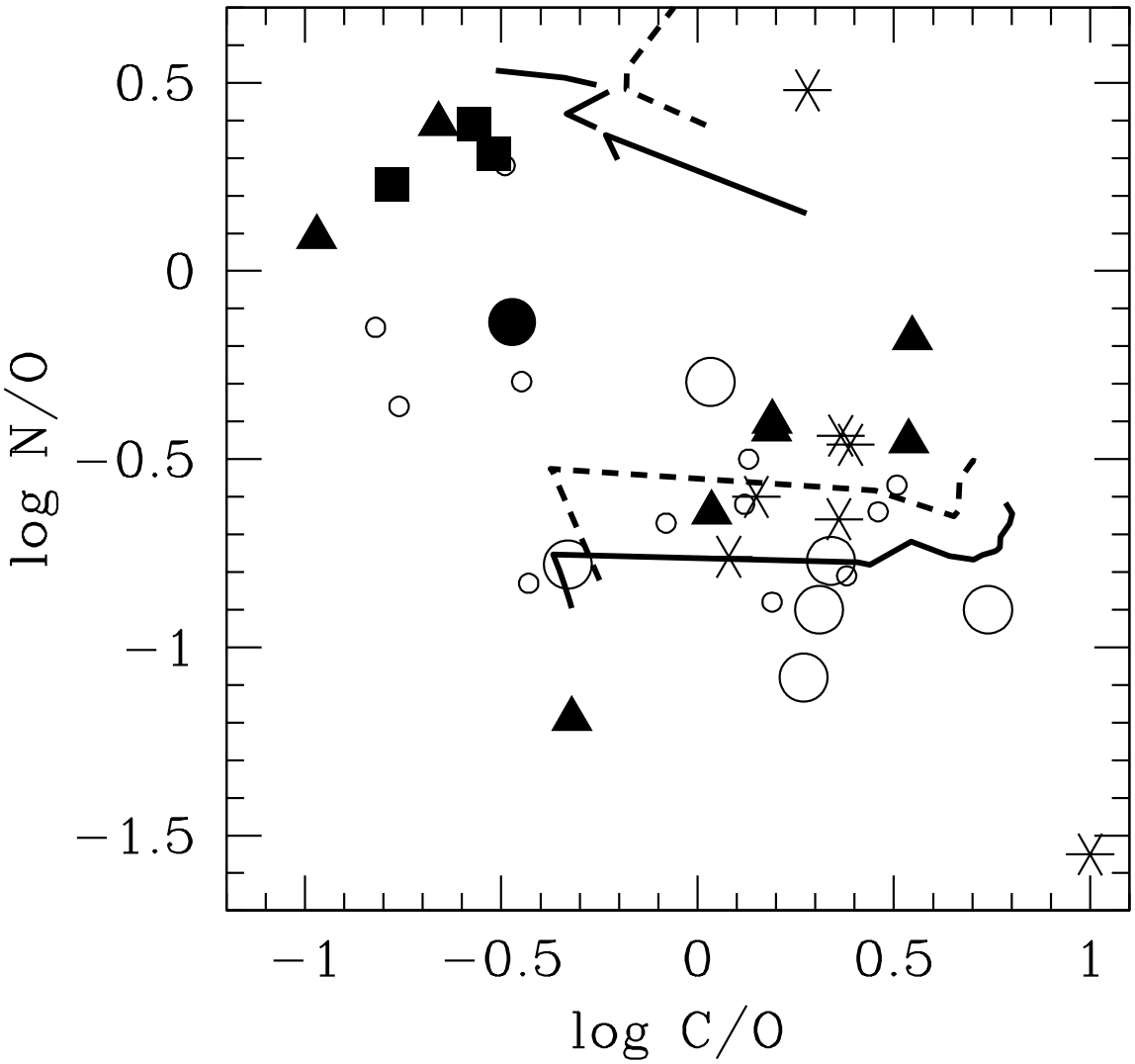
0.5
0
−0.5
−1
−1.5
log N/O
−1
−0.5
0
0.5
1
log C/O

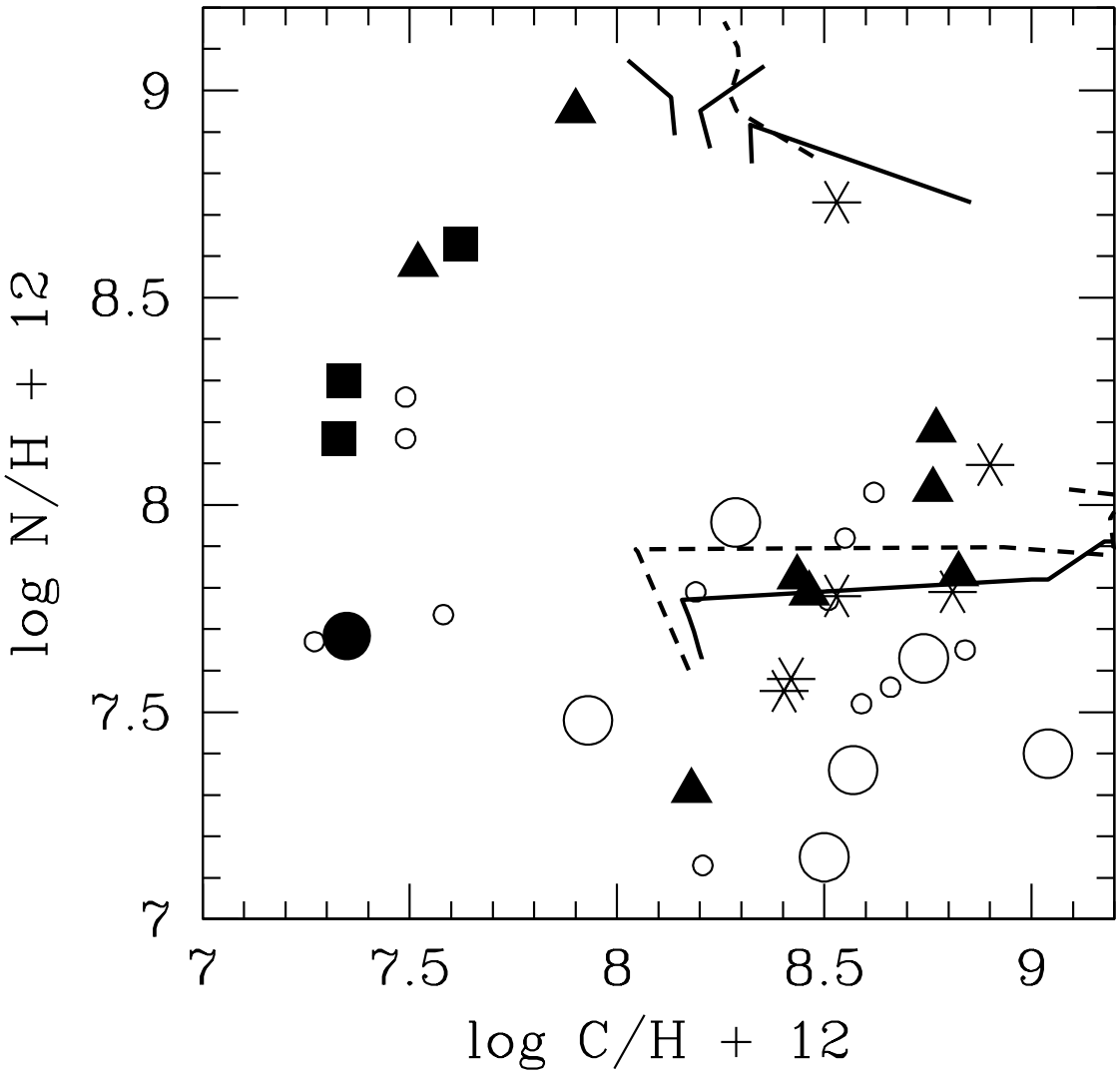
9
8.5
8
7.5
7
log N/H + 12
7
7.5
8
8.5
9
log C/H + 12

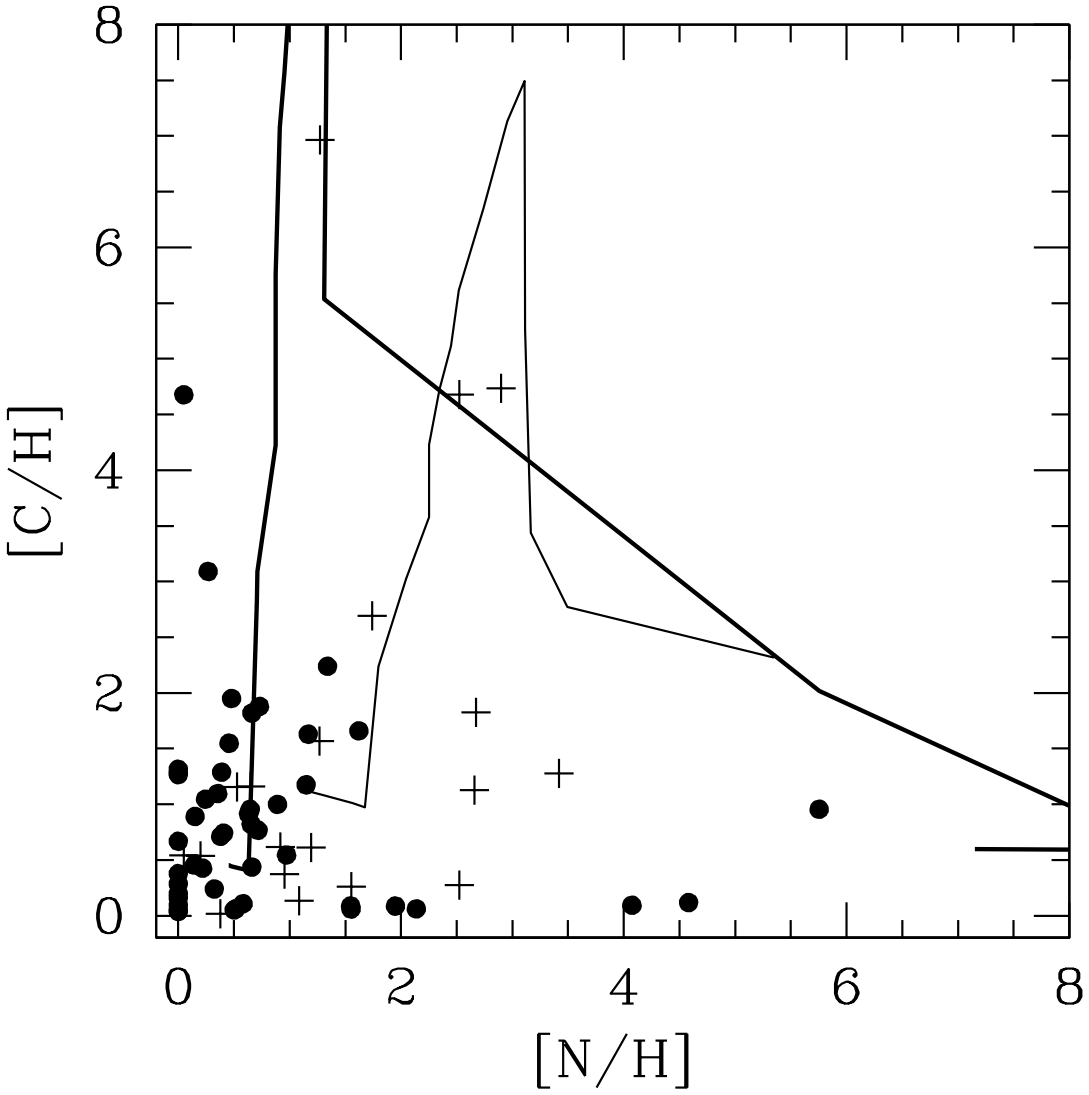
8
6
4
2
0
[C/H]
0
2
4
6
8
[N/H]

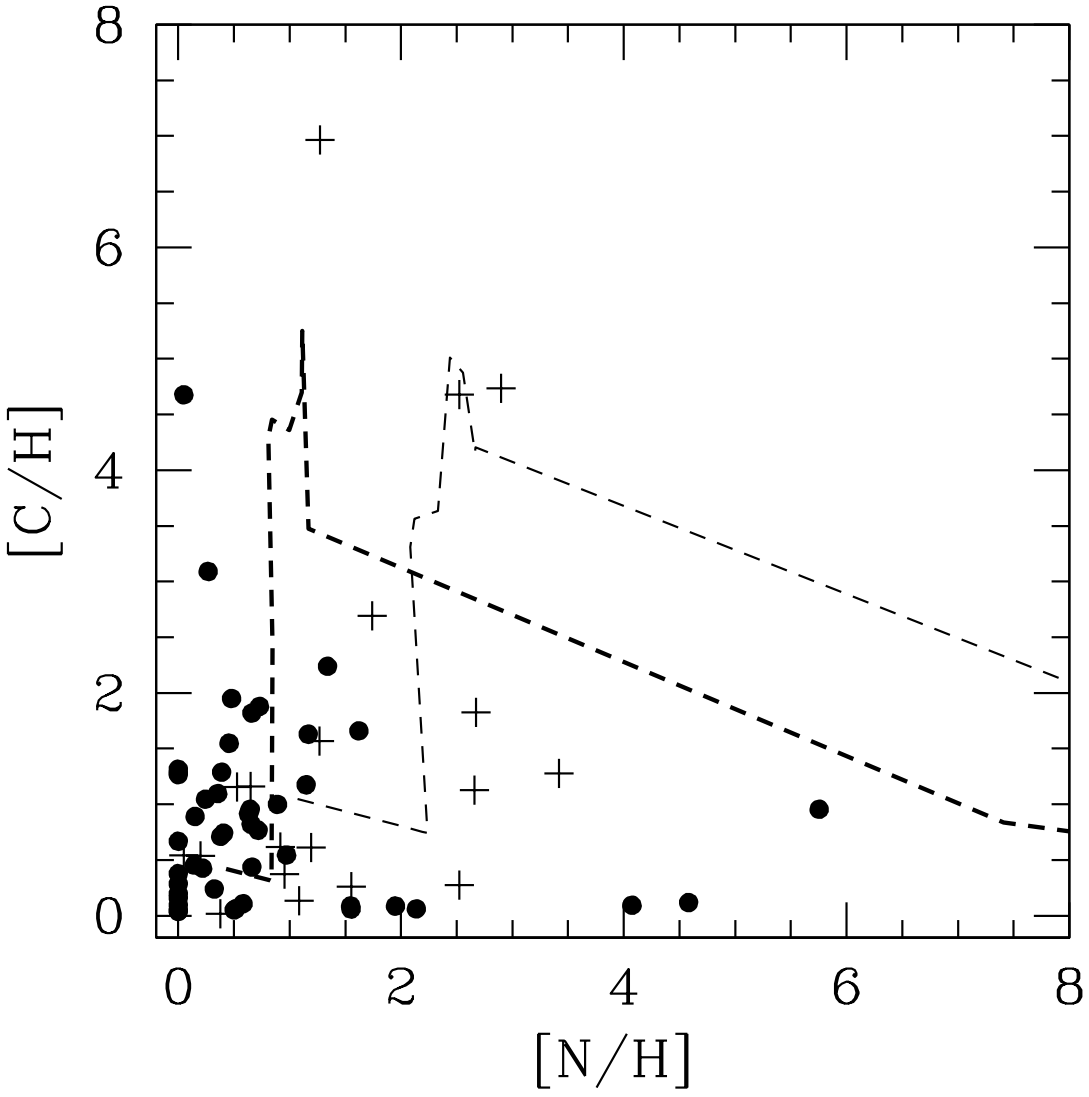
8
6
4
2
0
[C/H]
0
2
4
6
8
[N/H]

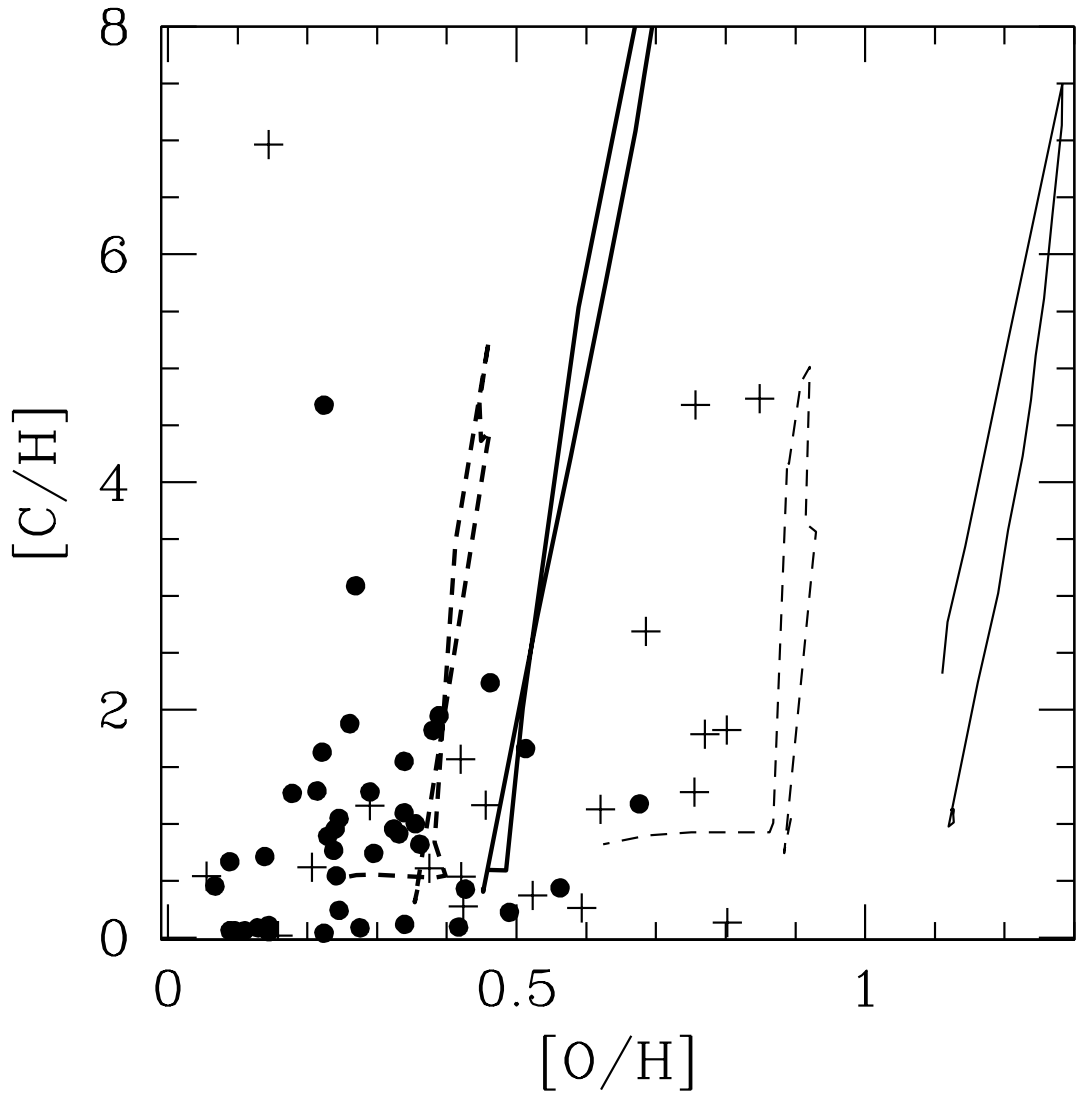
8
6
4
2
0
[C/H]
0
0.5
1
[O/H]